ELSEVIER

Comput. Methods Appl. Mech. Engrg. 185 (2000) 37–74

Computer methods in applied mechanics and engineering

www.elsevier.com/locate/cma

Adaptivity and convergence in the Voronoi cell finite element model for analyzing heterogeneous materials

Suresh Moorthy *, Somnath Ghosh

Department of Aerospace Engineering, Applied Mechanics and Aviation, The Ohio State University, 155 West Woodruff Avenue, Columbus, OH 43210, USA

Abstract

In this paper, an adaptive Voronoi cell finite element model is presented for analyzing micromechanical response of composites and porous materials. Both elastic and elastic–plastic materials are considered. Two error measures, viz. a traction reciprocity error and an error in the kinematic relation, are formulated as indicators of the quality of VCFEM solutions. Based on a posteriori evaluation of these error measures, element adaptation is executed in two consecutive stages. In the first stage, displacement function adaptations on the element boundaries and matrix–inclusion/void interfaces are carried out to minimize the corresponding traction reciprocity errors. This is accomplished through a sequence of h-refinement and spectral p-enrichment strategy in an optimal displacement direction. Following this, an enrichment of matrix and inclusion stress functions or ${}^{\mathrm{enr}}p$-adaptation is conducted to reduce the error in kinematic relations. The complete process improves convergence characteristics of the VCFEM solution. Numerical analysis is conducted to examine the potential of the resulting VCFEM code in analyzing microstructures with different distributions, sizes and shapes of heterogeneities. The method is seen to perform very well for the wide variety of problems solved. © 2000 Elsevier Science S.A. All rights reserved.

1. Introduction

The Voronoi cell finite element model (VCFEM) has been developed for elastic and elasto–plastic micromechanical problems in composite and porous materials in [1–4], and for damage initiation in reinforced composites by particle cracking in [4–6]. The model naturally evolves from the microstructure by Voronoi tessellation to generate a morphology based network of multi-sided Voronoi cells, each cell containing an embedded heterogeneity (inclusion or void). In VCFEM, each cell is treated as a FEM element and requires no additional discretization. Arbitrary dispersions, shapes and sizes of heterogeneities, as acquired from actual micrographs, are readily modeled by this method. Pre-processing efforts for generating the microstructural models are substantially reduced [7]. With assumptions incorporated from established micromechanics theories, VCFEM has been shown to require significantly reduced degrees of freedom compared to displacement based FEM models [8–10]. Computational efficiency is thus enhanced. Furthermore, VCFEM can be used to provide a direct link between quantitative metallography and mechanical response [11,12]. The Voronoi cell FEM for microscopic modeling has also been used in conjunction with multiple scale modeling in [13–15] for elastic, elastic–plastic and damage modeling.

The Voronoi cell FEM in the above developments have been validated in the above studies through comparisons with analytical models, results of other studies in literature and simulations with conventional finite element packages. While such heuristic studies have been satisfactory in general, rigorous studies on the convergence characteristics have not thus far been conducted. Such studies on the rate of convergence

* Corresponding author.

0045-7825/00/$ - see front matter © 2000 Elsevier Science S.A. All rights reserved.
PII: S 0 0 4 5 - 7 8 2 5 (9 9) 0 0 3 4 9 - 7

are necessary for information on the performance of any numerical algorithm. A number of convergence studies have been conducted for displacement based finite element methods in [16–25] where a priori and a posteriori error estimates have been proposed for measuring the quality of solutions. In the standard procedure, error analysis is generally followed by adaptive mesh strategies to improve the performance of the numerical methods and expedite the convergence rate. Such adaptive strategies have included altering the mesh structure by *h*- or mesh size adaptation, *p*- or spectral order adaptation and *hp* adaptation incorporating both. Recent studies [23–25] have also focussed on the quality of some of the error estimators and their effectiveness in improving the convergence of a numerical solution. In this context, concepts of local and pollution errors have been introduced. For the class of multi-field saddle point problems by hybrid and mixed methods, in depth studies on existence, stability and convergence have been carried out in [26–33].

Motivated by the strength of adaptive finite element analysis detailed in the literature, this paper documents an effort in incorporating a posteriori adaptivity in the Voronoi cell finite element model for analyzing micromechanical response of composites and porous materials. The problem classes considered for the adaptive analysis include both elasticity and elasto-plasticity in the materials. Error measures introduced are fundamental to the hybrid formulation used in VCFEM. They are conceived from those governing relations that are satisfied in a weak sense in this method. In particular two error measures, viz. a traction reciprocity error and an error in the kinematic relation, are formulated as indicators of the quality of VCFEM solutions. The latter error is shown to be related to a measure of strain energy error. Based on a posteriori evaluation of these error measures, element adaptation is executed in two consecutive stages. In the first stage, displacement function adaptations on the element boundaries and matrix–inclusion/void interfaces are carried out to minimize the corresponding traction reciprocity errors. The displacement field adaptation on the element boundaries and interfaces are shown to be optimal, provided they follow the direction of a traction discontinuity operator. This is accomplished through a *h*-refinement followed by a spectral *p*-enrichment strategy. The reduction of error in kinematic relations or strain energy is achieved by an enrichment of matrix and inclusion stress functions or $^{\mathrm{enr}}p$-adaptation to improve the convergence of the VCFEM solution. Numerical analysis is conducted to examine the potential of the resulting VCFEM code in analyzing microstructures with different morphologies, e.g. distribution, size and shape of heterogeneities. The method is seen to perform very well for the wide variety of problems solved. It should be emphasized, that though the focus of this paper is to establish the convergence of VCFEM for elliptical inclusions, the same ideas can be used for any polygonal inclusion such as those analyzed in [1,4–6]

2. The Voronoi cell FEM for heterogeneous materials

A typical representative material element (RME) of a heterogeneous domain Ω is shown in Fig. 1. Based on the location, size and shape of heterogeneities (inclusions and voids), the domain is discretized into N

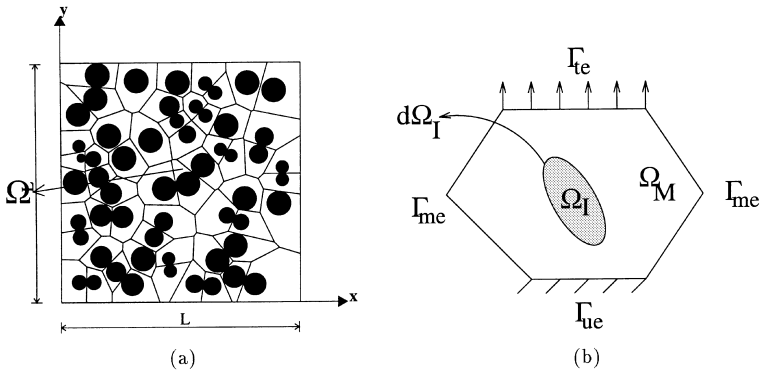

Fig. 1. (a) A heterogeneous microstructural representative volume element tessellated into a mesh of Voronoi cells. (b) A representative Voronoi cell element with various phase and boundary constituents.

Voronoi cells by a Voronoi tessellation method [7]. Each cell with included heterogeneities form an element in the VCFE model, where the element matrix phase is denoted by Ω_e^{M} and the heterogeneity phase is labeled Ω_e^{I}. The element boundary $\partial\Omega_e^{\mathrm{E}}$ is comprised of three mutually disjoint parts, viz. prescribed traction boundary Γ_{te}, prescribed displacement boundary Γ_{ue}, and interelement boundary Γ_{me}, i.e. $\partial\Omega_e^{\mathrm{E}} = \Gamma_{\mathrm{te}} \cup \Gamma_{\mathrm{ue}} \cup \Gamma_{\mathrm{me}}$. The interface $\partial\Omega_e^{\mathrm{I}}$ between the matrix and heterogeneity has an outward normal $\mathbf{n}^{\mathrm{I}}$, whereas $\mathbf{n}^{\mathrm{E}}$ is the outward normal to $\partial\Omega_e^{\mathrm{E}}$.

The Voronoi cell FEM formulation is based on the assumed stress hybrid variational principle with assumptions made from principles of micromechanics. In this formulation, the general model problem may be stated as:

$$
\begin{aligned}
&\text{Find } (\boldsymbol{\sigma}^{\mathrm{M}}, \boldsymbol{\sigma}^{\mathrm{I}}, \mathbf{u}^{\mathrm{E}}, \mathbf{u}^{\mathrm{I}}) \in \mathscr{T}^{\mathrm{M}} \times \mathscr{T}^{\mathrm{I}} \times \mathscr{V}^{\mathrm{E}} \times \mathscr{V}^{\mathrm{I}} \text{ satisfying}\\
&\nabla \cdot \boldsymbol{\sigma}^{\mathrm{M}} + \bar{\mathbf{f}}^{\mathrm{M}} = \mathbf{0} \in \Omega^{\mathrm{M}} \left(= \bigcup_{e=1,\ldots,N} \Omega_e^{\mathrm{M}} \right) \quad \text{and} \quad \nabla \cdot \boldsymbol{\sigma}^{\mathrm{I}} + \bar{\mathbf{f}}^{\mathrm{I}} = \mathbf{0} \in \Omega^{\mathrm{I}} \left(= \bigcup_{e=1,\ldots,N} \Omega_e^{\mathrm{I}} \right),\\
&\frac{\partial B^{\mathrm{M}}}{\partial \boldsymbol{\sigma}^{\mathrm{M}}} = \boldsymbol{\epsilon}^{\mathrm{M}} \in \Omega^{\mathrm{M}} \quad \text{and} \quad \frac{\partial B^{\mathrm{I}}}{\partial \boldsymbol{\sigma}^{\mathrm{I}}} = \boldsymbol{\epsilon}^{\mathrm{I}} \in \Omega^{\mathrm{I}},\\
&\mathbf{u}^{\mathrm{E}} = \bar{\mathbf{u}} \quad \text{on } \Gamma_{\mathrm{ue}}
\end{aligned}
$$

subject to the element level stationarity conditions of an energy functional

$$
\begin{aligned}
&\sum_{e=1}^{N} \Pi_e\left(\boldsymbol{\sigma}^{\mathrm{M}}, \boldsymbol{\sigma}^{\mathrm{I}}, \mathbf{u}^{\mathrm{E}}, \mathbf{u}^{\mathrm{I}}\right) \geqslant \sum_{e=1}^{N} \Pi_e\left(\boldsymbol{\tau}^{\mathrm{M}}, \boldsymbol{\sigma}^{\mathrm{I}}, \mathbf{u}^{\mathrm{E}}, \mathbf{u}^{\mathrm{I}}\right),\\
&\sum_{e=1}^{N} \Pi_e\left(\boldsymbol{\sigma}^{\mathrm{M}}, \boldsymbol{\sigma}^{\mathrm{I}}, \mathbf{u}^{\mathrm{E}}, \mathbf{u}^{\mathrm{I}}\right) \geqslant \sum_{e=1}^{N} \Pi_e\left(\boldsymbol{\sigma}^{\mathrm{M}}, \boldsymbol{\tau}^{\mathrm{I}}, \mathbf{u}^{\mathrm{E}}, \mathbf{u}^{\mathrm{I}}\right),\\
&\sum_{e=1}^{N} \Pi_e\left(\boldsymbol{\sigma}^{\mathrm{M}}, \boldsymbol{\sigma}^{\mathrm{I}}, \mathbf{u}^{\mathrm{E}}, \mathbf{u}^{\mathrm{I}}\right) \geqslant \sum_{e=1}^{N} \Pi_e\left(\boldsymbol{\sigma}^{\mathrm{M}}, \boldsymbol{\sigma}^{\mathrm{I}}, \mathbf{v}^{\mathrm{E}}, \mathbf{u}^{\mathrm{I}}\right),\\
&\sum_{e=1}^{N} \Pi_e\left(\boldsymbol{\sigma}^{\mathrm{M}}, \boldsymbol{\sigma}^{\mathrm{I}}, \mathbf{u}^{\mathrm{E}}, \mathbf{u}^{\mathrm{I}}\right) \geqslant \sum_{e=1}^{N} \Pi_e\left(\boldsymbol{\sigma}^{\mathrm{M}}, \boldsymbol{\sigma}^{\mathrm{I}}, \mathbf{u}^{\mathrm{E}}, \mathbf{v}^{\mathrm{I}}\right),\\
&\forall\left(\boldsymbol{\tau}^{\mathrm{M}}, \boldsymbol{\tau}^{\mathrm{I}}, \mathbf{v}^{\mathrm{E}}, \mathbf{v}^{\mathrm{I}}\right) \in \mathscr{T}^{\mathrm{M}} \times \mathscr{T}^{\mathrm{I}} \times \mathscr{V}^{\mathrm{E}} \times \mathscr{V}^{\mathrm{I}},
\end{aligned}
\tag{1}
$$

where $\boldsymbol{\sigma}$, $\boldsymbol{\epsilon}$, B and $\mathbf{f}$ are the equilibriated stress fields, the corresponding strain fields, the complimentary energy and body forces per unit volume respectively in the element interior, and $\mathbf{u}^{\mathrm{E}}$ and $\mathbf{u}^{\mathrm{I}}$ are the compatible displacement fields on the boundary $\partial\Omega_e^{\mathrm{E}}$ and the matrix–inclusion/void interface $\partial\Omega_e^{\mathrm{I}}$. In Eq. (1) variables with superscripts M and I correspond to the interior of the matrix and inclusion phases respectively, while superscripts E and I refer to variables on the element boundary and matrix–inclusion interface respectively. Stress and displacement solutions belong to the Hilbert spaces denoted by $\mathscr{T}^{\mathrm{M}}, \mathscr{T}^{\mathrm{I}}, \mathscr{V}^{\mathrm{E}}, \mathscr{V}^{\mathrm{I}}$ and defined as:

$$
\begin{aligned}
&\mathscr{T}^{\mathrm{M}} = \bigcup_{e=1,\ldots,N} \mathscr{T}_e^{\mathrm{M}}; \qquad \mathscr{T}_e^{\mathrm{M}} = \{\boldsymbol{\tau}_e^{\mathrm{M}} \in H^0(\Omega_e^{\mathrm{M}}) : \nabla \cdot \boldsymbol{\tau}_e^{\mathrm{M}} + \bar{\mathbf{f}}_e^{\mathrm{M}} = \mathbf{0}\} \quad \forall e,\\
&\mathscr{T}^{\mathrm{I}} = \bigcup_{e=1,\ldots,N} \mathscr{T}_e^{\mathrm{I}}; \qquad \mathscr{T}_e^{\mathrm{I}} = \{\boldsymbol{\tau}_e^{\mathrm{I}} \in H^0(\Omega_e^{\mathrm{I}}) : \nabla \cdot \boldsymbol{\tau}_e^{\mathrm{I}} + \bar{\mathbf{f}}_e^{\mathrm{I}} = \mathbf{0}\} \quad \forall e,\\
&\mathscr{V}^{\mathrm{E}} = \bigcup_{e=1,\ldots,N} \mathscr{V}_e^{\mathrm{E}}; \qquad \mathscr{V}_e^{\mathrm{E}} = \left\{ \mathbf{v}_e^{\mathrm{E}} \in \mathscr{H}^0\left(\bigcup_{i=1,\ldots,n_{\mathrm{E}}} {}_i\partial\Omega_e^{\mathrm{E}} \oplus \bigcup_{i,j=1,\ldots,n_{\mathrm{E}}, i>j} {}_{ij}S_e^{\mathrm{E}} \right) : \mathbf{v}_e^{\mathrm{E}} = \bar{\mathbf{u}} \ \text{ on } \Gamma_{\mathrm{ue}} \right\} \quad \forall e,\\
&\mathscr{V}^{\mathrm{I}} = \bigcup_{e=1,\ldots,N} \mathscr{V}_e^{\mathrm{I}}; \qquad \mathscr{V}_e^{\mathrm{I}} = \left\{ \mathbf{v}_e^{\mathrm{I}} \in \mathscr{H}^0\left(\bigcup_{i=1,\ldots,n_{\mathrm{E}}} {}_i\partial\Omega_e^{\mathrm{I}} \oplus \bigcup_{i,j=1,\ldots,n_{\mathrm{E}}, i>j} {}_{ij}S_e^{\mathrm{I}} \right) \right\} \quad \forall e,
\end{aligned}
\tag{2}
$$

where the element boundary $\partial\Omega_e^{\mathrm{E}}$ and the interface $\partial\Omega_e^{\mathrm{I}}$ are defined as the union of boundary segments ${}_i\partial\Omega_e^{\mathrm{E/I}}$, $i = 1, \ldots, n_{\mathrm{E}}$, and isolated nodal points ${}_{ij}S_e^{\mathrm{E/I}}$, $(i, j) = 1, \ldots, n_{\mathrm{E}}$, $i > j$ joining the i and jth segments, such that

$$\partial\Omega_e^{\mathrm{E/I}} = \bigcup_{i=1,\ldots,n_{\mathrm{E}}} {}_i\partial\Omega_e^{\mathrm{E/I}} \oplus \bigcup_{i,j=1,\ldots,n_{\mathrm{E}},i>j} {}_{ij}S_e^{\mathrm{E/I}}. \tag{3}$$

The saddle point problem in terms of the energy functional in Eq. (1) yields, as Euler equations, the weak forms of the kinematic equation and traction reciprocity conditions. In an incremental finite element formulation for rate independent small deformation plasticity, the incremented element energy functional Π_e in Eq. (1) is defined in terms of stresses and boundary and interface displacement fields as:

$$\begin{aligned}\Pi_e(\triangle\boldsymbol{\sigma}_e^{\mathrm{M}}, \triangle\boldsymbol{\sigma}_e^{\mathrm{I}}, \triangle\mathbf{u}_e^{\mathrm{E}}, \triangle\mathbf{u}_e^{\mathrm{I}}) = &-\int_{\Omega_e^{\mathrm{M}}} \triangle B^{\mathrm{M}}(\boldsymbol{\sigma}_e^{\mathrm{M}}, \triangle\boldsymbol{\sigma}_e^{\mathrm{M}})\,\mathrm{d}\Omega - \int_{\Omega_e^{\mathrm{I}}} \triangle B^{\mathrm{I}}(\boldsymbol{\sigma}_e^{\mathrm{I}}, \triangle\boldsymbol{\sigma}_e^{\mathrm{I}})\,\mathrm{d}\Omega - \int_{\Omega_e^{\mathrm{M}}} \boldsymbol{\epsilon}_e^{\mathrm{M}} : \triangle\boldsymbol{\sigma}_e^{\mathrm{M}}\,\mathrm{d}\Omega \\ &- \int_{\Omega_e^{\mathrm{I}}} \boldsymbol{\epsilon}_e^{\mathrm{I}} : \triangle\boldsymbol{\sigma}_e^{\mathrm{I}}\,\mathrm{d}\Omega + \int_{\partial\Omega_e^{\mathrm{E}}} (\boldsymbol{\sigma}_e^{\mathrm{M}} + \triangle\boldsymbol{\sigma}_e^{\mathrm{M}}) \cdot \mathbf{n}^{\mathrm{E}} \cdot (\mathbf{u}_e^{\mathrm{E}} + \triangle\mathbf{u}_e^{\mathrm{E}})\,\mathrm{d}\partial\Omega \\ &- \int_{\Gamma_{tE}} (\bar{\mathbf{t}} + \triangle\bar{\mathbf{t}}) \cdot (\mathbf{u}_e^{\mathrm{E}} + \triangle\mathbf{u}_e^{\mathrm{E}})\,\mathrm{d}\Gamma \\ &- \int_{\partial\Omega_e^{\mathrm{I}}} (\boldsymbol{\sigma}_e^{\mathrm{M}} + \triangle\boldsymbol{\sigma}_e^{\mathrm{M}} - \boldsymbol{\sigma}_e^{\mathrm{I}} - \triangle\boldsymbol{\sigma}_e^{\mathrm{I}}) \cdot \mathbf{n}^{\mathrm{I}} \cdot (\mathbf{u}_e^{\mathrm{I}} + \triangle\mathbf{u}_e^{\mathrm{I}})\,\mathrm{d}\partial\Omega.\end{aligned} \tag{4}$$

The increment of element complimentary energy $\triangle B$ yields the incremental constitutive relation $\partial\triangle B/\partial\triangle\boldsymbol{\sigma} = \triangle\boldsymbol{\epsilon}$, in terms of the increments of equilibriated stresses $\boldsymbol{\sigma}$ and associated strains $\boldsymbol{\epsilon}$. Traction increments on the boundary Γ_{te} is denoted by $\triangle\bar{\mathbf{t}}$. The element energy functional consists of bilinear forms ${}_e\mathsf{a}^{\mathrm{M/I}}$, ${}_e\mathsf{b}_{\mathrm{E/I}}^{\mathrm{M/I}}$ and the linear functionals ${}_e\mathsf{f}^{\mathrm{E}}$ and ${}_e\mathsf{g}^{\mathrm{M/I}}$ defined as

$$\begin{aligned}
&{}_e\mathsf{a}^{\mathrm{M/I}}(\triangle\boldsymbol{\sigma}_e^{\mathrm{M/I}}, \triangle\boldsymbol{\tau}_e^{\mathrm{M/I}}) = \int_{\Omega_e^{\mathrm{M/I}}} \triangle\boldsymbol{\epsilon}_e^{\mathrm{M/I}}(\triangle\boldsymbol{\sigma}_e^{\mathrm{M/I}}) : \triangle\boldsymbol{\tau}_e^{\mathrm{M/I}}\,\mathrm{d}\Omega; \qquad {}_e\mathsf{a}^{\mathrm{M/I}} : \mathscr{T}_e^{\mathrm{M/I}} \times \mathscr{T}_e^{\mathrm{M/I}} \to \mathscr{R}, \\
&{}_e\mathsf{b}_{\mathrm{E/I}}^{\mathrm{M/I}}(\triangle\boldsymbol{\sigma}_e^{\mathrm{M/I}}, \triangle\mathbf{u}_e^{\mathrm{E/I}}) = \int_{\partial\Omega_e^{\mathrm{E/I}}} \triangle\boldsymbol{\sigma}_e^{\mathrm{M/I}} \cdot \mathbf{n}_e^{\mathrm{E/I}} \cdot \triangle\mathbf{u}_e^{\mathrm{E/I}}\,\mathrm{d}\Omega; \qquad {}_e\mathsf{b}_{\mathrm{E/I}}^{\mathrm{M/I}} : \mathscr{T}_e^{\mathrm{M/I}} \times \mathscr{V}_e^{\mathrm{E/I}} \to \mathscr{R}, \\
&{}_e\mathsf{f}^{\mathrm{E}}(\triangle\mathbf{u}_e^{\mathrm{E}}) = \int_{\Gamma_{\mathrm{te}}} (\bar{\mathbf{t}} + \triangle\bar{\mathbf{t}}) \cdot \triangle\mathbf{u}_e^{\mathrm{E}}\,\mathrm{d}\Gamma; \qquad {}_e\mathsf{f}^{\mathrm{E}} : \mathscr{V}_e^{\mathrm{E}} \to \mathscr{R}, \\
&{}_e\mathsf{g}^{\mathrm{M/I}}(\triangle\boldsymbol{\sigma}_e^{\mathrm{M/I}}) = \int_{\Omega_e^{\mathrm{M/I}}} \boldsymbol{\epsilon}_e^{\mathrm{M/I}} : \triangle\boldsymbol{\sigma}_e^{\mathrm{M/I}}\,\mathrm{d}\Gamma; \qquad {}_e\mathsf{g}^{\mathrm{M/I}} : \mathscr{T}_e^{\mathrm{M/I}} \to \mathscr{R}.
\end{aligned} \tag{5}$$

Throughout this paper a slash (/) is used to denote alternative situations, e.g. M/I corresponds to the interior of the matrix or inclusion. In the Voronoi cell formulation, the equilibrium and constitutive relations in the matrix and inclusion phases, and compatibility on the element boundary and matrix–inclusion/void interface are satisfied a priori. The element kinematic equations in the matrix and inclusion phases, i.e.

$$\nabla\triangle\mathbf{u}_e^{\mathrm{M}} = \triangle\epsilon_e^{\mathrm{M}} \quad \text{in } \Omega_e^{\mathrm{M}} \quad \text{and} \quad \nabla\triangle\mathbf{u}_e^{\mathrm{I}} = \triangle\epsilon_e^{\mathrm{I}} \quad \text{in } \Omega_e^{\mathrm{I}} \tag{6}$$

are satisfied in a weak sense from the stationarity conditions of the element energy functional in Eq. (4). The weak forms are obtained by setting the first variation of Π_e with respect to the stresses in the matrix and inclusion phases to zero as

$$\begin{aligned}
-{}_e\mathsf{a}^{\mathrm{M}}(\triangle\boldsymbol{\sigma}_e^{\mathrm{M}}, \delta\boldsymbol{\sigma}_e^{\mathrm{M}}) + {}_e\mathsf{b}_{\mathrm{E}}^{\mathrm{M}}(\delta\boldsymbol{\sigma}_e^{\mathrm{M}}, \triangle\mathbf{u}_e^{\mathrm{E}}) - {}_e\mathsf{b}_{\mathrm{I}}^{\mathrm{M}}(\delta\boldsymbol{\sigma}_e^{\mathrm{M}}, \triangle\mathbf{u}_e^{\mathrm{I}}) = 0 \quad \forall\delta\boldsymbol{\sigma}_e^{\mathrm{M}} \in \mathscr{T}_e^{\mathrm{M}}, \quad \forall e, \\
-{}_e\mathsf{a}^{\mathrm{I}}(\triangle\boldsymbol{\sigma}_e^{\mathrm{I}}, \delta\boldsymbol{\sigma}_e^{\mathrm{I}}) + {}_e\mathsf{b}_{\mathrm{I}}^{\mathrm{I}}(\delta\boldsymbol{\sigma}_e^{\mathrm{I}}, \triangle\mathbf{u}_e^{\mathrm{I}}) = 0 \quad \forall\delta\boldsymbol{\sigma}_e^{\mathrm{I}} \in \mathscr{T}_e^{\mathrm{I}}, \quad \forall e.
\end{aligned} \tag{7}$$

Eq. (7) is solved for stress increments in the constituent phases. Additionally the traction reciprocity conditions on the inter-element boundary Γ_{me}, traction boundary Γ_{te} and matrix–inclusion/void interface $\partial\Omega_e^{\mathrm{I}}$, viz.

$$\begin{aligned}
&(\boldsymbol{\sigma}_e^{\mathrm{M}} + \triangle\boldsymbol{\sigma}_e^{\mathrm{M}}) \cdot \mathbf{n}^{\mathrm{E}+} = -(\boldsymbol{\sigma}_e^{\mathrm{M}} + \triangle\boldsymbol{\sigma}_e^{\mathrm{M}}) \cdot \mathbf{n}^{\mathrm{E}-} \quad \text{on } \Gamma_{\mathrm{me}} \text{ (inter-element boundary)}, \\
&(\boldsymbol{\sigma}_e^{\mathrm{M}} + \triangle\boldsymbol{\sigma}_e^{\mathrm{M}}) \cdot \mathbf{n}^{\mathrm{E}} = \bar{\mathbf{t}} + \triangle\bar{\mathbf{t}} \text{on } \Gamma_{\mathrm{te}} \text{ (traction boundary)}, \\
&(\boldsymbol{\sigma}_e^{\mathrm{I}} + \triangle\boldsymbol{\sigma}_e^{\mathrm{I}}) \cdot \mathbf{n}^{\mathrm{I}} = (\boldsymbol{\sigma}_e^{\mathrm{M}} + \triangle\boldsymbol{\sigma}_e^{\mathrm{M}}) \cdot \mathbf{n}^{\mathrm{I}} \quad \text{on } \partial\Omega_e^{\mathrm{I}} \text{ (interface)},
\end{aligned} \tag{8}$$

are satisfied in a weak sense from the total energy functional of the heterogeneous RME which is obtained by adding each element contribution as

$$\Pi = \sum_{e=1}^{N} \Pi_e. \tag{9}$$

The corresponding weak form is obtained by setting its first variation with respect to the displacements on the element boundaries and matrix–inclusion interfaces to zero as:

$$\begin{aligned} &\sum_{e=1}^{N} {}_e\mathsf{b}_{\mathrm{E}}^{\mathrm{M}}\big((\boldsymbol{\sigma}_e^{\mathrm{M}} + \triangle\boldsymbol{\sigma}_e^{\mathrm{M}}), \delta\mathbf{u}_e^{\mathrm{E}}\big) = \sum_{e=1}^{N} {}_e\mathsf{f}^{\mathrm{E}}\big(\delta\mathbf{u}_e^{\mathrm{E}}\big) \quad \forall\delta\mathbf{u}_e^{\mathrm{E}} \in \bar{\mathscr{V}}_e^{\mathrm{E}}, \\ &\quad \text{where } \bar{\mathscr{V}}_e^{\mathrm{E}} = \big\{\mathbf{v}_e^{\mathrm{E}} \in \mathscr{H}^0\big(\partial\Omega_e^{\mathrm{E}}\big) : \mathbf{v}^{\mathrm{E}} = \mathbf{0} \quad \text{on } \Gamma_{\mathrm{ue}}\big\} \quad \forall e, \\ &\quad {}_e\mathsf{b}_{\mathrm{I}}^{\mathrm{I}}((\boldsymbol{\sigma}_e^{\mathrm{I}} + \triangle\boldsymbol{\sigma}_e^{\mathrm{I}}), \delta\mathbf{u}_e^{\mathrm{I}}) - {}_e\mathsf{b}_{\mathrm{I}}^{\mathrm{M}}\big((\boldsymbol{\sigma}_e^{\mathrm{M}} + \triangle\boldsymbol{\sigma}_e^{\mathrm{M}}), \delta\mathbf{u}_e^{\mathrm{I}}\big) = 0 \quad \forall\delta\mathbf{u}_e^{\mathrm{I}} \in \mathscr{V}_e^{\mathrm{I}}, \ \forall e. \end{aligned} \tag{10}$$

The solution of Eq. (10) yields displacement increments at nodes located on the element boundary and the interface.

2.1. Element formulations and assumptions

As discussed in [1,2], equilibriated two-dimensional stress fields are attained through the use of independent Airy's stress functions $\Phi^{\mathrm{M/I}}(x,y)$ in the matrix and inclusion phases respectively, such that

$$\begin{Bmatrix} \triangle\sigma_{xx}^{\mathrm{M}} \\ \triangle\sigma_{yy}^{\mathrm{M}} \\ \triangle\sigma_{xy}^{\mathrm{M}} \end{Bmatrix} = \begin{Bmatrix} \dfrac{\partial^2\Phi^{\mathrm{M}}}{\partial y^2} \\ \dfrac{\partial^2\Phi^{\mathrm{M}}}{\partial x^2} \\ -\dfrac{\partial^2\Phi^{\mathrm{M}}}{\partial x\partial y} \end{Bmatrix} \quad \text{and} \quad \begin{Bmatrix} \triangle\sigma_{xx}^{\mathrm{I}} \\ \triangle\sigma_{yy}^{\mathrm{I}} \\ \triangle\sigma_{xy}^{\mathrm{I}} \end{Bmatrix} = \begin{Bmatrix} \dfrac{\partial^2\Phi^{\mathrm{I}}}{\partial y^2} \\ \dfrac{\partial^2\Phi^{\mathrm{I}}}{\partial x^2} \\ -\dfrac{\partial^2\Phi^{\mathrm{I}}}{\partial x\partial y} \end{Bmatrix}. \tag{11}$$

Different functional forms of Φ^{M} and Φ^{I} with independent coefficients allow for stress jumps across the interface. The element stress increments may be written in terms of well defined functions of position $[\mathbf{P}(x,y)]$ and unknown stress coefficients $\boldsymbol{\beta}$ to be solved, i.e.

$$\{\triangle\boldsymbol{\sigma}_e^{\mathrm{M}}\} = [\mathbf{P}^{\mathrm{M}}(x,y)]\{\triangle\boldsymbol{\beta}_e^{\mathrm{M}}\}, \quad \{\triangle\boldsymbol{\sigma}_e^{\mathrm{I}}\} = [\mathbf{P}^{\mathrm{I}}(x,y)]\{\triangle\boldsymbol{\beta}_e^{\mathrm{I}}\}. \tag{12}$$

Convergence of the multiple phase Voronoi cell element is strongly affected by the proper choice of stress functions and element efficiency can significantly benefit if micromechanics observations are taken into consideration in this choice. The following conditions are accounted for in the choice of matrix stress functions in VCFEM:

1. Stress functions should account for the shape of the inclusion or void, such that the shape effect should be dominant near the interface but vanish at large distances from it.
2. The shape effects should facilitate traction reciprocity at the interface or reduce to zero interface tractions for voids.

It is clearly demonstrated in [1] that pure polynomial forms stress functions do not easily accommodate the shape of a heterogeneity. Consequently, very high order terms are required for stability. Motivated by analytical solutions of Muskhelishvili and Savin [34,35], special functions are developed to augment polynomial functions and yet satisfy the conditions mentioned above. In this construction, the matrix–inclusion/void interface $\partial\Omega_e^{\mathrm{I}}$ is expressed parametrically by an equation $f(x,y) = 1$, where the analytic function $f(x,y)$ is obtained from Schwarz–Christoffel conformal mapping of an ellipse to a unit circle. The function $f(x,y)$ corresponds to a special radial coordinate with the property that $1/f = 1$ on $\partial\Omega_e^{\mathrm{I}}$ and $f \to 0$ as $(x,y) \to \infty$. Reciprocal stress functions are constructed with f in the matrix phase to augment matrix polynomial functions as

$$\Phi^{\mathrm{M}} = \Phi_{\mathrm{poly}}^{\mathrm{M}} + \Phi_{\mathrm{rec}}^{\mathrm{M}}, \tag{13}$$

where

$$\Phi^{\mathrm{M}}_{\mathrm{poly}} = \sum_{p,q} \triangle\beta^{\mathrm{M}}_{pq} x^p y^q \quad \text{and} \quad \Phi^{\mathrm{M}}_{\mathrm{rec}} = \sum_{p,q} x^p y^q \left(\frac{\triangle\beta_{pq1}}{f^{p+q}} + \frac{\triangle\beta_{pq2}}{f^{p+q+1}} + \cdots \right). \tag{14}$$

This facilitates traction field reciprocity on $\partial\Omega^{\mathrm{I}}_e$. The first term in $\Phi^{\mathrm{M}}_{\mathrm{rec}}$, i.e. f^0 (when $p+q=0$) is substituted with a $\log f$ term in order to provide the required asymptotic behavior of stresses. The stress function in the inclusion phase is assumed to consist of polynomial functions alone, i.e.

$$\Phi^{\mathrm{I}} = \Phi^{\mathrm{I}}_{\mathrm{poly}} = \triangle\beta^{\mathrm{I}}_{pq} x^p y^q. \tag{15}$$

The corresponding stresses in the matrix and inclusion phases are expressed as:

$$\begin{Bmatrix} \triangle\sigma^{\mathrm{M}}_{xx} \\ \triangle\sigma^{\mathrm{M}}_{yy} \\ \triangle\sigma^{\mathrm{M}}_{xy} \end{Bmatrix}_e = \begin{Bmatrix} \sum_{p,q} \dfrac{\partial^2(x^p y^q)}{\partial y^2} \triangle\beta_{pq} + \sum\limits_{p,q} \sum\limits_{i=p+q}^{\infty} \dfrac{\partial^2(x^p y^q/f^i)}{\partial y^2} \triangle\beta_{pqi} \\ \sum_{p,q} \dfrac{\partial^2(x^p y^q)}{\partial x^2} \triangle\beta_{pq} + \sum\limits_{p,q} \sum\limits_{i=p+q}^{\infty} \dfrac{\partial^2(x^p y^q/f^i)}{\partial x^2} \triangle\beta_{pqi} \\ -\sum_{p,q} \dfrac{\partial^2(x^p y^q)}{\partial x \partial y} \triangle\beta_{pq} - \sum\limits_{p,q} \sum\limits_{i=p+q}^{\infty} \dfrac{\partial^2(x^p y^q/f^i)}{\partial x \partial y} \triangle\beta_{pqi} \end{Bmatrix}_e$$
$$= [\mathbf{P}^{\mathrm{M}}_{\mathrm{poly}}]\{\triangle\boldsymbol{\beta}^{\mathrm{M}}_{\mathrm{poly}}\} + [\mathbf{P}^{\mathrm{M}}_{\mathrm{rec}}]\{\triangle\boldsymbol{\beta}^{\mathrm{M}}_{\mathrm{rec}}\} = [\mathbf{P}^{\mathrm{M}}]\{\triangle\boldsymbol{\beta}^{\mathrm{M}}_e\} \tag{16}$$

and

$$\begin{Bmatrix} \triangle\sigma^{\mathrm{I}}_{xx} \\ \triangle\sigma^{\mathrm{I}}_{yy} \\ \triangle\sigma^{\mathrm{I}}_{xy} \end{Bmatrix}_e = \begin{Bmatrix} \sum_{p,q} \dfrac{\partial^2(x^p y^q)}{\partial y^2} \triangle\beta_{pq} \\ \sum_{p,q} \dfrac{\partial^2(x^p y^q)}{\partial x^2} \triangle\beta_{pq} \\ -\sum_{p,q} \dfrac{\partial^2(x^p y^q)}{\partial x \partial y} \triangle\beta_{pq} \end{Bmatrix}_e = [\mathbf{P}^{\mathrm{I}}_{\mathrm{poly}}]\{\triangle\boldsymbol{\beta}^{\mathrm{I}}_{\mathrm{poly}}\} = [\mathbf{P}^{\mathrm{I}}]\{\triangle\boldsymbol{\beta}^{\mathrm{I}}_e\}. \tag{17}$$

The gradient of f in second set of terms in Eq. (16) accounts for the shape of the interface. Since the reciprocal terms decay with distance from the interface, the far-field tractions are produced predominantly by the polynomial terms in the stress function and are unaffected by the shape of the heterogeneity.

Compatible displacement increments are generated by interpolation of nodal displacements on the element boundary $\partial\Omega^{\mathrm{E}}_e$ as well as on the interface $\partial\Omega^{\mathrm{I}}_e$, [1,2] as

$$\{\triangle\mathbf{u}^{\mathrm{E}}_e\} = [\mathbf{L}^{\mathrm{E}}]\{\triangle\mathbf{q}^{\mathrm{E}}_e\} \quad \text{on } \partial\Omega^{\mathrm{E}}_e \quad \text{and} \quad \{\triangle\mathbf{u}^{\mathrm{I}}_e\} = [\mathbf{L}^{\mathrm{I}}]\{\triangle\mathbf{q}^{\mathrm{E}}_e\} \quad \text{on } \partial\Omega^{\mathrm{I}}_e. \tag{18}$$

The interpolation functions of stress and displacement fields provide a basis for the finite dimensional approximation subspaces $(\mathscr{T}^{\mathrm{M/I}}_{eH}, \mathscr{V}^{\mathrm{E/I}}_{eH})$ of the solution spaces $(\mathscr{T}^{\mathrm{M/I}}_{e}, \mathscr{V}^{\mathrm{E/I}}_{e})$, expressed as

$$\mathscr{T}^{\mathrm{M/I}}_{eH} = \mathrm{span}\{\mathbf{P}^{\mathrm{M/I}}_e\} \quad \forall e, \qquad \mathscr{V}^{\mathrm{E/I}}_{eH} = \mathrm{span}\{\mathbf{L}^{\mathrm{E/I}}_e\} \quad \forall e. \tag{19}$$

The corresponding bilinear and linear forms, defined on the discrete finite dimensional subspaces, are denoted with subscripts eH in the arguments as ${}_e\mathrm{a}^{\mathrm{M/I}}(\boldsymbol{\sigma}^{\mathrm{M/I}}_{eH}, \boldsymbol{\tau}^{\mathrm{M/I}}_{eH})$, ${}_e\mathrm{b}^{\mathrm{M/I}}_{\mathrm{E/I}}(\boldsymbol{\sigma}^{\mathrm{M/I}}_{eH}, \mathbf{u}^{\mathrm{E/I}}_{eH})$, ${}_e\mathrm{g}^{\mathrm{M/I}}(\boldsymbol{\sigma}^{\mathrm{M/I}}_{eH})$ and ${}_e f^{\mathrm{E}}(\mathbf{u}^{\mathrm{E}}_{eH})$.

Substituting Eqs. (16)–(18) in the energy functional Eq. (4) and setting the first variations with respect to the stress parameters $\triangle\boldsymbol{\beta}^{\mathrm{M}}_e$ and $\triangle\boldsymbol{\beta}^{\mathrm{I}}_e$ respectively to zero, yields the weak forms of the kinematic relations Eq. (6),

$$\begin{aligned} \int_{\Omega^{\mathrm{M}}_e} [\mathbf{P}^{\mathrm{M}}]^{\mathrm{T}}\{\triangle\boldsymbol{\epsilon}^{\mathrm{E}}_{eH}\}\,\mathrm{d}\Omega &= \int_{\partial\Omega^{\mathrm{E}}_e} [\mathbf{P}^{\mathrm{M}}]^{\mathrm{T}}[\mathbf{n}^{\mathrm{E}}][\mathbf{L}^{\mathrm{E}}]\,\mathrm{d}\Omega\{\triangle\mathbf{q}^{\mathrm{E}}_{eH}\} - \int_{\partial\Omega^{\mathrm{I}}_e} [\mathbf{P}^{\mathrm{M}}]^{\mathrm{T}}[\mathbf{n}^{\mathrm{I}}][\mathbf{L}^{\mathrm{I}}]\,\mathrm{d}\Omega\{\triangle\mathbf{q}^{\mathrm{I}}_{eH}\}, \\ \int_{\Omega^{\mathrm{I}}_e} [\mathbf{P}^{\mathrm{I}}]^{\mathrm{T}}\{\triangle\boldsymbol{\epsilon}^{\mathrm{I}}_{eH}\}\,\mathrm{d}\Omega &= \int_{\partial\Omega^{\mathrm{I}}_e} [\mathbf{P}^{\mathrm{I}}]^{\mathrm{T}}[\mathbf{n}^{\mathrm{I}}][\mathbf{L}^{\mathrm{I}}]\,\mathrm{d}\Omega\{\triangle\mathbf{q}^{\mathrm{I}}_{eH}\}, \end{aligned} \tag{20}$$

where $[\mathbf{n}^{\mathrm{E}}]$ and $[\mathbf{n}^{\mathrm{I}}]$ are the matrices with components of the normals. Furthermore, setting the first variation of the total energy functional Eq. (9) with respect to $\triangle\mathbf{q}^{\mathrm{E}}_e$ and $\triangle\mathbf{q}^{\mathrm{I}}_e$ to zero results in the weak form of the traction reciprocity conditions as

$$\sum_{e=1}^{N}\begin{bmatrix}\int_{\partial\Omega_e^{\mathrm{E}}}[\mathbf{L}^{\mathrm{E}}]^{\mathrm{T}}[\mathbf{n}^{\mathrm{E}}]^{\mathrm{T}}[\mathbf{P}^{\mathrm{M}}]\ \mathrm{d}\Omega & \mathbf{0}\\ -\int_{\partial\Omega_e^{\mathrm{I}}}[\mathbf{L}^{\mathrm{I}}]^{\mathrm{T}}[\mathbf{n}^{\mathrm{I}}]^{\mathrm{T}}[\mathbf{P}^{\mathrm{M}}]\ \mathrm{d}\Omega & \int_{\partial\Omega_e^{\mathrm{I}}}[\mathbf{L}^{\mathrm{I}}]^{\mathrm{T}}[\mathbf{n}^{\mathrm{I}}]^{\mathrm{T}}[\mathbf{P}^{\mathrm{I}}]\ \mathrm{d}\Omega\end{bmatrix}\begin{Bmatrix}\boldsymbol{\beta}_{eH}^{\mathrm{M}}+\triangle\boldsymbol{\beta}_{eH}^{\mathrm{M}}\\ \boldsymbol{\beta}_{eH}^{\mathrm{I}}+\triangle\boldsymbol{\beta}_{eH}^{\mathrm{I}}\end{Bmatrix}$$
$$=\sum_{e=1}^{N}\begin{Bmatrix}\int_{\Gamma_{\mathrm{te}}}[\mathbf{L}^{\mathrm{E}}]^{\mathrm{T}}\{\bar{\mathbf{t}}+\triangle\bar{\mathbf{t}}\}\ \mathrm{d}\Omega\\ \{\mathbf{0}\}\end{Bmatrix}. \tag{21}$$

The subscript H in the stress and displacement coefficients correspond to the finite element approximation subspaces of the solution spaces. The resulting non-linear finite element equations (20) and (21) for rate independent small deformation elasto-plasticity are solved for element stress coefficients ($\triangle\boldsymbol{\beta}_{eH}^{\mathrm{M}}$, $\triangle\boldsymbol{\beta}_{eH}^{\mathrm{I}}$) and the nodal displacement increments ($\triangle\mathbf{q}_{eH}^{\mathrm{E}}$, $\triangle\mathbf{q}_{eH}^{\mathrm{I}}$). Details of numerical integration schemes for the constitutive equations are provided in [1,2]. An iterative solution process is invoked for Eq. (20) to evaluate the stresses, given the nodal displacement increments. Thus the correction to $\triangle\boldsymbol{\beta}$ in the ith iteration is obtained as

$$\{\triangle\boldsymbol{\beta}_{eH}^{\mathrm{M}}\}=\{\triangle\boldsymbol{\beta}_{eH}^{\mathrm{M}}\}^{i}+\{d\boldsymbol{\beta}_{eH}^{\mathrm{M}}\}^{i},\quad \{\triangle\boldsymbol{\beta}_{eH}^{\mathrm{I}}\}=\{\triangle\boldsymbol{\beta}_{eH}^{\mathrm{I}}\}^{i}+\{d\boldsymbol{\beta}_{eH}^{\mathrm{I}}\}^{i}. \tag{22}$$

The kinematic Eq. (20) may be linearized with respect to $\triangle\boldsymbol{\beta}$ to yield:

$$\begin{bmatrix}\mathbf{H}_{\mathrm{M}} & \mathbf{0}\\ \mathbf{0} & \mathbf{H}_{\mathrm{I}}\end{bmatrix}\begin{Bmatrix}\mathrm{d}\boldsymbol{\beta}_{eH}^{\mathrm{M}}\\ \mathrm{d}\boldsymbol{\beta}_{eH}^{\mathrm{I}}\end{Bmatrix}^{i}=\begin{bmatrix}\mathbf{G}_{\mathrm{E}} & -\mathbf{G}_{\mathrm{MI}}\\ \mathbf{0} & \mathbf{G}_{\mathrm{II}}\end{bmatrix}\begin{Bmatrix}\triangle\mathbf{q}_{eH}^{\mathrm{E}}\\ \triangle\mathbf{q}_{eH}^{\mathrm{I}}\end{Bmatrix}-\begin{Bmatrix}\int_{\Omega_e^{\mathrm{M}}}[\mathbf{P}^{\mathrm{M}}]^{\mathrm{T}}\{\triangle\boldsymbol{\epsilon}_{eH}^{\mathrm{M}}\}^{i}\,\mathrm{d}\Omega\\ \int_{\Omega_e^{\mathrm{I}}}[\mathbf{P}^{\mathrm{I}}]^{\mathrm{T}}\{\triangle\boldsymbol{\epsilon}_{eH}^{\mathrm{I}}\}^{i}\,\mathrm{d}\Omega\end{Bmatrix}\quad\forall e=1,\ldots,N, \tag{23}$$

where

$$[\mathbf{H}_{\mathrm{M}}]=\int_{\Omega_e^{\mathrm{M}}}[\mathbf{P}^{\mathrm{M}}]^{\mathrm{T}}[\mathbf{S}^{\mathrm{M}}][\mathbf{P}^{\mathrm{M}}]\ \mathrm{d}\Omega,\quad [\mathbf{H}_{\mathrm{I}}]=\int_{\Omega_e^{\mathrm{I}}}[\mathbf{P}^{\mathrm{I}}]^{\mathrm{T}}[\mathbf{S}^{\mathrm{I}}][\mathbf{P}^{\mathrm{I}}]\ \mathrm{d}\Omega, \tag{24}$$

$$[\mathbf{G}_{\mathrm{E}}]=\int_{\partial\Omega_e^{\mathrm{E}}}[\mathbf{P}^{\mathrm{M}}]^{\mathrm{T}}[\mathbf{n}^{\mathrm{E}}][\mathbf{L}^{\mathrm{E}}]\ \mathrm{d}\Omega,\quad [\mathbf{G}_{\mathrm{MI}}]=\int_{\partial\Omega_e^{\mathrm{I}}}[\mathbf{P}^{\mathrm{M}}]^{\mathrm{T}}[\mathbf{n}^{\mathrm{I}}][\mathbf{L}^{\mathrm{I}}]\ \mathrm{d}\Omega,\quad [\mathbf{G}_{\mathrm{II}}]=\int_{\partial\Omega_e^{\mathrm{I}}}[\mathbf{P}^{\mathrm{I}}]^{\mathrm{T}}[\mathbf{n}^{\mathrm{I}}][\mathbf{L}^{\mathrm{I}}]\ \mathrm{d}\Omega, \tag{25}$$

where $[\mathbf{S}]$ is the instantaneous compliance tensor (elastic for the inclusion and elastic–plastic for the matrix). A quasi-Newton iterative solution procedure is used to solve Eq. (23), in which the traction reciprocity conditions (21) are solved for given nodal displacement increments. Likewise, with known stress increments, displacements are solved iteratively in the jth iteration of Eq. (21) as

$$\{\triangle\mathbf{q}_{eH}^{\mathrm{E}}\}=\{\triangle\mathbf{q}_{eH}^{\mathrm{E}}\}^{j}+\{\mathrm{d}\mathbf{q}_{eH}^{\mathrm{E}}\}^{j}\quad\text{and}\quad\{\triangle\mathbf{q}_{eH}^{\mathrm{I}}\}=\{\triangle\mathbf{q}_{eH}^{\mathrm{I}}\}^{j}+\{\mathrm{d}\mathbf{q}_{eH}^{\mathrm{I}}\}^{j}. \tag{26}$$

Substituting Eq. (23) in the linearized global traction reciprocity Eq. (21), with respect to $\{\triangle\mathbf{q}\}$, yields the matrix equation

$$\sum_{e=1}^{N}[K_e]\begin{Bmatrix}\mathrm{d}\mathbf{q}_{eH}^{\mathrm{E}}\\ \mathrm{d}\mathbf{q}_{eH}^{\mathrm{I}}\end{Bmatrix}^{j}=\sum_{e=1}^{N}\begin{bmatrix}\mathbf{G}_{\mathrm{E}} & -\mathbf{G}_{\mathrm{MI}}\\ \mathbf{0} & \mathbf{G}_{\mathrm{II}}\end{bmatrix}^{\mathrm{T}}\begin{bmatrix}\mathbf{H}_{\mathrm{M}} & \mathbf{0}\\ \mathbf{0} & \mathbf{H}_{\mathrm{I}}\end{bmatrix}\begin{bmatrix}\mathbf{G}_{\mathrm{E}} & -\mathbf{G}_{\mathrm{MI}}\\ \mathbf{0} & \mathbf{G}_{\mathrm{II}}\end{bmatrix}\begin{Bmatrix}\mathrm{d}\mathbf{q}_{eH}^{\mathrm{E}}\\ \mathrm{d}\mathbf{q}_{eH}^{\mathrm{I}}\end{Bmatrix}^{j}$$
$$=\sum_{e=1}^{N}\begin{Bmatrix}\int_{\Gamma_{\mathrm{te}}}[\mathbf{L}^{\mathrm{M}}]^{\mathrm{T}}\{\bar{\mathbf{t}}+\triangle\bar{\mathbf{t}}\}\,\mathrm{d}\Omega\\ \mathbf{0}\end{Bmatrix}$$
$$-\sum_{e=1}^{N}\begin{bmatrix}\int_{\partial\Omega_e^{\mathrm{E}}}[\mathbf{L}^{\mathrm{E}}]^{\mathrm{T}}[\mathbf{n}^{\mathrm{E}}]^{\mathrm{T}}[\mathbf{P}^{\mathrm{M}}]\,\mathrm{d}\Omega & \mathbf{0}\\ -\int_{\partial\Omega_e^{\mathrm{I}}}[\mathbf{L}^{\mathrm{I}}]^{\mathrm{T}}[\mathbf{n}^{\mathrm{I}}]^{\mathrm{T}}[\mathbf{P}^{\mathrm{M}}]\,\mathrm{d}\Omega & \int_{\partial\Omega_e^{\mathrm{I}}}[\mathbf{L}^{\mathrm{I}}]^{\mathrm{T}}[\mathbf{n}^{\mathrm{I}}]^{\mathrm{T}}[\mathbf{P}^{\mathrm{I}}]\,\mathrm{d}\Omega\end{bmatrix}\begin{Bmatrix}\boldsymbol{\beta}_{eH}^{\mathrm{M}}+\triangle\boldsymbol{\beta}_{eH}^{\mathrm{M}}\\ \beta_{eH}^{\mathrm{I}}+\triangle\boldsymbol{\beta}_{eH}^{\mathrm{I}}\end{Bmatrix}^{j}. \tag{27}$$

With known traction and displacement increments on Γ_{te} and Γ_{ue} respectively, the linearized global traction reciprocity condition (27) is solved iteratively.

2.2. An example of stress function convergence

The assumed forms of stress functions in Eqs. (13) and (14) are compared with a known analytical form of solution provided in [36] for the problem of an elliptical void in an infinite matrix. The matrix is loaded in simple tension at any arbitrary angle to the axes of the ellipse. This comparison establishes the effectiveness and also the generality of the assumed stress functions for a wide variety of problems. The stress function is available in a complex form in [36] as

$$\Phi^{\mathrm{M}}_{\mathrm{exact}} = Re(\bar{z}(Ac\ \cosh\zeta + Bc\ \sinh\zeta) + C\zeta + Dc^2\ \cosh 2\zeta + Ec^2\ \sinh 2\zeta), \tag{28}$$

where A, B, C, D, E, and c are constants. As shown in Appendix A, the stress function in the matrix can be recast in the form:

$$\begin{aligned}\Phi^{m}_{\mathrm{exact}} \approx\ & A^*x^2 + B^*y^2 + C^*x^2(1 - 2m/f^2 + 2m^2/f^4 + \mathrm{O}(1/f^6)) \\ & + D^*y^2(1 + 2m/f^2 - 2m^2/f^4 + \mathrm{O}(1/f^6)) + E^*x^2(1 + 4m/f^2 + 8m^2/f^4 + \mathrm{O}(1/f^6)) \\ & + F^*y^2(1 - 4m/f^2 + 8m^2/f^4 + \mathrm{O}(1/f^6)) + G^*(H^* + \log f + \mathrm{O}(1/f^4)).\end{aligned} \tag{29}$$

Comparing Eq. (29) with Eqs. (14) and (13), it can be seen that the reciprocal stress functions used in VCFEM can indeed capture the leading order characteristics of the analytical stress function for this problem.

2.3. Stability and convergence of VCFEM

Various aspects of stability in hybrid and mixed methods for multi-field saddle point problems have been discussed in a number of papers, viz. [26–33]. Following the arguments explained in these studies, the stability conditions of the multi-field variational problem in VCFEM are concluded to depend on the energy functionals, constituted of ${}_e\mathsf{a}^{\mathrm{M/I}}(\boldsymbol{\sigma}^{\mathrm{M/I}}_{eH}, \boldsymbol{\sigma}^{\mathrm{M/I}}_{eH})$ and ${}_e\mathsf{b}^{\mathrm{M/I}}_{\mathrm{E/I}}(\mathbf{u}^{\mathrm{E/I}}_{eH}, \boldsymbol{\sigma}^{\mathrm{M/I}}_{eH})$, being positive for all nontrivial stresses and non-rigid body displacements.

The bilinear form ${}_e\mathsf{a}^{\mathrm{M/I}}$ represents the element complimentary energy and may be represented in terms of the stress coefficients from Eqs. (16), (17) and (7) as

$${}_e\mathsf{a}^{\mathrm{M/I}}\left(\boldsymbol{\sigma}^{\mathrm{M/I}}_{eH}, \boldsymbol{\sigma}^{\mathrm{M/I}}_{eH}\right) = \left\langle \boldsymbol{\beta}^{\mathrm{M/I}}_{eH}, \mathbf{H}_{M/I}\boldsymbol{\beta}^{\mathrm{M/I}}_{eH}\right\rangle \quad \forall \boldsymbol{\sigma}^{\mathrm{M/I}}_{eH} \in \mathscr{T}^{\mathrm{M/I}}_{eH}, \tag{30}$$

where $\langle\cdot\rangle$ is the L_2 vector inner product. Thus ${}_e\mathsf{a}^{\mathrm{M/I}}$ is positive for all $\boldsymbol{\sigma} \neq 0$ if the matrix $[\mathbf{H}]$ is positive definite. From the definition of $[\mathbf{H}]$ in Eq. (23) it is inferred that the necessary conditions for it to be positive definite is that the tangent operator $[\mathbf{S}(x,y)]$ be positive definite and that the finite-dimensional subspaces $\mathscr{T}^{\mathrm{M/I}}_{eH}$ be spanned uniquely by the basis functions $[\mathbf{P}^{\mathrm{M}}(x,y)]$ and $[\mathbf{P}^{\mathrm{I}}(x,y)]$. The first condition is valid for all tangent operators $[\mathbf{S}(x,y)]$ in elasticity and hardening plasticity. The second conditions is satisfied by assuring linear independence of the columns of basis functions $[\mathbf{P}^{\mathrm{M}}(x,y)]$ and $[\mathbf{P}^{\mathrm{I}}(x,y)]$, which also guarantees the invertibility of $[\mathbf{H}]$. However, an additional conditions for stability are required to guarantee non-zero stress parameters $\boldsymbol{\beta}^{\mathrm{M/I}}_{eH}$ in ${}_e\mathsf{a}^{\mathrm{M/I}}$ for all non-rigid body boundary displacement fields $\mathbf{u}^{\mathrm{E/I}}_{eH}$. Careful choice of the dimensions of the stress and displacement subspaces are required for this purpose, as discussed later in this section. The second bilinear form in the energy functional ${}_e\mathsf{b}^{\mathrm{M/I}}_{\mathrm{E/I}}$ is represented in terms of the stress and displacement parameters from Eqs. (16), (18), (5) and (7) as

$$\begin{aligned}&{}_e\mathsf{b}^{\mathrm{M}}_{\mathrm{E}}(\boldsymbol{\sigma}^{\mathrm{M}}_{eH}, \mathbf{u}^{\mathrm{E}}_{eH}) = \left\langle \mathbf{G}_{\mathrm{E}}\ \mathbf{q}^{\mathrm{E}}_{eH}, \boldsymbol{\beta}^{\mathrm{M}}_{eH}\right\rangle, \quad {}_e\mathsf{b}^{\mathrm{M}}_{\mathrm{I}}(\boldsymbol{\sigma}^{\mathrm{M}}_{eH}, \mathbf{u}^{\mathrm{I}}_{eH}) = \left\langle \mathbf{G}_{\mathrm{MI}}\ \mathbf{q}^{\mathrm{I}}_{eH}, \boldsymbol{\beta}^{\mathrm{M}}_{eH}\right\rangle, \\ &{}_e\mathsf{b}^{\mathrm{I}}_{\mathrm{I}}(\boldsymbol{\sigma}^{\mathrm{I}}_{eH}, \mathbf{u}^{\mathrm{I}}_{eH}) = \left\langle \mathbf{G}_{\mathrm{II}}\ \mathbf{q}^{\mathrm{I}}_{eH}, \boldsymbol{\beta}^{\mathrm{I}}_{eH}\right\rangle \quad \forall \boldsymbol{\sigma}^{\mathrm{M/I}}_{eH} \in \mathscr{T}^{\mathrm{M/I}}_{eH} \quad \text{and} \quad \forall \mathbf{u}^{\mathrm{E/I}}_{eH} \in \mathscr{V}^{\mathrm{E/I}}_{eH}.\end{aligned} \tag{31}$$

For rigid body displacement modes $\mathbf{u}^{\mathrm{E/I}}$ on the element boundary and interface, it is necessary that ${}_{eH}b^{\mathrm{M/I}}_{\mathrm{E/I}}$ go to zero. Thus, the displacement fields in the space ${}^{\perp}\mathscr{V}^{\mathrm{E/I}}_{eH}$ perpendicular to the subspace of rigid body modes, should strictly produce positive strain energies. This is referred to as the discrete L–B–B condition [26,31], and ensures the stability of the multi-field variational problems such as in VCFEM.

These stability conditions for a two phase Voronoi cell element with a void or inclusion are now derived. The strain energy in a Voronoi cell element with a void comprises of the energy in the matrix phase alone and may be expressed from Eqs. (7), (31), (16) and (23) as

$$\begin{aligned}(\mathrm{SE})_e^{\mathrm{M}} &= {}_e\mathsf{a}_e^{\mathrm{M}}(\boldsymbol{\sigma}_{eH}^{\mathrm{M}},\boldsymbol{\sigma}_{eH}^{\mathrm{M}}) = {}_e\mathsf{b}_{\mathrm{E}}^{\mathrm{M}}(\boldsymbol{\sigma}_{eH}^{\mathrm{M}},\mathbf{u}_{eH}^{\mathrm{E}}) - {}_e\mathsf{b}_{\mathrm{I}}^{\mathrm{M}}(\boldsymbol{\sigma}_{eH}^{\mathrm{M}},\mathbf{u}_{eH}^{\mathrm{I}})\\ &= \left\langle \mathbf{G}_{\mathrm{E}}\ \mathbf{q}_{eH}^{\mathrm{E}},\boldsymbol{\sigma}_{eH}^{\mathrm{M}}\right\rangle - \left\langle \mathbf{G}_{\mathrm{MI}}\ \mathbf{q}_{eH}^{\mathrm{I}},\boldsymbol{\sigma}_{eH}^{\mathrm{M}}\right\rangle = \left\langle (\mathbf{G}_{\mathrm{E}}\ \mathbf{q}_{eH}^{\mathrm{E}} - \mathbf{G}_{\mathrm{MI}}\ \mathbf{q}_{eH}^{\mathrm{I}}),\boldsymbol{\sigma}_{eH}^{\mathrm{M}}\right\rangle\\ &= \left\langle \begin{bmatrix}\mathbf{G}_{\mathrm{E}} & -\mathbf{G}_{\mathrm{MI}}\end{bmatrix}\begin{Bmatrix}\mathbf{q}_{eH}^{\mathrm{E}}\\ \mathbf{q}_{eH}^{\mathrm{I}}\end{Bmatrix}, [\mathbf{H}_{\mathrm{M}}]^{-1}\begin{bmatrix}\mathbf{G}_{\mathrm{E}} & -\mathbf{G}_{\mathrm{MI}}\end{bmatrix}\begin{Bmatrix}\mathbf{q}_{eH}^{\mathrm{E}}\\ \mathbf{q}_{eH}^{\mathrm{I}}\end{Bmatrix}\right\rangle\\ &= \left\langle \left[\mathbf{G}^{\mathrm{void}}\right]\{\mathbf{Q}\}, [\mathbf{H}_{\mathrm{M}}]^{-1}\left[\mathbf{G}^{\mathrm{void}}\right]\{\mathbf{Q}\}\right\rangle \end{aligned} \tag{32}$$

$[\mathbf{G}^{\mathrm{void}}]$ is an $n_\beta^{\mathrm{M}} \times (n_q^{\mathrm{E}} + n_q^{\mathrm{I}})$ rectangular matrix, where $n_\beta^{\mathrm{M}} = \dim(\mathscr{T}_{eH}^{\mathrm{M}})$, $n_q^{\mathrm{E}} = \dim(\mathscr{V}_{eH}^{\mathrm{E}})$ and $n_q^{\mathrm{I}} = \dim(\mathscr{V}_{eH}^{\mathrm{I}})$. Since $[\mathbf{H}_{\mathrm{M}}]$ is positive definite, the strain energy in the matrix of the Voronoi cell element vanishes for zero stress fields in the matrix, and consequently in Eq. (32)

$$(\mathrm{SE})_e^{\mathrm{M}} = 0 \quad \Longleftrightarrow \quad \left[\mathbf{G}^{\mathrm{void}}\right]\{\mathbf{Q}\} = 0. \tag{33}$$

A necessary condition of stability is thus written from Eq. (33) as

$$[\mathbf{G}^{\mathrm{void}}]\{\mathbf{Q}\} = [\mathbf{U}][\boldsymbol{\lambda}][\mathbf{V}]\{\mathbf{Q}\} \neq 0 \quad \forall \mathbf{Q} \cap \mathbf{Q}^{\mathrm{rb}} = \emptyset, \tag{34}$$

where $\mathbf{Q}^{\mathrm{rb}}$ correspond to the three rigid body modes of displacement for 2D problems. The matrices $[\mathbf{U}]$ and $[\mathbf{V}]$, whose columns are the eigenvectors of $[\mathbf{G}^{\mathrm{void}}][\mathbf{G}^{\mathrm{void}}]^{\mathrm{T}}$ and $[\mathbf{G}^{\mathrm{void}}]^{\mathrm{T}}[\mathbf{G}^{\mathrm{void}}]$ respectively, are orthonormal matrices obtained by singular value decomposition of $[\mathbf{G}^{\mathrm{void}}]$. $[\boldsymbol{\lambda}]$ is a rectangular matrix with positive entries on the diagonal corresponding to the square roots of the non-zero eigenvalues of both $[\mathbf{G}^{\mathrm{void}}][\mathbf{G}^{\mathrm{void}}]^{\mathrm{T}}$ and $[\mathbf{G}^{\mathrm{void}}]^{\mathrm{T}}[\mathbf{G}^{\mathrm{void}}]$. Premultiplying both sides of Eq. (34) by $[\mathbf{U}]^{-1}$ yields

$$[\boldsymbol{\lambda}][\mathbf{V}]\{\mathbf{Q}\} = [\boldsymbol{\lambda}]\{\mathbf{Q}^*\} = 0. \tag{35}$$

Since the columns of $[\mathbf{V}]$ are linearly independent, the above equation can only be satisfied for either trivial or rigid body solutions of the boundary displacement, and hence the necessary condition. Eq. (33) also leads to the L–B–B condition for rank sufficiency of a Voronoi cell element with a void. Positive singular values of $[\boldsymbol{\lambda}]$ implies that the strain energy associated with the stress field solution $\boldsymbol{\sigma}_{eH}^{\mathrm{M}}(\mathbf{u}_{eH}^{\mathrm{E}},\mathbf{u}_{eH}^{\mathrm{I}})$ associated for non-rigid body displacement fields $\mathbf{u}_{eH}^{\mathrm{E/I}} \in^{\perp} \mathscr{V}_{eH}^{\mathrm{E/I}} \forall^{\perp} \mathscr{V}_{eH}^{\mathrm{E/I}} \cap^{\mathrm{rb}} \mathscr{V}_{eH}^{\mathrm{E/I}} = \emptyset$ is strictly non-zero. From Eqs. (7) and (33), the L–B–B condition may be stated as, $\exists \gamma > 0$ such that

$$\sup_{\forall \mathbf{u}_{eH}^{\mathrm{E/I}} \in^{\perp} \mathscr{V}_{eH}^{\mathrm{E/I}}} \frac{{}_e\mathsf{b}_{\mathrm{E}}^{\mathrm{M}}(\boldsymbol{\sigma}_{eH}^{\mathrm{M}},\mathbf{u}_{eH}^{\mathrm{E}}) - {}_e\mathsf{b}_{\mathrm{I}}^{\mathrm{M}}(\boldsymbol{\sigma}_{eH}^{\mathrm{M}},\mathbf{u}_{eH}^{\mathrm{I}})}{\|\mathbf{u}_{eH}^{\mathrm{E}} \otimes \mathbf{u}_{eH}^{\mathrm{I}}\|} \geqslant \gamma \|\boldsymbol{\sigma}_{eH}^{\mathrm{M}}\| \quad \forall \boldsymbol{\sigma}_{eH}^{\mathrm{M}} \in \mathscr{T}_{eH}^{\mathrm{M}}, \tag{36}$$

where $\|\cdot\|$ are metric norms defined in the respective subspaces. The corresponding necessary condition for stability in terms of the matrix dimensions become

$$n_\beta^{\mathrm{M}} > n_q^{\mathrm{E}} + n_q^{\mathrm{I}} - 3. \tag{37}$$

The sufficient condition for stability is established by ensuring that the eigen values in $[\boldsymbol{\lambda}]$ are positive, and is enforced at the solution stage.

For the composite Voronoi cell element with an embedded inclusion, positiveness of the total strain energy $(\mathrm{SE})_e = (\mathrm{SE})_e^{\mathrm{M}} + (\mathrm{SE})_e^{\mathrm{I}}$ can be stated in a similar manner as, $\exists \gamma > 0$ such that

$$\begin{aligned}&\sup_{\forall \mathbf{u}_{eH}^{\mathrm{E}} \in^{\perp} \mathscr{V}_{eH}^{\mathrm{E}}} \frac{{}_e\mathsf{b}_{\mathrm{E}}^{\mathrm{M}}(\boldsymbol{\sigma}_{eH}^{\mathrm{M}},\mathbf{u}_{eH}^{\mathrm{E}})}{\|\mathbf{u}_{eH}^{\mathrm{E}}\|} \geqslant \gamma \|\boldsymbol{\sigma}_{eH}^{\mathrm{M}}\| \quad \forall \boldsymbol{\sigma}_{eH}^{\mathrm{M}} \in \mathscr{T}_{eH}^{\mathrm{M}},\\ &\sup_{\forall \mathbf{u}_{eH}^{\mathrm{I}} \in^{\perp} \mathscr{V}_{eH}^{\mathrm{I}}} \frac{{}_e\mathsf{b}_{\mathrm{I}}^{\mathrm{I}}(\boldsymbol{\sigma}_{eH}^{\mathrm{I}},\mathbf{u}_{eH}^{\mathrm{I}})}{\|\mathbf{u}_{eH}^{\mathrm{I}}\|} \geqslant \gamma \|\boldsymbol{\sigma}_{eH}^{\mathrm{I}}\| \quad \forall \boldsymbol{\sigma}_{eH}^{\mathrm{I}} \in \mathscr{T}_{eH}^{\mathrm{I}}. \end{aligned} \tag{38}$$

The corresponding L–B–B condition or the necessary condition for stability of a composite Voronoi cell element [1,2] are

$$n_\beta^{\mathrm{M}} > n_q^{\mathrm{E}} - 3 \quad \text{and} \quad n_\beta^{\mathrm{I}} > n_q^{\mathrm{I}} - 3. \tag{39}$$

As explained in [26,27], the above conditions are sufficient to guarantee the existence of solution and its convergence for multi-field saddle point problem posed by the Voronoi cell FEM with elastic constituents. Additionally, as explained in [26,27], the convergence criteria for the incremental problem in terms of $(\triangle\boldsymbol{\sigma}_e, \triangle\mathbf{u}_e)$ may be written as: $\exists C_1 > 0$ such that

$$\sum_{e=1}^{N}\left[\|(\triangle\boldsymbol{\sigma}_e^{\mathrm{M}}. - \triangle\boldsymbol{\sigma}_{eH}^{\mathrm{M}})\otimes(\triangle\boldsymbol{\sigma}_e^{\mathrm{I}} - \triangle\boldsymbol{\sigma}_{eH}^{\mathrm{I}})\|_{\mathscr{T}} + \|(\triangle\mathbf{u}_e^{\mathrm{E}} - \triangle\mathbf{u}_{eH}^{\mathrm{E}})\otimes(\triangle\mathbf{u}_e^{\mathrm{I}} - \triangle\mathbf{u}_{eH}^{\mathrm{I}})\|_{\mathscr{V}}\right]$$
$$\leqslant C_1\sum_{e=1}^{N}\left[\inf_{\forall\tau_e^{\mathrm{M/I}}\in\mathscr{T}_{eH}^{\mathrm{M/I}},\forall v_e^{\mathrm{E/I}}\in\mathscr{V}_{eH}^{\mathrm{E/I}}}\|(\triangle\boldsymbol{\sigma}_e^{\mathrm{M}} - \boldsymbol{\tau}_e^{\mathrm{M}})\otimes(\triangle\boldsymbol{\sigma}_e^{\mathrm{I}} - \boldsymbol{\tau}_e^{\mathrm{I}})\|_{\mathscr{T}} + \|(\triangle\mathbf{u}_e^{\mathrm{E}} - \mathbf{v}_e^{\mathrm{E}})\otimes(\triangle\mathbf{u}_e^{\mathrm{I}} - \mathbf{v}_e^{\mathrm{I}})\|_{\mathscr{V}}\right]. \tag{40}$$

Detailed procedures for estimation of the norms in the stress and displacement subspaces are discussed in Section 3.

2.3.1. Numerical implementation of stability conditions

As discussed in the previous section, the linear independence of the columns of influence matrices $[\mathbf{P}^{\mathrm{M}}]$ and $[\mathbf{P}^{\mathrm{I}}]$ is necessary for positiveness of the bilinear forms ${}_e\mathrm{a}^{\mathrm{M/I}}$. For pure polynomial expansions of stress functions e.g. $[\mathbf{P}^{\mathrm{I}}_{\mathrm{poly}}]$, this is natural. However, for stress functions with the reciprocal terms e.g. $[\mathbf{P}^{\mathrm{M}}]$, some of the reciprocal terms may be linearly dependent on the polynomial terms. For example, in the case of the stress function for a circular void ($f = r/a$, $\Phi_{\mathrm{M}}^{\mathrm{poly}} = \sum_{p,q}\triangle\beta_{pq}x^p y^q\ \forall p+q = 2..4$, and $\Phi_{\mathrm{M}}^{\mathrm{rec}} = \sum_{p,q,i}\triangle\beta_{pqi}(x^p y^q)/(f^p + q + i - 1)\ \forall p+q = 2..4$ and $i = 1..3$), the basis function y^2/f^2 corresponding to the stress coefficient $\triangle\beta_{021}$ can be written as

$$\frac{y^2}{f^2} = \frac{r^2 - x^2}{f^2} = \frac{a^2 f^2 - x^2}{f^2} = a^2 - \frac{x^2}{f^2}. \tag{41}$$

The stress field generated from the basis function y^2/f^2 is thus represented by the spanning function x^2/f^2, giving rise to linear dependence. To avert this, the rank of the influence functions e.g. $[\mathbf{P}^{\mathrm{M}}]$ is determined apriori by noting the diagonal matrix resulting from a Cholesky factorization of the square matrix

$$[\mathbf{H}_{\mathrm{M}}^*] = \int_{\Omega_e}[\mathbf{P}^{\mathrm{M}}]^{\mathrm{T}}[\mathbf{P}^{\mathrm{M}}]\ \mathrm{d}\Omega. \tag{42}$$

The matrix $[\mathbf{H}_{\mathrm{M}}^*]$ will be positive definite for linearly independent columns in $[\mathbf{P}^{\mathrm{M}}]$. Thus nearly dependent terms in the columns result in very small pivots during the factorization process. These terms in the stress function are dropped to prevent numerical inaccuracies in the inversion of $[\mathbf{H}_{\mathrm{M}}]$ matrix.

A singular value decomposition of the matrix $[\mathbf{G}_{\mathrm{E}}] - [\mathbf{G}_{\mathrm{MI}}]$ and matrices $[\mathbf{G}_{\mathrm{E}}]$, $[\mathbf{G}_{\mathrm{II}}]$ are performed for Voronoi cell elements with voids and inclusions respectively to satisfy the discrete L–B–B conditions. The number of degrees of freedom n_β^{M} and n_β^{I} in the stress functions Φ^{M} and Φ^{I} are chosen to satisfy Eqs. (37) and (39). Zero singular values in the diagonal of the resulting $[\boldsymbol{\lambda}]$ matrix are removed by enriching the corresponding stress function with polynomial terms. Additionally, extremely small eigen-values in $[\boldsymbol{\lambda}]$ may result in inaccurate displacements, as noted in [26]. This problem was observed during displacement adaptations at the interfaces. A simple procedure corresponding to the constraining of selected displacement values based on the singular value decomposition of $[\mathbf{G}_{\mathrm{MI}}]$ or $[\mathbf{G}_{\mathrm{II}}]$ is carried out. The procedure involves re-writing the matrix multiplication as

$$[\mathbf{G}]\{\mathbf{q}^{\mathrm{I}}\} = [\mathbf{U}][\boldsymbol{\lambda}][\mathbf{V}]\{\mathbf{q}^{\mathrm{I}}\} = [\mathbf{U}][\boldsymbol{\lambda}]\{\mathbf{q}^{\mathrm{I}}\}_{\mathrm{alt}} = [\mathbf{G}]_{\mathrm{alt}}\{\mathbf{q}^{\mathrm{I}}\}_{\mathrm{alt}}. \tag{43}$$

Elements in $\{\mathbf{q}_{\mathrm{alt}}^{\mathrm{I}}\}$ corresponding to small eigen-values in $[\boldsymbol{\lambda}]$ are preconstrained to a zero value. This procedure decreases the dimensions of $\mathscr{V}_{eH}^{\mathrm{I}}$ and consequently results in a loss of accuracy as seen in the accumulated error during adaptations. The discrete L–B–B conditions are re-checked with enrichment of the displacement functions and stress functions during the adaptive phase of the calculations. Detailed

discussions of the various numerical integration techniques for element energy functionals and solution methods for nonlinear system of equations can be found in [4].

3. Error measures in VCFEM for adaptivity

As seen from the Euler equations (6) and (8), kinematic equations in each phase and the traction reciprocities on the element boundary and interface of each Voronoi cell element are satisfied in a weak sense. Consequently, the major sources of error in VCFEM arise from the lack of adequate representation of variables in the discrete subspaces $\mathscr{T}^{\mathrm{M}}_{eH}, \mathscr{T}^{\mathrm{I}}_{eH}, \mathscr{V}^{\mathrm{E}}_{eH}$ and $\mathscr{V}^{\mathrm{I}}_{eH}$. In accordance with the convergence criteria stated in Eq. (40), error measures are represented in terms of metrics or norms $\|\cdot\|_{\mathscr{T}}$ and $\|\cdot\|_{\mathscr{V}}$ in the Hilbert spaces $\mathscr{T}$ and $\mathscr{V}$, respectively.

To improve the convergence of solutions in the adaptive procedure, the finite element approximation subspaces $\mathscr{T}^{\mathrm{M/I}}_{eH}$ and $\mathscr{V}^{\mathrm{E/I}}_{eH}$ are augmented by basis vectors in the orthogonal subspaces ${}^{\perp}\mathscr{T}^{\mathrm{M/I}}_{eH}$ and ${}^{\perp}\mathscr{V}^{\mathrm{E/I}}_{eH}$. The orthogonality conditions for respective elements in these spaces are expressed as

$$\int_{\Omega_e^{\mathrm{M/I}}} {}^{*}\delta\boldsymbol{\sigma}_{eH} \cdot [\mathbf{S}] \cdot \boldsymbol{\sigma}_{eH} \; \mathrm{d}\Omega = 0, \; \forall(\boldsymbol{\sigma}_{eH}, {}^{*}\delta\boldsymbol{\sigma}_{eH}) \in \left(\mathscr{T}^{\mathrm{M/I}}_{eH}, {}^{\perp}\mathscr{T}^{\mathrm{M/I}}_{eH}\right) \tag{44}$$

and

$$\int_{\partial\Omega_e^{\mathrm{E/I}}} \delta\mathbf{u}^{\mathrm{E/I}}_{eH} \cdot {}^{*}\delta\mathbf{u}^{\mathrm{E/I}}_{eH} \; \mathrm{d}\Omega = 0, \; \forall(\delta\mathbf{u}_{eH}, {}^{*}\delta\mathbf{u}_{eH}) \in \left(\mathscr{V}^{\mathrm{E/I}}_{eH}, {}^{\perp}\mathscr{V}^{\mathrm{E/I}}_{eH}\right). \tag{45}$$

The motivation to this is that the exact solution spaces are better spanned by the augmented basis functions such that $(\mathscr{T}_{eH} \oplus^{\perp} \mathscr{T}_{eH}) \otimes (\mathscr{V}_{eH} \oplus^{\perp} \mathscr{V}_{eH}) \to \mathscr{T}_e \otimes \mathscr{V}_e$, $\forall\boldsymbol{\sigma} \otimes \mathbf{u} \in \mathscr{T}_e \otimes \mathscr{V}_e$. The error measures and criteria in terms of the stresses and displacements in Eq. (40), are established from the incremental weak forms in Eq. (10). Assume that $\mathrm{d}\boldsymbol{\sigma}^{\mathrm{M/I}}_e \in \mathscr{T}^{\mathrm{M/I}}_e$ is the correction to incremented stresses $(\boldsymbol{\sigma} + \triangle\boldsymbol{\sigma})^{\mathrm{M/I}}_{eH}$ in the approximation space $\mathscr{T}^{\mathrm{M/I}}_{eH}$ i.e. $(\boldsymbol{\sigma} + \triangle\boldsymbol{\sigma})^{\mathrm{M/I}}_{eH} + \mathrm{d}\boldsymbol{\sigma}^{\mathrm{M/I}}_e = (\boldsymbol{\sigma} + \triangle\boldsymbol{\sigma})^{\mathrm{M/I}}_e$. The enriched forms of Eq. (10) may be rewritten in terms of the corrections as

$$\sum_{e=1}^{N} {}_e\mathrm{b}^{\mathrm{M}}_{\mathrm{E}}(\mathrm{d}\boldsymbol{\sigma}^{\mathrm{M}}_e, \delta\mathbf{u}^{\mathrm{E}}_e) = \sum_{e=1}^{N} \left\{ {}_e\mathrm{f}^{\mathrm{E}}(\delta\mathbf{u}^{\mathrm{E}}_e) - {}_e\mathrm{b}^{\mathrm{M}}_{\mathrm{E}}((\boldsymbol{\sigma}^{\mathrm{M}}_{eH} + \triangle\boldsymbol{\sigma}^{\mathrm{M}}_{eH}), \delta\mathbf{u}^{\mathrm{E}}_e) \right\} \quad \forall\delta\mathbf{u}^{\mathrm{E}}_e \in \mathscr{V}^{\mathrm{E}}_e, \; \forall e, \tag{46}$$

$${}_e\mathrm{b}^{\mathrm{I}}_{\mathrm{I}}((\boldsymbol{\sigma}^{\mathrm{I}}_{eH} + \triangle\boldsymbol{\sigma}^{\mathrm{I}}_{eH} + \mathrm{d}\boldsymbol{\sigma}^{\mathrm{I}}_e), \delta\mathbf{u}^{\mathrm{I}}_e) - {}_e\mathrm{b}^{\mathrm{M}}_{\mathrm{I}}\left((\boldsymbol{\sigma}^{\mathrm{M}}_e + \triangle\boldsymbol{\sigma}^{\mathrm{M}}_e + \mathrm{d}\boldsymbol{\sigma}^{\mathrm{M}}_e), \delta\mathbf{u}^{\mathrm{I}}_e\right) = 0 \quad \forall\delta\mathbf{u}^{\mathrm{I}}_e \in \mathscr{V}^{\mathrm{I}}_e, \; \forall e. \tag{47}$$

The exact displacement solutions $\delta\mathbf{u}^{\mathrm{E/I}}_e \in \mathscr{V}^{\mathrm{E/I}}_e$ satisfying Eqs. (46) and (47) results from augmenting the displacement approximations $\delta\mathbf{u}^{\mathrm{E/I}}_{eH} \in \mathscr{V}^{\mathrm{E/I}}_{eH}$ by a set of enrichment functions ${}^{*}\delta\mathbf{u}^{\mathrm{E/I}}_{eH} \in^{\perp} \mathscr{V}^{\mathrm{E/I}}_{eH}$. Substituting $\delta\mathbf{u}^{\mathrm{E/I}}_e = \delta\mathbf{u}^{\mathrm{E/I}}_{eH} + {}^{*}\delta\mathbf{u}^{\mathrm{E/I}}_{eH}$ in Eqs. (46) and (47) yields

$$\begin{aligned}\sum_{e=1}^{N} {}_e\mathrm{b}^{\mathrm{M}}_{\mathrm{E}}(\mathrm{d}\boldsymbol{\sigma}^{\mathrm{M}}_e, \delta\mathbf{u}^{\mathrm{E}}_{eH}) &= \sum_{e=1}^{N} \left\{ {}_e\mathrm{f}^{\mathrm{E}}({}^{*}\delta\mathbf{u}^{\mathrm{E}}_{eH}) - {}_e\mathrm{b}^{\mathrm{M}}_{\mathrm{E}}((\boldsymbol{\sigma}^{\mathrm{M}}_{eH} + \triangle\boldsymbol{\sigma}^{\mathrm{M}}_{eH}), {}^{*}\delta\mathbf{u}^{\mathrm{E}}_e) \right\} \\ &= \sum_{\tilde{e}=1}^{\tilde{N}} {}_{\tilde{e}}\tilde{\mathrm{b}}^{\mathrm{E}}\left([[\mathbf{t}]]^{\tilde{e}}_H, {}^{*}\delta\mathbf{u}^{\mathrm{E}}_{\tilde{e}H}\right) \quad \forall e,\end{aligned} \tag{48}$$

$${}_e\mathrm{b}^{\mathrm{I}}_{\mathrm{I}}(\mathrm{d}\boldsymbol{\sigma}^{\mathrm{I}}_e, \delta\mathbf{u}^{\mathrm{I}}_{eH}) - {}_e\mathrm{b}^{\mathrm{M}}_{\mathrm{I}}(\mathrm{d}\boldsymbol{\sigma}^{\mathrm{M}}_e, \delta\mathbf{u}^{\mathrm{I}}_{eH}) = \sum_{\tilde{e}=1}^{\breve{N}_e} {}_{\tilde{e}}\tilde{\mathrm{b}}^{\mathrm{I}}\left([[\mathbf{t}]]^{\tilde{e}_{\mathrm{I}}}_H, \delta\mathbf{u}^{\mathrm{I}}_{\tilde{e}H}\right) = 0 \quad \forall e. \tag{49}$$

Here $\tilde{N}$ is the total number of discrete segments on the element boundaries for the entire VCFEM model and $\breve{N}_e$ corresponds to the number of segments on the matrix interface for each element e. The expressions $[[\mathbf{t}]]^{\tilde{e}/\tilde{e}_{\mathrm{I}}}_H$ correspond to traction jump operators on element boundary and interface segments, which is expressed from Eq. (8) as

$$[[\mathbf{t}]]_H^{\tilde{e}} = [[t_x]]_H^{\tilde{e}}\mathbf{i}_x + [[t_y]]_H^{\tilde{e}}\mathbf{i}_y = (\boldsymbol{\sigma}_{eH}^{\mathrm{M}} + \triangle\boldsymbol{\sigma}_{eH}^{\mathrm{M}})^{+} \cdot \mathbf{n}^{\tilde{e}+} + (\boldsymbol{\sigma}_{eH}^{\mathrm{M}} + \triangle\boldsymbol{\sigma}_{eH}^{\mathrm{M}})^{-} \cdot \mathbf{n}^{\tilde{e}-} \quad \forall\tilde{e} \quad \text{on } \Gamma_{\mathrm{me}}, \tag{50}$$

$$[[\mathbf{t}]]_H^{\tilde{e}} = [[t_x]]_H^{\tilde{e}}\mathbf{i}_x + [[t_y]]_H^{\tilde{e}}\mathbf{i}_y = (\bar{\mathbf{t}} + \bar{\triangle}\mathbf{t}) - (\boldsymbol{\sigma}_{eH}^{\mathrm{M}} + \triangle\boldsymbol{\sigma}_{eH}^{\mathrm{M}})^{+} \cdot \mathbf{n}^{\tilde{e}+} \quad \forall\tilde{e} \quad \text{on } \Gamma_{\mathrm{te}}, \tag{51}$$

$$[[\mathbf{t}]]_H^{\tilde{e}_{\mathrm{I}}} = [[t_x]]_H^{\tilde{e}_{\mathrm{I}}}\mathbf{i}_x + [[t_y]]_H^{\tilde{e}_{\mathrm{I}}}\mathbf{i}_y = (\boldsymbol{\sigma}_{eH}^{\mathrm{M}} + \triangle\boldsymbol{\sigma}_{eH}^{\mathrm{M}}) \cdot \mathbf{n}^{\tilde{e}_{\mathrm{I}}} - (\boldsymbol{\sigma}_{eH}^{\mathrm{I}} + \triangle\boldsymbol{\sigma}_{eH}^{\mathrm{I}}) \cdot \mathbf{n}^{\tilde{e}_{\mathrm{I}}} \quad \forall\tilde{e}_{\mathrm{I}} \quad \text{on } \partial\Omega_e^{\mathrm{I}}. \tag{52}$$

The modified bilinear forms ${}_{\tilde{e}}\tilde{\mathsf{b}}^{\mathrm{E/I}}$ are simple rearrangements of ${}_e\mathsf{b}^{\mathrm{E/I}}$ accounting for the traction difference between two adjacent elements of between the matrix and inclusion, and are written in terms of integration over boundary/interface segments as

$${}_{\tilde{e}}\tilde{\mathsf{b}}^{\mathrm{E}}([[\mathbf{t}]]_H^{\tilde{e}}, {}^*\delta\mathbf{u}_{\tilde{e}H}^{\mathrm{E}}) = \int_{\tilde{e}} [[\mathbf{t}]]_H^{\tilde{e}}\, {}^*\delta\mathbf{u}_{\tilde{e}H}^{\mathrm{E}}\, \mathrm{d}\Omega, \quad {}_{\tilde{e}}\tilde{\mathsf{b}}^{\mathrm{I}}([[\mathbf{t}]]_H^{\tilde{e}_{\mathrm{I}}}, \delta\mathbf{u}_{\tilde{e}H}^{\mathrm{I}}) = \int_{\tilde{e}_{\mathrm{I}}} [[\mathbf{t}]]_H^{\tilde{e}_{\mathrm{I}}}\, {}^*\delta\mathbf{u}_{\tilde{e}H}^{\mathrm{I}}\, \mathrm{d}\Omega. \tag{53}$$

In the derivation of Eqs. (48) and (49) it is assumed that the approximate form of Eq. (10) are satisfied exactly by solutions in the approximate space $\mathscr{T}_{eH}^{\mathrm{M/I}} \otimes \mathscr{V}_{eH}^{\mathrm{E/I}}$. The error arising from the terms ${}_e\mathsf{a}^{\mathrm{M/I}}$ in Eq. (7) which correspond to the variations in the element strain energy may be related to variations in ${}_e\mathsf{b}_{\mathrm{E/I}}^{\mathrm{M/I}}$ to express the error estimate for VCFEM. As shown in Appendix B, this error may be expressed as

$$\begin{aligned}
&\left|\sum_{e=1}^{N} {}_e\mathsf{a}^{\mathrm{E}}(\mathrm{d}\boldsymbol{\sigma}_e^{\mathrm{E}}, \mathrm{d}\boldsymbol{\sigma}_e^{\mathrm{E}}) + {}_e\mathsf{a}^{\mathrm{I}}(\mathrm{d}\boldsymbol{\sigma}_e^{\mathrm{E}}, \mathrm{d}\boldsymbol{\sigma}_e^{\mathrm{I}})\right| \\
&\quad \leqslant \left|\left[\sup_{\forall\, \mathrm{d}\mathbf{u}_e^{\mathrm{E/I}} \in \mathscr{V}_e^{\mathrm{E/I}}} \sum_{e=1}^{N} \{{}_e\mathsf{b}_{\mathrm{E}}^{\mathrm{M}}(\mathrm{d}\boldsymbol{\sigma}_e^{\mathrm{M}}, \mathrm{d}\mathbf{u}_e^{\mathrm{E}}) - {}_e\mathsf{b}_{\mathrm{I}}^{\mathrm{M}}(\mathrm{d}\boldsymbol{\sigma}_e^{\mathrm{M}}, \mathrm{d}\mathbf{u}_e^{\mathrm{I}}) + {}_e\mathsf{b}_{\mathrm{I}}^{\mathrm{I}}(\mathrm{d}\boldsymbol{\sigma}_e^{\mathrm{I}}, \mathrm{d}\mathbf{u}_e^{\mathrm{I}})\}\right]\right| \\
&\qquad + \left[\sum_{e=1}^{N} |\{{}_e\mathsf{b}_{\mathrm{E}}^{\mathrm{M}}({}^*\mathrm{d}\boldsymbol{\sigma}_e^{\mathrm{M}}, \triangle\mathbf{u}_{eH}^{\mathrm{E}}) - {}_e\mathsf{b}_{\mathrm{I}}^{\mathrm{M}}({}^*\mathrm{d}\boldsymbol{\sigma}_e^{\mathrm{M}}, \triangle\mathbf{u}_{eH}^{\mathrm{I}})\}| + \sum_{e=1}^{N} |\{{}_e\mathsf{b}_{\mathrm{I}}^{\mathrm{I}}({}^*\mathrm{d}\boldsymbol{\sigma}_e^{\mathrm{I}}, \triangle\mathbf{u}_{eH}^{\mathrm{I}})\}|\right].
\end{aligned} \tag{54}$$

It will be proved in subsequent sections, that the terms in the first bracket correspond to norms of errors in boundary/interface displacements and the terms in the second bracket are norms of error in stresses.

3.1. Characterization of error in traction reciprocity

The traction reciprocity conditions in Eq. (8) are satisfied in a weak sense on the interelement boundary Γ_{me}, traction boundary Γ_{te} and interface $\partial\Omega_e^{\mathrm{I}}$. The corresponding weak forms in Eq. (10) may be rewritten as

$$\begin{aligned}
&\sum_{\tilde{e}=1}^{\tilde{N}} {}_{\tilde{e}}\tilde{\mathsf{b}}^{\mathrm{E}}([[\mathbf{t}]]_H^{\tilde{e}}, \delta\mathbf{u}_{\tilde{e}H}^{\mathrm{E}}) = 0 \qquad \forall\delta\mathbf{u}_{\tilde{e}H}^{\mathrm{E}} \in \mathscr{V}_{eH}^{\mathrm{E}} \ \text{ on } \Gamma_{\mathrm{me}} \cup \Gamma_{\mathrm{te}} \\
&{}_{\tilde{e}}\tilde{\mathsf{b}}^{\mathrm{I}}([[\mathbf{t}]]_H^{\tilde{e}_{\mathrm{I}}}, \delta\mathbf{u}_{\tilde{e}H}^{\mathrm{I}}) = 0 \qquad \forall\delta\mathbf{u}_{\tilde{e}H}^{\mathrm{I}} \in \mathscr{V}_{eH}^{\mathrm{I}} \ \text{ on } \partial\Omega_e^{\mathrm{I}} \quad \text{and} \quad \forall e = 1, \ldots, N.
\end{aligned} \tag{55}$$

Minimization of traction discontinuity in Eq. (55) and consequently the satisfaction of traction continuity in a strong sense requires that

$$\sum_{\tilde{e}=1}^{\tilde{N}} {}_{\tilde{e}}\tilde{\mathsf{b}}^{\mathrm{E}}([[\mathbf{t}]]_H^{\tilde{e}}, \delta\mathbf{u}_{\tilde{e}}^{\mathrm{E}}) = 0 \quad \forall\delta\mathbf{u}_{\tilde{e}}^{\mathrm{E}} \in \mathscr{V}_e^{\mathrm{E}}, \quad {}_{\tilde{e}}\tilde{\mathsf{b}}^{\mathrm{I}}([[\mathbf{t}]]_H^{\tilde{e}_{\mathrm{I}}}, \delta\mathbf{u}_{\tilde{e}}^{\mathrm{I}}) = 0 \quad \forall\delta\mathbf{u}_{\tilde{e}}^{\mathrm{I}} \in \mathscr{V}_e^{\mathrm{I}} \quad \text{on } \partial\Omega_e^{\mathrm{I}}, \tag{56}$$

where $\delta\mathbf{u}_{\tilde{e}}$ correspond to any arbitrary displacement field. The traction discontinuity may be therefore reduced by the augmentation of displacement field approximations $\delta\mathbf{u}_{\tilde{e}H}^{\mathrm{E/I}} \in \mathscr{V}_{eH}^{\mathrm{E}}$ by a set of enrichment functions ${}^*\delta\mathbf{u}_{\tilde{e}H}^{\mathrm{E/I}} \in^{\perp} \mathscr{V}_{eH}$, such that they belong to mutually orthogonal subspaces as defined in Eq. (45). To establish the condition for optimal enrichment in displacement functions, projection vectors ${}^*[[\mathbf{t}]]_H^{\tilde{e}}$ and ${}^*[[\mathbf{t}]]_H^{\tilde{e}_{\mathrm{I}}}$ are defined as the projection of $[[\mathbf{t}]]_H^{\tilde{e}/\tilde{e}_{\mathrm{I}}}$ on $\mathscr{V}_{eH}^{\mathrm{E/I}}$ (see Fig. 2(a) and (b)) such that

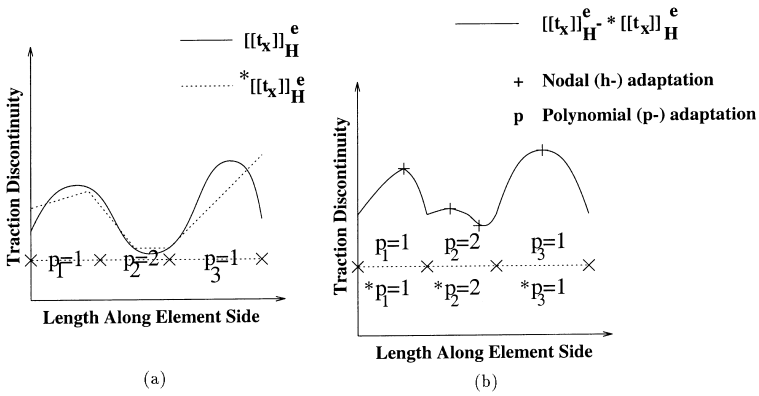

Fig. 2. Schematic diagram of: (a) traction discontinuity $[[t_x]]^{\tilde{e}}_H$ and its projection ${}^*[[t_x]]^{\tilde{e}}_H$ on an element boundary; (b) *h*- and *p*-adaptation strategy along *optimal* directions.

$$
\begin{aligned}
&{}_{\tilde{e}}\tilde{\mathrm{b}}^{\mathrm{E}}\left({}^*[[\mathbf{t}]]^{\tilde{e}}_H, \delta\mathbf{u}^{\mathrm{E}}_{\tilde{e}H}\right) = {}_{\tilde{e}}\tilde{\mathrm{b}}^{\mathrm{E}}\left([[\mathbf{t}]]^{\tilde{e}}_H, \delta\mathbf{u}^{\mathrm{E}}_{\tilde{e}H}\right),\\
&{}_{\tilde{e}}\tilde{\mathrm{b}}^{\mathrm{I}}\left({}^*[[\mathbf{t}]]^{\tilde{e}_{\mathrm{I}}}_H, \delta\mathbf{u}^{\mathrm{I}}_{\tilde{e}H}\right) = {}_{\tilde{e}}\tilde{\mathrm{b}}^{\mathrm{I}}\left([[\mathbf{t}]]^{\tilde{e}_{\mathrm{I}}}_H, \delta\mathbf{u}^{\mathrm{I}}_{\tilde{e}H}\right) \quad \forall\delta\mathbf{u}^{\mathrm{E/I}}_{\tilde{e}H} \in \mathscr{V}^{\mathrm{E/I}}_{eH}.
\end{aligned}
\tag{57}
$$

Consequently, the difference vectors $([[\mathbf{t}]]^{\tilde{e}}_H - {}^*[[\mathbf{t}]]^{\tilde{e}}_H)$ and $([[\mathbf{t}]]^{\tilde{e}_{\mathrm{I}}}_H - {}^*[[\mathbf{t}]]^{\tilde{e}_{\mathrm{I}}}_H)$ are orthogonal to the approximation space of displacements $\mathscr{V}^{\mathrm{E/I}}_{eH}$. This is also shown from linearity in the bilinear forms and Eqs. (45) and (57).

$$
\begin{aligned}
{}_{\tilde{e}}\tilde{\mathrm{b}}^{\mathrm{E/I}}\left(([[\mathbf{t}]]^{\tilde{e}/\tilde{e}_{\mathrm{I}}} - {}^*[[\mathbf{t}]]^{\tilde{e}/\tilde{e}_{\mathrm{I}}}), \delta\mathbf{u}^{\mathrm{E/I}}_{\tilde{e}H}\right) &= {}_{\tilde{e}}\tilde{\mathrm{b}}^{\mathrm{E/I}}\left([[\mathbf{t}]]^{\tilde{e}/\tilde{e}_{\mathrm{I}}}, \delta\mathbf{u}^{\mathrm{E/I}}_{\tilde{e}H}\right) - {}_{\tilde{e}}\tilde{\mathrm{b}}^{\mathrm{E/I}}\left({}^*[[\mathbf{t}]]^{\tilde{e}/\tilde{e}_{\mathrm{I}}}, \delta\mathbf{u}^{\mathrm{E/I}}_{\tilde{e}H}\right)\\
&= {}_{\tilde{e}}\tilde{\mathrm{b}}^{\mathrm{E/I}}\left([[\mathbf{t}]]^{\tilde{e}/\tilde{e}_{\mathrm{I}}}, \delta\mathbf{u}^{\mathrm{E/I}}_{\tilde{e}H}\right) - {}_{\tilde{e}}\tilde{\mathrm{b}}^{\mathrm{E/I}}\left({}^*[[\mathbf{t}]]^{\tilde{e}/\tilde{e}_{\mathrm{I}}}_H, \delta\mathbf{u}^{\mathrm{E/I}}_{\tilde{e}H}\right) = 0.
\end{aligned}
\tag{58}
$$

By comparing with Eq. (45), it may thus be concluded that $([[\mathbf{t}]]^{\tilde{e}/\tilde{e}_{\mathrm{I}}} - {}^*[[\mathbf{t}]]^{\tilde{e}/\tilde{e}_{\mathrm{I}}}) \in^{\perp} \mathscr{V}_{eH}$. An additional constraint equation is needed to characterize the the boundedness of displacement enrichments, i.e.

$$
\int_{\partial\Omega^{\mathrm{E/I}}_e} {}^*\delta\mathbf{u}^{\mathrm{E/I}}_{eH} \cdot {}^*\delta\mathbf{u}^{\mathrm{E/I}}_{eH}\,\mathrm{d}\Omega = \varepsilon^2 \quad \forall {}^*\delta\mathbf{u}_{eH} \in^{\perp} \mathscr{V}_{eH},
\tag{59}
$$

where ε is a finite number. The optimal direction for displacement adaptation ${}^*_{\mathrm{opt}}\delta\mathbf{u}^{\mathrm{E/I}}_{eH}$ is then determined from the stationary conditions of the virtual work for each element boundary or interface segment $\tilde{e}/\tilde{e}_{\mathrm{I}}$, represented by ${}_{\tilde{e}}\tilde{\mathrm{b}}^{\mathrm{E/I}}([[\mathbf{t}]]^{\tilde{e}/,\tilde{e}_{\mathrm{I}}}_H, {}^*\delta\mathbf{u}^{\mathrm{E/I}}_{\tilde{e}H})$ with given traction discontinuities $[[\mathbf{t}]]^{\tilde{e}/,\tilde{e}_{\mathrm{I}}}_H$, and subject to the constraints in Eqs. (45) and (59). An augmented functional is constructed using Lagrange multipliers as

$$
\begin{aligned}
{}_{\tilde{e}}\tilde{\mathrm{g}}^{\mathrm{E/I}}\left({}^*\delta\mathbf{u}^{\mathrm{E/I}}_{\tilde{e}H}, \lambda_1, \lambda_2\right) &= {}_{\tilde{e}}\tilde{\mathrm{b}}^{\mathrm{E/I}}\left([[\mathbf{t}]]^{\tilde{e}/,\tilde{e}_{\mathrm{I}}}_H, {}^*\delta\mathbf{u}^{\mathrm{E/I}}_{\tilde{e}H}\right) + \lambda_1 \int_{\partial\Omega^{\mathrm{E/I}}_e} \delta\mathbf{u}^{\mathrm{E/I}}_{\tilde{e}H} \cdot {}^*\delta\mathbf{u}^{\mathrm{E/I}}_{\tilde{e}H}\,\mathrm{d}\Omega\\
&\quad - \frac{\lambda_2}{2}\int_{\partial\Omega^{\mathrm{E/I}}_e} \left[{}^*\delta\mathbf{u}^{\mathrm{E/I}}_{\tilde{e}H} \cdot {}^*\delta\mathbf{u}^{\mathrm{E/I}}_{\tilde{e}H}\,\mathrm{d}\Omega - \varepsilon^2\right].
\end{aligned}
\tag{60}
$$

The optimal variation in the displacement field is proved in Appendix C to be

$$
{}^*_{\mathrm{opt}}\delta\mathbf{u}^{\mathrm{E/I}}_{eH} = \frac{([[\mathbf{t}]]^{\tilde{e}/,\tilde{e}_{\mathrm{I}}} - {}^*[[\mathbf{t}]]^{\tilde{e}/,\tilde{e}_{\mathrm{I}}})\varepsilon}{(\|[[\mathbf{t}]]^{\mathrm{E/I}}_e - {}^*[[\mathbf{t}]]^{\mathrm{E/I}}_e\|)}.
\tag{61}
$$

The first term in the error equation (54) can now be rewritten as

$$\left|\left[\sup_{\forall\, \mathrm{d}\mathbf{u}_e^{\mathrm{E/I}}} \sum_{e=1}^{N}\{{}_e\mathrm{b}_{\mathrm{E}}^{\mathrm{M}}(\mathrm{d}\boldsymbol{\sigma}_e^{\mathrm{M}}, \mathrm{d}\mathbf{u}_e^{\mathrm{E}}) - {}_e\mathrm{b}_{\mathrm{I}}^{\mathrm{M}}(\mathrm{d}\boldsymbol{\sigma}_e^{\mathrm{M}}, \mathrm{d}\mathbf{u}_e^{\mathrm{I}}) + {}_e\mathrm{b}_{\mathrm{I}}^{\mathrm{I}}(\mathrm{d}\boldsymbol{\sigma}_e^{\mathrm{I}}, \mathrm{d}\mathbf{u}_e^{\mathrm{I}})\}\right]\right|$$

$$= \left|\sum_{\tilde{e}=1}^{\tilde{N}} {}_{\tilde{e}}\tilde{\mathbf{b}}^{\mathrm{E}}([[\mathbf{t}]]_H^{\tilde{e}}, \delta\mathbf{u}_{\tilde{e}}^{\mathrm{E}}) + \sum_{\tilde{e}=1}^{\tilde{N}_e} {}_{\tilde{e}}\tilde{\mathbf{b}}^{\mathrm{I}}([[\mathbf{t}]]_H^{\tilde{e}_{\mathrm{I}}}, \delta\mathbf{u}_{\tilde{e}}^{\mathrm{I}})\right| \quad \text{from Eqs. (73) and (49)}$$

$$= \left|\sum_{\tilde{e}=1}^{\tilde{N}} [{}_{\tilde{e}}\tilde{\mathbf{b}}^{\mathrm{E}}([[\mathbf{t}]]_H^{\tilde{e}}, \delta\mathbf{u}_{\tilde{e}_H}^{\mathrm{E}}) + {}_{\tilde{e}}\tilde{\mathbf{b}}^{\mathrm{E}}([[\mathbf{t}]]_H^{\tilde{e}}, {}^*\delta\mathbf{u}_{\tilde{e}_H}^{\mathrm{E}})] + \sum_{\tilde{e}=1}^{\tilde{N}_e} [{}_{\tilde{e}}\tilde{\mathbf{b}}^{\mathrm{I}}([[\mathbf{t}]]_H^{\tilde{e}_{\mathrm{I}}}, \delta\mathbf{u}_{\tilde{e}_H}^{\mathrm{I}}) + {}_{\tilde{e}}\tilde{\mathbf{b}}^{\mathrm{I}}([[\mathbf{t}]]_H^{\tilde{e}_{\mathrm{I}}}, {}^*\delta\mathbf{u}_{\tilde{e}_H}^{\mathrm{I}})]\right|$$

$$= \left|\sum_{\tilde{e}=1}^{\tilde{N}} {}_{\tilde{e}}\tilde{\mathbf{b}}^{\mathrm{E}}([[\mathbf{t}]]_H^{\tilde{e}}, {}^*\delta\mathbf{u}_{\tilde{e}_H}^{\mathrm{E}}) + \sum_{\tilde{e}=1}^{\tilde{N}_e} [{}_{\tilde{e}}\tilde{\mathbf{b}}^{\mathrm{I}}([[\mathbf{t}]]_H^{\tilde{e}_{\mathrm{I}}}, {}^*\delta\mathbf{u}_{\tilde{e}_H}^{\mathrm{I}})\right| \quad \text{from Eq. (55)}$$

$$\leqslant \left|\sum_{\tilde{e}=1}^{\tilde{N}} \frac{\varepsilon}{(\|[[\mathbf{t}]]_e^{\mathrm{E}} - {}^*[[\mathbf{t}]]_e^{\mathrm{E}}\|)} {}_{\tilde{e}}\tilde{\mathrm{b}}^{\mathrm{E}}([[\mathbf{t}]]_H^{\tilde{e}}, [[\mathbf{t}]]^{\tilde{e}})\right| + \left|\sum_{\tilde{e}=1}^{\tilde{N}_e} \frac{\varepsilon}{(\|[[\mathbf{t}]]_e^{\mathrm{I}} - {}^*[[\mathbf{t}]]_e^{\mathrm{I}}\|)} {}_{\tilde{e}}\tilde{\mathrm{b}}^{\mathrm{I}}([[\mathbf{t}]]_H^{\tilde{e}_{\mathrm{I}}}, [[\mathbf{t}]]^{\tilde{e}_{\mathrm{I}}})\right|$$

$$\text{by using } {}^*[[\mathbf{t}]]^{\tilde{e}/,\tilde{e}_{\mathrm{I}}} \in \mathscr{V}_{eH}^{\mathrm{E/I}} \text{ in Eq. (55)} . \tag{62}$$

Thus the error in traction reciprocity $\bar{e}_{\mathrm{T}}^{\mathrm{E/I}}$ on the element boundary or the interface may be characterized as

$$\bar{e}_{\mathrm{T}}^{\mathrm{E/I}} = \frac{{}_{\tilde{e}}\tilde{\mathrm{b}}^{\mathrm{E/I}}([[\mathbf{t}]]_H^{\tilde{e}/\tilde{e}_{\mathrm{I}}}, [[\mathbf{t}]]_H^{\tilde{e}/\tilde{e}_{\mathrm{I}}})}{(n^* \int_{\partial\Omega_e^{(E/I)}} \mathrm{d}\Omega)^{1/2}}, \tag{63}$$

where n^* is a factor depending on the degrees of freedom to be adapted. For plane problems, the traction discontinuity error $\bar{e}_{\mathrm{T}}^{\mathrm{E/I}}$ may lead itself to displacement adaptations in two directions and consequently the factor $n^* = 2$. To express the error in traction reciprocity error as a fraction or percentage, the error $\bar{e}_{\mathrm{T}}^{\mathrm{E/I}}$ is normalized with respect to a stress $\bar{\sigma}_{\mathrm{I}}$ obtained as the principal value of a volume averaged stress tensor $\bar{\boldsymbol{\sigma}} = \int_\Omega \boldsymbol{\sigma}\, \mathrm{d}\Omega / \int_\Omega \mathrm{d}\Omega$. The resulting traction reciprocity error is then defined as

$$e_{\mathrm{T}}^{\mathrm{E/I}} = \frac{\bar{e}_{\mathrm{T}}^{\mathrm{E/I}}}{\bar{\sigma}_{\mathrm{I}}}. \tag{64}$$

3.2. Characterization of error in kinematic relationships

The second term in the last expression of Eq. (54) i.e. $\sum_{e=1}^{N} |\{{}_e\mathrm{b}_{\mathrm{E}}^{\mathrm{M}}({}^*\mathrm{d}\boldsymbol{\sigma}_e^{\mathrm{M}}, \triangle\mathbf{u}_{eH}^{\mathrm{E}}) - {}_e\mathrm{b}_{\mathrm{I}}^{\mathrm{M}}({}^*\mathrm{d}\boldsymbol{\sigma}_e^{\mathrm{M}}, \triangle\mathbf{u}_{eH}^{\mathrm{I}})\}| + \sum_{e=1}^{N} |\{{}_e\mathrm{b}_{\mathrm{I}}^{\mathrm{I}}({}^*\mathrm{d}\boldsymbol{\sigma}_e^{\mathrm{I}}, \triangle\mathbf{u}_{eH}^{\mathrm{I}})\}|$ corresponds to a measure of error in satisfying the kinematic relations (6) due to inadequate resolution in the representation of stresses. To evaluate this error measure, it is necessary to quantify the global change in the approximate boundary and interface displacement fields $\mathbf{u}_{eH}^{\mathrm{E/I}} \in \mathscr{V}_{eH}^{\mathrm{E/I}}$, $\forall e \in [1, \ldots, N]$ as a consequence of local stress enrichment in the element $\hat{e}$. The enriched stress in the $\hat{e}$th element may be written as

$$\boldsymbol{\sigma}_{\hat{e}}^{\mathrm{M/I}} = \boldsymbol{\sigma}_{\hat{e}H}^{\mathrm{M/I}} + {}^*\boldsymbol{\sigma}_{\hat{e}}^{\mathrm{M/I}}; (\boldsymbol{\sigma}_{\hat{e}H}, {}^*\boldsymbol{\sigma}_{\hat{e}}) \in (\mathscr{T}_{\hat{e}H}, {}^{\perp}\mathscr{T}_{\hat{e}H}). \tag{65}$$

To achieve this, the weak form (7) of the kinematic relations (4) is rewritten in terms of the enriched stresses and its variations $\delta\boldsymbol{\sigma}_e^{\mathrm{M/I}} = \delta\boldsymbol{\sigma}_{eH}^{\mathrm{M/I}} + {}^*\delta\boldsymbol{\sigma}_{eH}^{\mathrm{M/I}}$ as

$${}_e\mathrm{a}^{\mathrm{M}}((\triangle\boldsymbol{\sigma}_{eH}^{\mathrm{M}} + \mathrm{d}\boldsymbol{\sigma}_e^{\mathrm{M}}), \delta\boldsymbol{\sigma}_e^{\mathrm{M}}) = {}_e\mathrm{b}_{\mathrm{E}}^{\mathrm{M}}(\delta\boldsymbol{\sigma}_e^{\mathrm{M}}, (\triangle\mathbf{u}_{eH}^{\mathrm{E}} + \mathrm{d}\mathbf{u}_{eH}^{\mathrm{E}})) - {}_e\mathrm{b}_{\mathrm{I}}^{\mathrm{M}}(\delta\boldsymbol{\sigma}_e^{\mathrm{M}}, (\triangle\mathbf{u}_{eH}^{\mathrm{I}} + \mathrm{d}\mathbf{u}_{eH}^{\mathrm{I}})) \quad \forall\delta\boldsymbol{\sigma}_e^{\mathrm{M}} \in \mathscr{T}_e^{\mathrm{M}}, \tag{66}$$

$${}_e\mathrm{a}^{\mathrm{I}}((\triangle\boldsymbol{\sigma}_{eH}^{\mathrm{I}} + \mathrm{d}\boldsymbol{\sigma}_e^{\mathrm{I}}), \delta\boldsymbol{\sigma}_e^{\mathrm{I}}) = {}_e\mathrm{b}_{\mathrm{I}}^{\mathrm{I}}(\delta\boldsymbol{\sigma}_e^{\mathrm{I}}, (\triangle\mathbf{u}_{eH}^{\mathrm{I}} + \mathrm{d}\mathbf{u}_{eH}^{\mathrm{I}})) \quad \forall\delta\boldsymbol{\sigma}_e^{\mathrm{I}} \in \mathscr{T}_e^{\mathrm{I}}, \tag{67}$$

where $\mathrm{d}\boldsymbol{\sigma}_e^{\mathrm{M/I}}, \mathrm{d}\mathbf{u}_{eH}^{\mathrm{E/I}}$ correspond to the stress and displacement corrections in element e. In Appendix D, Eqs. (66) and (67) are further resolved to obtain the kinematic component of the error estimate. Substituting Eq. (D.2) in Appendix D to the second term of the last expression in Eq. (54) yields

$$\left[\sum_{e=1}^{N}|\{{}_e\mathsf{b}_{\mathrm{E}}^{\mathrm{M}}({}^*\mathrm{d}\boldsymbol{\sigma}_e^{\mathrm{M}},\triangle\mathbf{u}_{eH}^{\mathrm{E}})-{}_e\mathsf{b}_{\mathrm{I}}^{\mathrm{M}}({}^*\mathrm{d}\boldsymbol{\sigma}_e^{\mathrm{M}},\triangle\mathbf{u}_{eH}^{\mathrm{I}})\}|+\sum_{e=1}^{N}|\{{}_e\mathsf{b}_{\mathrm{I}}^{\mathrm{I}}({}^*\mathrm{d}\boldsymbol{\sigma}_e^{\mathrm{I}},\triangle\mathbf{u}_{eH}^{\mathrm{I}})\}|\right]$$
$$=\sum_{E=1}^{N}|\{{}_e\mathsf{a}^{\mathrm{M}}(\mathrm{d}\boldsymbol{\sigma}_e^{\mathrm{M}},\mathrm{d}\boldsymbol{\sigma}_e^{\mathrm{M}})-{}_e\mathsf{b}_{\mathrm{E}}^{\mathrm{M}}(\mathrm{d}\boldsymbol{\sigma}_e^{\mathrm{M}},\mathrm{d}\mathbf{u}_{eH}^{\mathrm{E}})-{}_e\mathsf{b}_{\mathrm{I}}^{\mathrm{M}}(\mathrm{d}\boldsymbol{\sigma}_e^{\mathrm{M}},\mathrm{d}\mathbf{u}_{eH}^{\mathrm{I}})\}|$$
$$+\sum_{E=1}^{N}|\{{}_e\mathsf{a}^{\mathrm{I}}(\mathrm{d}\boldsymbol{\sigma}_e^{\mathrm{I}},\mathrm{d}\boldsymbol{\sigma}_e^{\mathrm{I}})-{}_e\mathsf{b}_{\mathrm{I}}^{\mathrm{I}}(\mathrm{d}\boldsymbol{\sigma}_e^{\mathrm{I}},\mathrm{d}\mathbf{u}_{eH}^{\mathrm{I}})\}|. \tag{68}$$

The evaluation of this error from stress enrichments is detailed in Section 3.5.

3.3. The adaptation process

Consistent with the error measures discussed in the previous section, two stages of adaptation are executed for enhancing the rate of convergence. Their implementations are discussed in next.

3.4. Displacement adaptation for improved traction reciprocity

The error in traction reciprocity in Eq. (64) and the associated direction of optimal displacement enrichment ${}^*_{\mathrm{opt}}\delta\mathbf{u}_{eH}$ in Eq. (61) are used to selectively enrich displacement degrees of freedom on the element boundaries and interfaces. Adaptation entails that the displacement field be interpolated along the optimal displacement direction, proved to be along $([[\mathbf{t}]]_H^{\tilde{e}/\tilde{e}_{\mathrm{I}}}-{}^*[[\mathbf{t}]]_{eH}^{\tilde{e}/\tilde{e}_{\mathrm{I}}})$ in Section 3.1. This is achieved in two ways, viz. (a) by adding nodal degrees of freedom along the element boundaries and interfaces or h-adaptation, and (b) by enriching the order of interpolation functions between nodes on the element boundaries/interfaces or p-adaptation. It results in altered representations of the interpolation matrices $[\mathbf{L}^{\mathrm{E}}]$ and $[\mathbf{L}^{\mathrm{I}}]$ in Eq. (18). The displacement adaptation process is accomplished in the following steps.

(1) The traction discontinuity vectors $[[\mathbf{t}]]_H^{\tilde{e}/\tilde{e}_{\mathrm{I}}}=[[t_x]]_H^{\tilde{e}/\tilde{e}_{\mathrm{I}}}\mathbf{i}_x+[[t_y]]_H^{\tilde{e}/\tilde{e}_{\mathrm{I}}}\mathbf{i}_y$ on the element boundaries ($\tilde{e}=1..\tilde{N}$) and interfaces ($\tilde{e}_{\mathrm{I}}=1\cdots\breve{N}_e\ \forall e$) are first generated from the stress fields $\boldsymbol{\sigma}_{eH}^{\mathrm{M/I}}$.

(2) Next, the components of the projected traction vector ${}^*[[t_x]]_H^{\tilde{e}/\tilde{e}_{\mathrm{I}}}$ and ${}^*[[t_y]]_H^{\tilde{e}/\tilde{e}_{\mathrm{I}}}$ are evaluated from the displacement fields on $\tilde{e}$ and $\tilde{e}_{\mathrm{I}}$ as depicted in Fig. 2(a). This displacement field on a given boundary/interface segment may consist of previously adapted additional nodal degrees of freedom (h-adapted) or enriched polynomials (p-adapted). Concurrently, the node-polynomial or hp data structure for a given side along each of the x and y directions are recorded. These are marked on the abscissa of the graph in Fig. 2 (a) with $\times$ for node addition or h-adaptation and with $\mathbf{p}$ for polynomial enrichment or p-adaptation.

To obtain the projection of the traction discontinuity along the displacement vectors according to Eq. (57), the displacement components ${}_xu_{eH}^{\mathrm{E/I}}$ and ${}_yu_{eH}^{\mathrm{E/I}}$ on a segment j are expressed in terms of a set of orthonormal basis vectors $({}_x\hat{u}_i^j,{}_y\hat{u}_i^j)$ as

$${}_xu_{eH}^{\mathrm{E/I}}=\sum_{i=1}^{p_j+1}{}^x\alpha_{ij}^h\ {}_x\hat{u}_i^j\quad\text{and}\quad{}_yu_{eH}^{\mathrm{E/I}}=\sum_{i=1}^{p_j+1}{}^y\alpha_{ij}^h\ {}_y\hat{u}_i^j. \tag{69}$$

The coefficients α_{ij}^h correspond to the components of the displacement along the respective basis vector. The number of basis vectors are determined by the order of the polynomials p_j used to interpolate displacements. Starting from the shape functions in $[\mathbf{L}^{\mathrm{E/I}}]$ in terms of the line coordinates s, a Gram–Schmidt orthogonalization procedure yields the orthonormal basis according to

$${}_{\tilde{e}}\tilde{\mathsf{b}}^{\mathrm{E/I}}({}_x\hat{u}_i^j,{}_x\delta\hat{u}_k^j)=\delta_{ik}\quad\text{and}\quad{}_{\tilde{e}}\tilde{\mathsf{b}}^{\mathrm{E/I}}({}_y\hat{u}_i^j,{}_y\delta\hat{u}_k^j)=\delta_{ik}\qquad\forall(i,k)\in(1,p_j+1). \tag{70}$$

Subsequently, the projected traction discontinuity vectors are calculated as

$${}^*[[t_x]]_H^{\tilde{e}/\tilde{e}_{\mathrm{I}}}=\sum_{j=1}^{np}\sum_{i=1}^{p_j+1}{}_{\tilde{e}}\tilde{\mathsf{b}}^{\mathrm{E/I}}([[t_x]]_H^{\tilde{e}/\tilde{e}_{\mathrm{I}}},{}_x\hat{u}_i^j)_x\hat{u}_i^j,\qquad{}^*[[t_y]]_H^{\tilde{e}/\tilde{e}_{\mathrm{I}}}=\sum_{j=1}^{np}\sum_{i=1}^{p_j+1}{}_{\tilde{e}}\tilde{\mathsf{b}}^{\mathrm{E/I}}([[t_y]]_H^{\tilde{e}/\tilde{e}_{\mathrm{I}}},{}_y\hat{u}_i^j)_y\hat{u}_i^j. \tag{71}$$

For previously unadapted boundary segments the value of np in Eq. (71) is 1, but for segments that have already undergone h-adaptation, the value of np corresponds to the total number of divisions between nodes as shown in Fig. 2(a). It should be noted that a single vector with components ${}^{*}[[t_{x/y}]]_H^{\tilde{e}/\tilde{e}_{\mathrm{I}}}$ are evaluated for a boundary/interface element. The optimal direction for displacement adaptation is obtained from Eq. (61) as

$$ {}^{\mathrm{adapt}}\mathbf{u}_H^{\tilde{e}/\tilde{e}_{\mathrm{I}}} = \frac{([[t_x]]_H^{\tilde{e}/\tilde{e}_{\mathrm{I}}} - {}^{*}[[t_x]]_H^{\tilde{e}/\tilde{e}_{\mathrm{I}}})\mathbf{i}_x + ([[t_y]]_H^{\tilde{e}/\tilde{e}_{\mathrm{I}}} - {}^{*}[[t_y]]_H^{\tilde{e}/\tilde{e}_{\mathrm{I}}})\mathbf{i}_y}{|[[\mathbf{t}]]_H^{\tilde{e}/\tilde{e}_{\mathrm{I}}} - {}^{*}[[\mathbf{t}]]_H^{\tilde{e}/\tilde{e}_{\mathrm{I}}}|}. \tag{72} $$

(3) Adaptation of hp data structure to better achieve the optimal displacement direction on the element boundary and interface segments is achieved by adding nodal degrees of freedom (h-adaptation) or by enriching interpolation functions (p-adaptation). In this work, either h refinement or p enrichment is executed in each cycle of a posteriori adaptation, but not simultaneously.

(a) For the cycle of h-adaptation, nodal displacement degrees of freedom are added along either the x- or the y-direction. This is based on the inflection points in $([[t_x]]_H^{\tilde{e}/\tilde{e}_{\mathrm{I}}} - {}^{*}[[t_x]]_H^{\tilde{e}/\tilde{e}_{\mathrm{I}}})$ or $([[t_y]]_H^{\tilde{e}/\tilde{e}_{\mathrm{I}}} - {}^{*}[[t_y]]_H^{\tilde{e}/\tilde{e}_{\mathrm{I}}})$ as shown with + symbols in Fig. 2(b).

(b) For the cycle of p-adaptation, enriched shape functions in the interpolation matrices $[\mathbf{L}^{\mathrm{E/I}}]$ are created with higher order polynomials. For each segment j (may be previously h-adapted), the new polynomial order p_j^* is calculated as the sum of the old order p_j and the total number of the inflection points on the $[[t_{x/y}]]_H^{\tilde{e}/\tilde{e}_{\mathrm{I}}} - {}^{*}[[t_{x/y}]]_H^{\tilde{e}/\tilde{e}_{\mathrm{I}}}$ graph, as shown in Fig. 2 (b).For problems in elasticity, h-refinement is done in the first cycle of a posteriori adaptation on all required segments. The second cycle involves p-enrichment on the h-adapted sides. A cut-off value in the traction reciprocity error in Eq. (64) is a priori chosen to be $e_{\mathrm{T}}^{\mathrm{cut-off}} = \max[0.01, e_{\mathrm{T}}^{\mathrm{E/I}}/10]$.

(4) While the above procedure creates separate adaptations in each of the x- and y-directions, it may also be possible in some cases to adapt the displacement field along a single direction x', which is at an angle θ to the x-direction. For this, the traction discontinuity operators in the x' and y' directions are first obtained as:

$$ [[t_{x'}]]_H^{\tilde{e}/\tilde{e}_{\mathrm{I}}} = [[t_x]]_H^{\tilde{e}/\tilde{e}_{\mathrm{I}}} \cos\theta + [[t_y]]_H^{\tilde{e}/\tilde{e}_{\mathrm{I}}} \sin\theta, \tag{73} $$

$$ [[t_{y'}]]_H^{\tilde{e}/\tilde{e}_{\mathrm{I}}} = [[t_y]]_H^{\tilde{e}/\tilde{e}_{\mathrm{I}}} \cos\theta - [[t_x]]_H^{\tilde{e}/\tilde{e}_{\mathrm{I}}} \sin\theta. \tag{74} $$

Any direction, for which the error associated with $[[t_{y'}]]_H^{\tilde{e}/\tilde{e}_{\mathrm{I}}}$ is significantly less than that associated with $[[t_{x'}]]_H^{\tilde{e}/\tilde{e}_{\mathrm{I}}}$ is ideal for this class of adaptation. The direction can be obtained as the solution to an optimization problem stated as

$$ \min \left[\frac{e_{\mathrm{T}}^{\mathrm{E/I}}(y')}{e_{\mathrm{T}}^{\mathrm{E/I}}(x')}\right]; \quad \text{s.t.} \left[\frac{e_{\mathrm{T}}^{\mathrm{E/I}}(y')}{e_{\mathrm{T}}^{\mathrm{E/I}}(x')}\right] \leqslant \epsilon_{x'y'} \quad \text{for} \quad \theta \in (0°, 180°), \tag{75} $$

where $\epsilon_{x'y'}$ is a predetermined small number. The optimal direction, if any, is calculated only for the first cycle of i.e. h-adaptation. Subsequent cycles of p-adaptation are performed along this direction.

3.5. Stress adaptation for improved kinematics

Adaptation of stress functions is performed only after boundary and interface displacement adaptation, follows the error measures and procedures introduced in Section 3.2. For enriching the stress components in ${}^{\mathrm{enr}}\mathscr{T}_{eH}^{\mathrm{M/I}} \to (\mathscr{T}_{eH} \oplus^{\perp} \mathscr{T}_{eH})$, the basis functions are augmented with higher order terms $[{}^{\mathrm{enr}}\mathbf{P}_{eH}^{\mathrm{M/I}}]$ yielding a modified form of Eq. (19) as

$$ {}^{\mathrm{enr}}\mathscr{T}_{eH}^{\mathrm{M/I}} = \mathrm{span}\left\{\mathbf{P}_{eH}^{\mathrm{M/I}} + {}^{\mathrm{enr}}\mathbf{P}_{eH}^{\mathrm{M/I}}\right\} \quad \forall e. \tag{76} $$

As a consequence of local stress enrichment, the corresponding boundary and interface displacement corrections for the entire finite element domain are obtained by solving the enriched form of the global traction reciprocity Eq. (27), given as

$$\sum_{e=1}^{N}[{}^{\mathrm{enr}}\mathbf{K}_e]\{\mathrm{d}\mathbf{q}_{eH}\} = -\left\{\sum_{e=1}^{N}\begin{bmatrix}\int_{\partial\Omega_e^{\mathrm{E}}}[\mathbf{L}^{\mathrm{E}}]^{\mathrm{T}}[\mathbf{n}^{\mathrm{E}}]^{\mathrm{T}}[{}^{\mathrm{enr}}\mathbf{P}^{\mathrm{M}}]\,\mathrm{d}\Omega & \mathbf{0}\\ \int_{\partial\Omega_e^{\mathrm{I}}}[\mathbf{L}^{\mathrm{I}}]^{\mathrm{T}}[\mathbf{n}^{\mathrm{I}}]^{\mathrm{T}}[{}^{\mathrm{enr}}\mathbf{P}^{\mathrm{M}}]\,\mathrm{d}\Omega & \int_{\partial\Omega_e^{\mathrm{I}}}[\mathbf{L}^{\mathrm{c}}]^{\mathrm{T}}[\mathbf{n}^{\mathrm{I}}]^{\mathrm{T}}[{}^{\mathrm{enr}}\mathbf{P}^{\mathrm{I}}]\,\mathrm{d}\Omega\end{bmatrix}\begin{Bmatrix}\boldsymbol{\beta}^m + \triangle\boldsymbol{\beta}_{eH}^{\mathrm{M}}\\ \boldsymbol{\beta}^{\mathrm{c}} + \triangle\boldsymbol{\beta}_{eH}^{\mathrm{I}}\end{Bmatrix}\right\}, \tag{77}$$

where the enriched element stiffness matrix $[{}^{\mathrm{enr}}\mathbf{K}]$ is obtained from enriched matrices $[{}^{\mathrm{enr}}\mathbf{G}]$ and $[{}^{\mathrm{enr}}\mathbf{H}]$. This procedure is similar to adaptivity for pollution errors as discussed in [23–25]. The local problem is then solved with the new displacements to obtain the enriched stress parameters ${}^{\mathrm{enr}}\,\mathrm{d}\boldsymbol{\beta}_e^{\mathrm{M/I}}$ from the enriched form of Eq. (23)

$$\begin{bmatrix}{}^{\mathrm{enr}}\mathbf{H}_{\mathrm{M}} & \mathbf{0}\\ \mathbf{0} & {}^{\mathrm{enr}}\mathbf{H}_{\mathrm{I}}\end{bmatrix}\begin{Bmatrix}{}^{\mathrm{enr}}\mathrm{d}\beta_{eH}^{\mathrm{M}}\\ {}^{\mathrm{enr}}\mathrm{d}\beta_{eH}^{\mathrm{I}}\end{Bmatrix} = \begin{bmatrix}{}^{\mathrm{enr}}\mathbf{G}_{\mathrm{E}} & -{}^{\mathrm{enr}}\,\mathbf{G}_{\mathrm{MI}}\\ \mathbf{0} & {}^{\mathrm{enr}}\mathbf{G}_{\mathrm{II}}\end{bmatrix}\begin{Bmatrix}\mathrm{d}\mathbf{q}_{eH}^{\mathrm{E}}\\ \mathrm{d}\mathbf{q}_{eH}^{\mathrm{I}}\end{Bmatrix}. \tag{78}$$

Substituting Eqs. (30)–(32) in Eq. (68), the expression of error indicator in kinematic relations is expressed as

$$\begin{aligned}(\mathrm{SE})_{\Omega}^2\sum_{e=1}^{N}(e_{\mathrm{SE}}|_u)^2 = \sum_{e=1}^{N}|\{\,\mathrm{d}\boldsymbol{\beta}_e^{\mathrm{M}}\,\}^{\mathrm{T}}[{}^{\mathrm{enr}}\mathbf{H}_{\mathrm{M}}]\{\,\mathrm{d}\boldsymbol{\beta}_e^{\mathrm{M}}\,\} - \{\,\mathrm{d}\boldsymbol{\beta}_e^{\mathrm{M}}\,\}^{\mathrm{T}}[{}^{\mathrm{enr}}\mathbf{G}_{\mathrm{E}}]_{\mathrm{E}}\{\,\mathrm{d}\mathbf{q}_e^{\mathrm{E}}\,\}\\ + \{\,\mathrm{d}\boldsymbol{\beta}_e^{\mathrm{M}}\,\}^{\mathrm{T}}[{}^{\mathrm{enr}}\mathbf{G}_{\mathrm{MI}}]\{\,\mathrm{d}\mathbf{q}_e^{\mathrm{I}}\,\}| + |\{\,\mathrm{d}\boldsymbol{\beta}_e^{\mathrm{I}}\,\}^{\mathrm{T}}[{}^{\mathrm{enr}}\mathbf{H}_{\mathrm{I}}]\{\,\mathrm{d}\boldsymbol{\beta}_e^{\mathrm{I}}\,\} - \{\,\mathrm{d}\boldsymbol{\beta}_e^{\mathrm{I}}\,\}^{\mathrm{T}}[{}^{\mathrm{enr}}\mathbf{G}_{\mathrm{II}}]\{\,\mathrm{d}\mathbf{u}^{\mathrm{c}}\,\}|,\end{aligned} \tag{79}$$

where SE_{Ω} is the strain energy of the entire finite element domain and $e_{\mathrm{SE}}|_u$ is an element level error indicator of strain energy that is associated with purely stress enrichment corresponding to a given displacement field.

Stress adaptation is based on the requirement that element level error $e_{\mathrm{SE}}|_u$ be less than a preset tolerance, which in this work is chosen to be

$$\frac{\sqrt{\sum_{e=1}^{N}(e_{\mathrm{SE}}|_u)^2}}{N} < 10\%.$$

The reciprocal bases $\Phi_{\mathrm{rec}}^{\mathrm{M}}$ used in VCFEM, provides increasing resolution of the strees field with increasing exponents of the $1/f$ terms at vanishing distances from interface. Consequently, the stress function has a h-type adaptivity built into it. Therefore the failure to meet the error criterion is compensated by *p-adaptation*, implying an increase in the order of the polynomial contributing to the stress interpolation matrices $[\mathbf{P}_{eH}^{\mathrm{M/I}}]$. The order is increased by one in each adaptation cycle in each of the matrix or inclusion phases, as required. Eqs. (77) and (78) are then solved for improved displacements and stress parameters. The maximum order ${}^{\mathrm{enr}}p$ allowed in the polynomial enrichment in this adaptation process is 10.

From problems with plasticity, initial adaptations are conducted for the purely elastic problems as discussed. With the incremental progress of the analysis, the solution is monitored for traction reciprocity error. Subsequent adaptations are performed only through p-enrichment for $e_{\mathrm{T}}^{\mathrm{cut-off}} > 0.05$ on the boundaries or interfaces. In addition, stress polynomial enrichments are also made by ${}^{\mathrm{enr}}p$-adaptation for $e_{\mathrm{SE}}|_u > 10\%$.

4. Numerical examples

Various numerical examples are solved to understand the strength and effectiveness of the adaptive Voronoi cell finite element model in analyzing heterogeneous microstructures. The heterogeneities are in the form of voids or inclusions of different shapes and distributions. The microstructures are chosen to represent various morphological effects and interactions between them. The inclusion material always considered to be elastic while the matrix material may be elastic or elastic–plastic. Both inplane and out of plane (generalized plane strain) displacement loadings are considered for the two dimensional microstructures. The sequence of adaptations executed automatically by the program are: (i) h-adaptation on the element boundaries and interfaces; (ii) p-adaptation on the already h-adapted element boundaries and

interfaces; and (iii) $^{\text{enr}}p$-adaptation for enriching the matrix and inclusion stress fields. For elastic–plastic problems, this sequence is repeated at discrete increments of progressive deformation. It is important to note that, the L–B–B stability conditions necessitate enrichment of stress functions as a consequence of additional degrees of freedom due to h–p adaptation on the boundaries and interfaces. Thus, stress functions are augmented even without requirements from the strain energy error criterion.

4.1. Elastic problems

The elastic problems considered in this section are classified according to different morphological aspects.

4.1.1. Microstructures with different distributions of circular heterogeneities

Six composite and porous microstructures with different distribution patterns are analyzed in this example as shown in Fig. 3. They consist of four circular inclusions or voids. Relevant microstructural di-

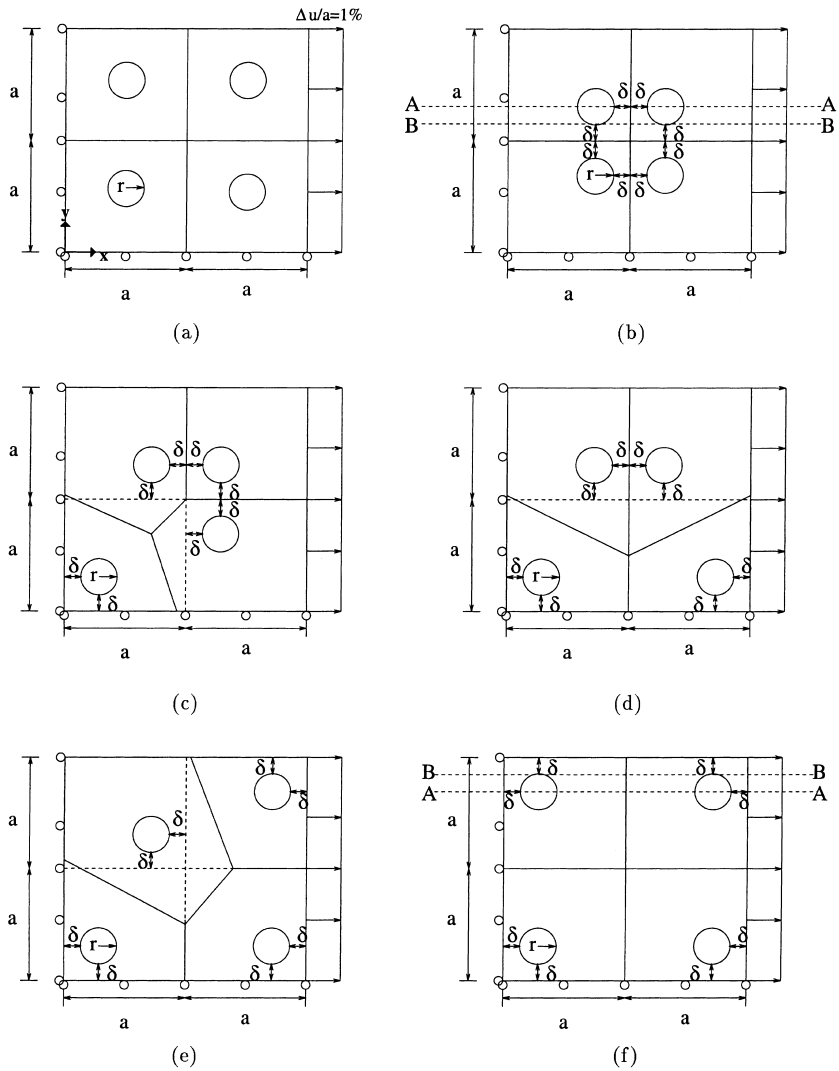

Fig. 3. (a–f) Different microstructural patterns and VCFEM meshes to illustrate the morphological and interaction effects on the solution; dimensions are given as $\delta/r = 0.25, r/a = 0.2$.

mensions and the unidirectional loading conditions are depicted in the figures. The dimensional ratios are chosen to be $r/a = 0.2$ and $\delta/r = 0.25$, where r is the radius of the circle. The Voronoi cell element boundaries are indicated with solid lines, and the dotted lines are used as location references. The six configurations, chosen to delineate the effect of proximity of neighbors and the influence of boundaries on solutions, are classified as follows.

1. Pattern 1 in Fig. 3(a) contains the heterogeneities in a square-edge arrangement at equal distances from each other and from the boundaries. The effects of the interaction between the heterogeneities and the influence of the boundaries are expected to be similar in this case.
2. Pattern 2 in Fig. 3(b) is generated from pattern 1 by uniformly moving the heterogeneities close to one another, but away from the boundaries. The effect of the interaction between the heterogeneities is much stronger than the boundary influence in this case.
3. Pattern 3 in Fig. 3(c) is generated through altering pattern 2 by moving the lower left heterogeneity closer to the boundary and away from the others.
4. Pattern 4 in Fig. 3(d) is generated through altering pattern 2 by moving the lower two heterogeneities closer to the boundary and away from the top two.
5. Pattern 5 in Fig. 3(e) is generated from pattern 2 by moving all but the top left heterogeneity close to the boundary.
6. Pattern 6 in Fig. 3(f) is generated from pattern 1 by uniformly moving the heterogeneities close to the boundaries but away from one another. The boundary influence is stronger than the interaction between heterogeneities in this case.

As shown in Fig. 3, the initial mesh consists of four Voronoi cell elements that are generated by a surface based tessellation method outlined in [7]. The pre-adaptation stress and displacement fields are as follows:

(a) *Matrix stresses*: The matrices in Eq. (16) are constructed with a 12 term, 4-th order polynomial stress function ($p + q = 2, \ldots, 4$) for $[\mathbf{P}^{\mathrm{M}}_{\mathrm{poly}}]$ with an associated 36 term reciprocal field ($i = 1, \ldots, 3$ $\forall p + q = 2, \ldots, 4$) created for $[\mathbf{P}_{\mathrm{rec}}]$.

(b) *Inclusion stresses*: The $[\mathbf{P}^{\mathrm{I}}_{\mathrm{poly}}]$ matrix in Eq. (17) is constructed using a 25 term, 6-th order polynomial stress function ($p + q = 2, \ldots, 6$).

(c) *Element boundary displacements*: The $[\mathbf{L}^{\mathrm{E}}]$ matrix in Eq. (18) are constructed with linear shape functions interpolating between adjacent nodes.

(d) *Interface displacements*: The $[\mathbf{L}^{\mathrm{I}}]$ matrix in Eq. (18) are constructed using curved elements with quadratic shape functions.

Composite material (Figs. 4–10): The matrix material in the composite is assumed to be Al-3.5% Cu with Young's Modulus $E = 69$ GPa and Poisson's ratio $\nu = 0.32$, while the inclusion material is SiC with Young's Modulus $E = 450$ GPa and Poisson's ratio $\nu = 0.17$. The convergence of the VCFEM solutions is shown with the log–log plots of the traction reciprocity error and strain energy error as functions of the inverse of total degrees of freedom in the models in Fig. 4. The degrees of freedom (DOF) correspond to the sum to the total number of nodal degrees of freedom and the number of β parameters, i.e. DOF$= 2 * N_{\mathrm{nodes}} + N_{\beta}$. The average traction reciprocity error for the entire model is calculated from Eq. (64) as

$$\text{Average Traction Reciprocity Error (ATRE)} = \frac{\sum_{\tilde{e}_{\mathrm{E}}=1}^{\tilde{N}_{\mathrm{E}}} e_{\mathrm{T}}^{\mathrm{E}} + \sum_{\tilde{e}_{\mathrm{I}}=1}^{\tilde{N}_{\mathrm{I}}} e_{\mathrm{T}}^{\mathrm{I}}}{\tilde{N}_{\mathrm{E}} + \tilde{N}_{\mathrm{I}}}, \tag{80}$$

where $\tilde{N}_{\mathrm{E}}$ and $\tilde{N}_{\mathrm{I}}$ correspond to the total number of segments on the element boundary and interface respectively. Similarly the average error in the strain energy is calculated from Eq. (79) as

$$\text{Average Strain Energy Error (ASEE)} = \frac{\sqrt{\sum_{e=1}^{N} \left(e_{\mathrm{SE}}|_{u}\right)^2}}{N}. \tag{81}$$

Table 1 gives the numerical details of error reduction with added degrees of freedom due to each mode of adaptation. In the graphs of Fig. 4, the discrete points for each pattern correspond to the different stages of adaptation. In Fig. 4(a) the first drop in traction reciprocity error is for boundary/interface h-adaptation, the second for boundary/interface p-adaptation and the final is for two cycles of stress function ($^{\mathrm{enr}}p$)

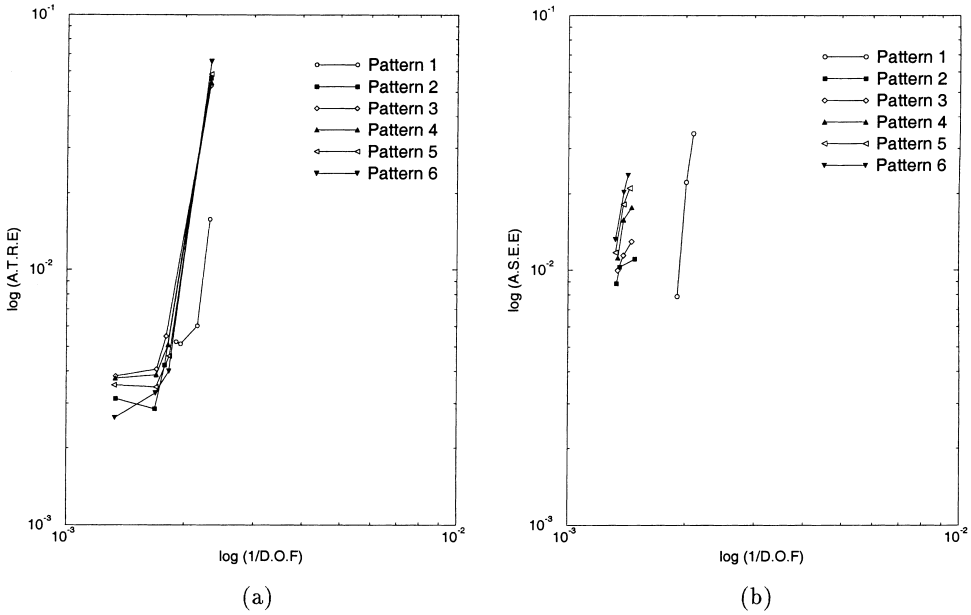

Fig. 4. Solution convergence rate in the six composite microstructural patterns with h–p–$^{\mathrm{enr}}p$-adaptations: (a) average traction reciprocity error (ATRE) and (b) average strain energy error (ASEE), as functions of inverse of the total degrees of freedom.

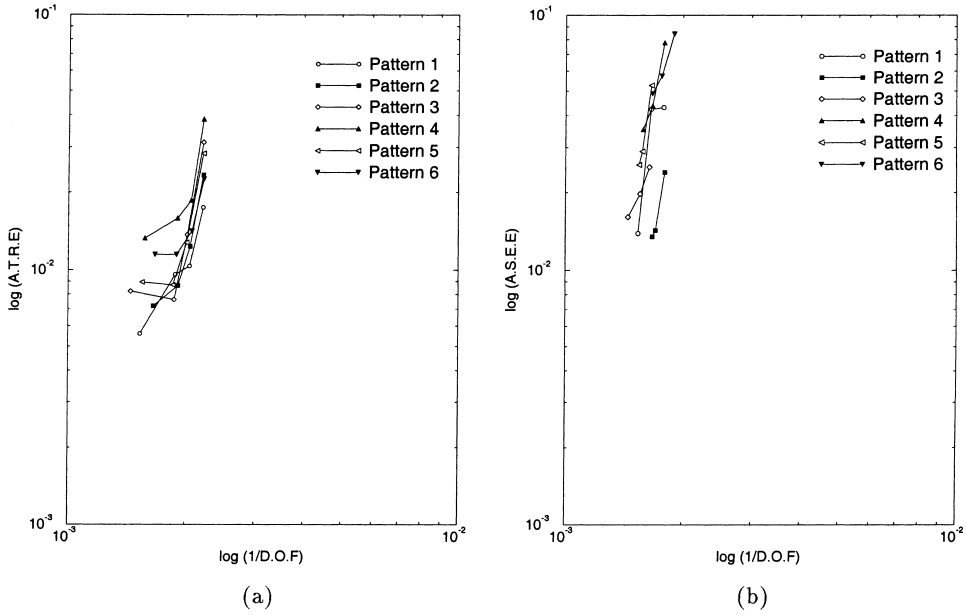

Fig. 5. Solution convergence rate in the six porous microstructural patterns with h–p–$^{\mathrm{enr}}p$-adaptations: (a) average traction reciprocity error (ATRE) and (b) average strain energy error (ASEE), as functions of inverse of the total degrees of freedom.

enrichment. For the microstructure with the maximum change in error, a 99% change in traction reciprocity error is obtained with a 38% increase in DOF. The traction reciprocity error reduces rather drastically in the first adaptation cycle, i.e. with h-adaptation as shown by the large drops in the graphs. Very little is gained in the traction reciprocity through additional stress enrichment in $^{\mathrm{enr}}p$-adaptation. On the other hand, considerable reduction in the strain energy error is achieved by the 2 cycles of stress function

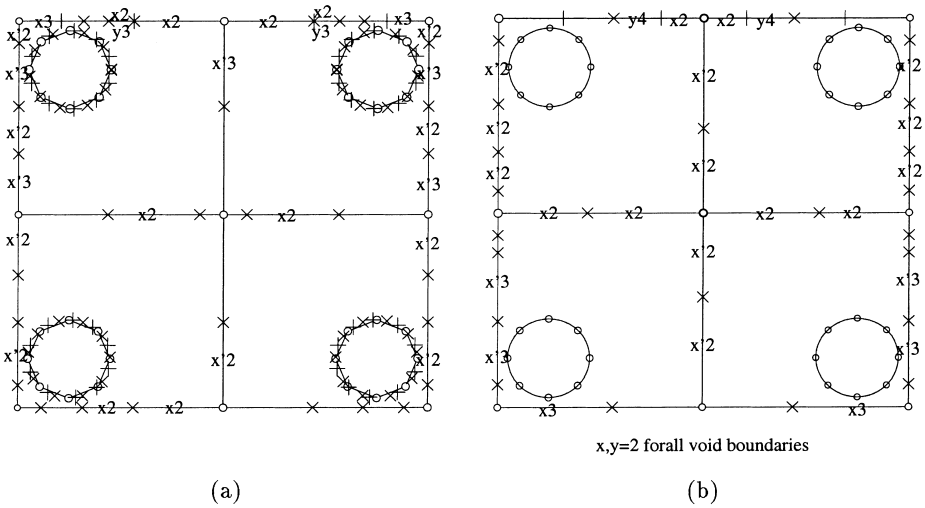

Fig. 6. Final h–p-adapted mesh for pattern 6 showing locations of the initial (marked with a $\circ$) and added nodes with $x-$ (marked with a $\times$) and $y-$ (marked with a $+$) DOF: (a) composite microstructure and (b) porous microstructure. *Note*: Only polynomial $-p$ orders greater than 1 are marked in the figure.

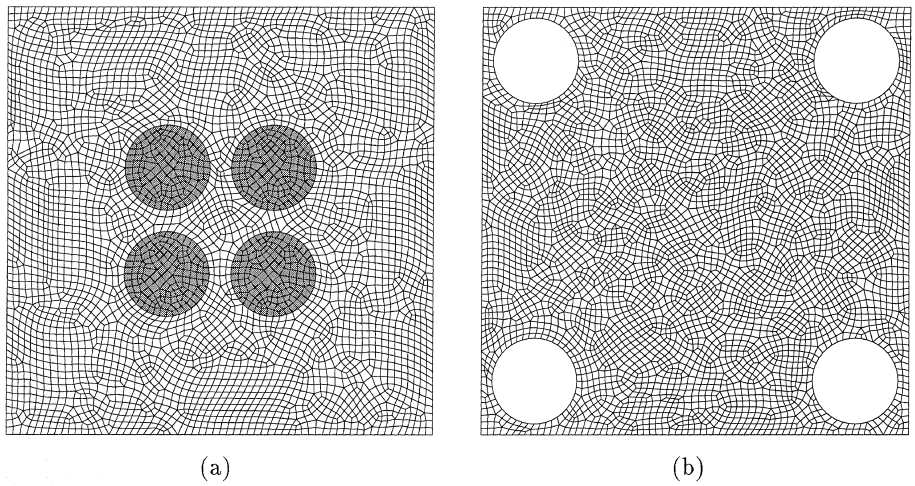

Fig. 7. ANSYS mesh with QUAD4 elements for: (a) composite microstructure of pattern 2 and (b) porous microstructure of pattern 6.

augmentation by ${}^{\mathrm{enr}}p$-adaptation, as shown in Fig. 4(b). For example in pattern 2, the maximum error in the strain energy is found to drop from 3.2% before (${}^{\mathrm{enr}}p$) enrichment to 2.1% by enriching the stress function in each element by four polynomial orders from the initial order to $p+q=2,\ldots,8$. The rates of convergence are indicated by the slopes of the plots, and are very similar for all but the pattern 1. In pattern 1, the initial error is less and it also converges at a faster rate during the p-adaptation. The results validate the effectiveness of this adaptation scheme for a wide variety of morphologies.

Pertinent observations during the adaptation process with different patterns are delineated below.

(i) For pattern 1, the h–p displacement adaptation occurs predominantly at the element boundaries in comparison with the matrix–inclusion interfaces. The traction reciprocity error on the latter are found to be considerably lower. The element boundary refinement by h-adaptation is able to reduce the traction reciprocity error below the preset tolerance for all but the top edges. With subsequent p-adaptations in the y direction the zero traction conditions on these boundaries are better satisfied.

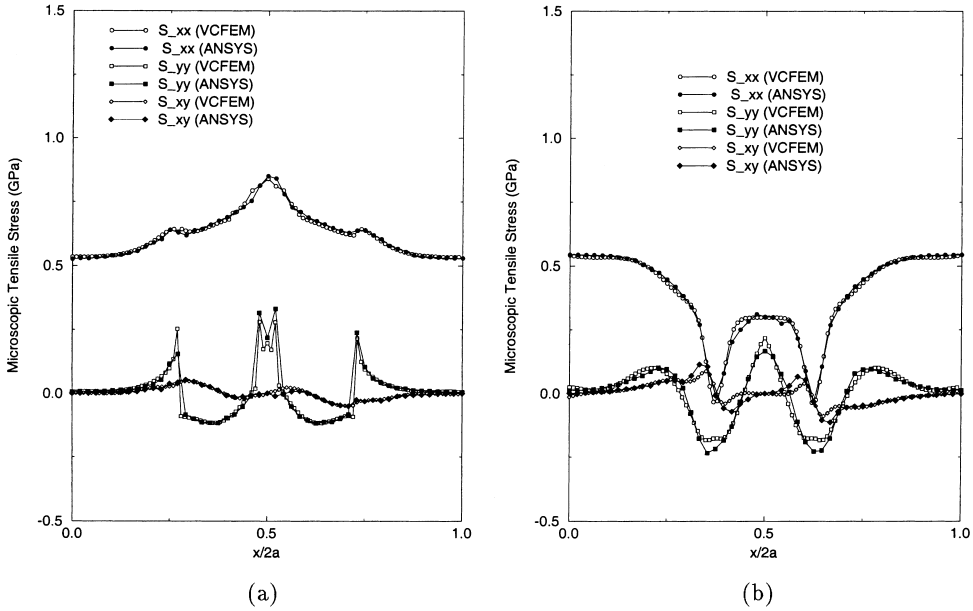

Fig. 8. Comparison of microscopic stress distribution for the composite microstructure of pattern 2 along: (a) Section A in Fig. 3(b) at $y/2a = 0.625$ and (b) Section B in Fig. 3(b) at $y/2a = 0.524$.

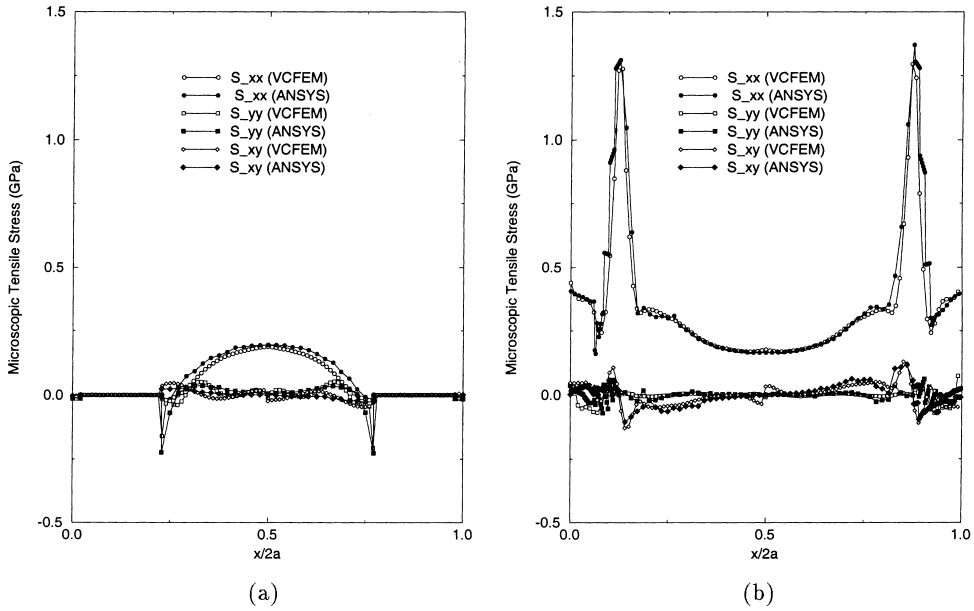

Fig. 9. Comparison of microscopic stress distribution for the porous microstructure of pattern 6 along: (a) Section A in Fig. 3(b) at $y/2a = 0.88$ and (b) Section B in Fig. 3(b) at $y/2a = 0.975$.

(ii) Pattern 2 requires *h–p* displacement adaptations on both the element boundaries and interfaces. In particular, for those segments on the interelement boundaries and interfaces that are in close proximity with each other, a large number of additional nodes are needed. Subsequent *p*-adaptation is also needed on these boundary and interface segments.

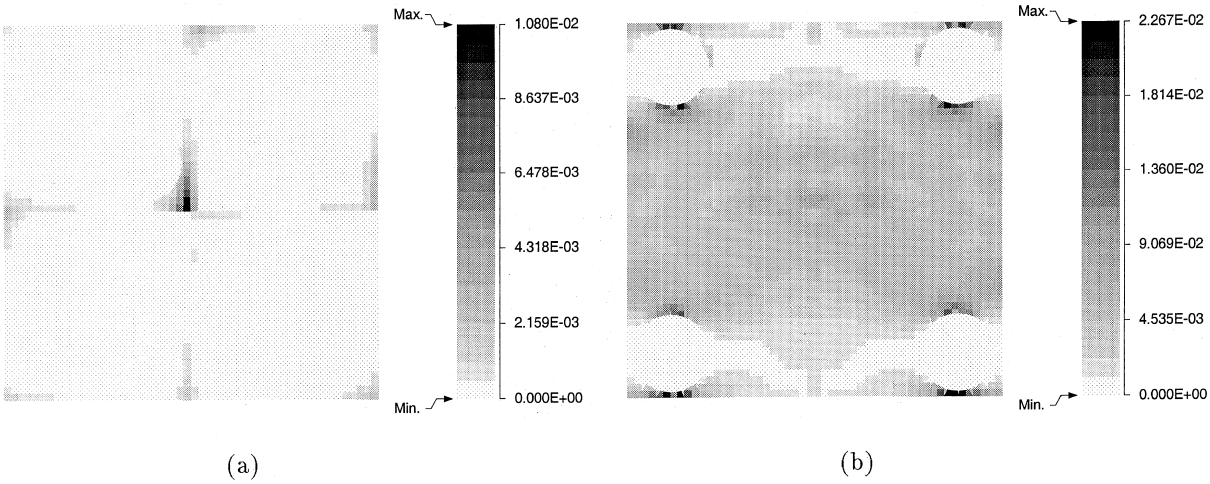

Fig. 10. Distribution of strain energy errors (ASEE) (%) in the final mesh for: (a) composite microstructure of pattern 2 and (b) porous microstructure of pattern 6.

Table 1
Statistics of h–p–$^{\text{enr}}p$-adaptation for the six microstructural patterns of elastic composite materials with circular inclusions

Pattern	Total DOF	Additional DOF by			ATRE (%)	ASE (%)
		h	p	$^{\text{enr}}p$		
1	427	12	4	24	0.63	0.88
2	575	30	34	84	0.36	2.31
3	568	35	22	71	0.53	2.03
4	569	29	39	62	0.47	1.67
5	570	15	44	62	0.55	1.74
6	572	18	45	62	0.46	1.82

(iii) For the pattern 3 also, h–p displacement adaptation is required on both the element boundaries and interfaces. Of these, the boundaries and interfaces near the proximal inclusions require larger number of additional nodes. Additionally, more degrees of freedom are needed on element boundaries near the offset inclusion for satisfying the zero traction condition. All element boundaries that are close to the interfaces require p-adaptation.

(iv) The h–p-adaptation for the patterns 4, 5 and are required on the outer element boundaries where zero traction conditions should be met. This is in contrast to that in pattern 2, since the inclusions are now farther away from one another.

The results of h–p-adaptation in terms of added displacement degrees of freedom, for pattern 6 at the end of the adaptation cycle, are illustrated in Fig. 6. The pre-adaptation nodes are marked with a $\circ$. The x direction nodal adaptations are marked with a $\times$ while those in the y direction are shown with $+$. The p-adaptations are shown with xn or yn, where n is the polynomial order along that directions, for sides with quadratic or higher order interpolation functions only.

A comparison study is made with solutions generated by the commercial code ANSYS [39] for the microstructure of pattern 2. This pattern is chosen since it requires the maximum adaptation in VCFEM (see Table 1) and is therefore significant. The ANSYS mesh, for which convergence is achieved with 4230 QUAD4 elements and 4352 nodes, is shown in Fig. 7(a) and Fig. 8. Plots of the microscopic stresses along horizontal sections A and B of Fig. 4(b) are shown in Fig. 9. Section A passes through the middle of the inclusion while section B barely touches the bottom. The VCFEM results agree very well with those of the

Table 2
Statistics of h–p–$^{\text{enr}}p$-adaptation for the six microstructural patterns of elastic porous materials with circular voids

Pattern	Total DOF	Additional DOF by			ATRE (%)	ASE (%)
		h	p	$^{\text{enr}}p$		
1	591	37	43	52	0.60	2.34
2	613	36	36	84	0.76	3.27
3	641	47	39	120	0.83	3.53
4	656	23	46	130	0.98	3.94
5	669	46	42	140	0.85	3.76
6	675	33	47	162	0.99	4.12

converged ANSYS model. This is also an attestation of the accuracy of the adaptive VCFEM solutions. A contour plot of the strain energy error in the final h–p–$^{\text{enr}}p$ adapted VCFE model for pattern 2 is shown in Fig. 10(a). The error is seen to be uniformly low throughout the entire domain.

Porous material: The matrix material in the microstructure with 4 circular voids is considered to be the same as in the composite. Fig. 5(a) and (b) depict the convergence of VCFEM solutions for the 6 patterns of porous materials with respect to traction reciprocity and strain energy errors. The error reduction with added degrees of freedom from each mode of adaptation, are tallied in Table 2. The maximum overall reduction in traction reciprocity error by the adaptation is found to be approximately 71% with a 28% increase in the degrees of freedom. The reduction in this error with h-adaptation is not as much as for composites. However a more pronounced drop is seen with p-adaptation for reduced increase in degrees of freedom. This is evidenced by the lower slopes in the plots. Additional stress enrichment by $^{\text{enr}}p$-adaptation does not necessarily reduce the traction reciprocity error for all patterns. As a matter of fact, it increases a little for a few patterns. This may be attributed to pollution error emanating from local adaptation. The reduction of strain energy error in Fig. 5(b) is considerable during the 2 cycles of stress function $^{\text{enr}}p$-adaptation. The maximum error in strain energy is for pattern 6, and reduces from 9.3% to 5.7% as a consequence of $^{\text{enr}}p$-adaptation. The top two elements are enriched by 6 polynomial orders ($p+q=2,\ldots,10$) in stress functions, and the bottom two elements by 5 polynomial orders ($p+q=2,\ldots,9$). Rates of convergence in both errors vary from pattern to pattern.

Observations made during the adaptation process of the voided microstructures are essentially similar to those for the composite microstructure with one major difference. The displacement adaptation for the porous material predominantly takes place on the element boundaries and not on the traction free void interfaces. Thus, the h–p-data structure at these interfaces remain unchanged with adaptation.

Pattern 6 is identified as a critical microstructure, for which the error is significantly reduced by adaptation. The accuracy of adapted VCFEM solutions is compared with those from the commercial code ANSYS [39] for this pattern. The converged ANSYS mesh shown in Fig. 7(b) contains 4485 QUAD4 elements with 4700 nodes. Microscopic stresses along horizontal sections A and B in Fig. 4(f) are shown in Fig. 8. Here also, the results agree very well. Fig. 10(b) shows a contour plot of the strain energy error distribution in the final h–p–$^{\text{enr}}p$ adapted VCFE model. Generally speaking, a satisfactorily low error threshold is achieved throughout the entire domain by adaptation.

4.1.2. Effect of heterogeneity size on adapted solutions

The volume fraction of heterogeneities is increased from 12.5% in the previous examples to 63.6% for understanding the effect of size on the quality of adapted solutions. The corresponding dimensions ratio becomes then $r/a = 0.45$. Results for the composite and porous microstructures are compared in Fig. 11(a) and (b) for pattern 1 only. For the same degrees of freedom, the initial traction reciprocity and strain energy errors are considerably larger for the microstructure with higher volume fraction. The adaptive method is however able to reduce the errors significantly with almost the same number of additional degrees of freedom. In general, it can be said that the adaptive VCFEM is equally effective with respect to convergence for all volume fractions without significant difference in the final model sizes.

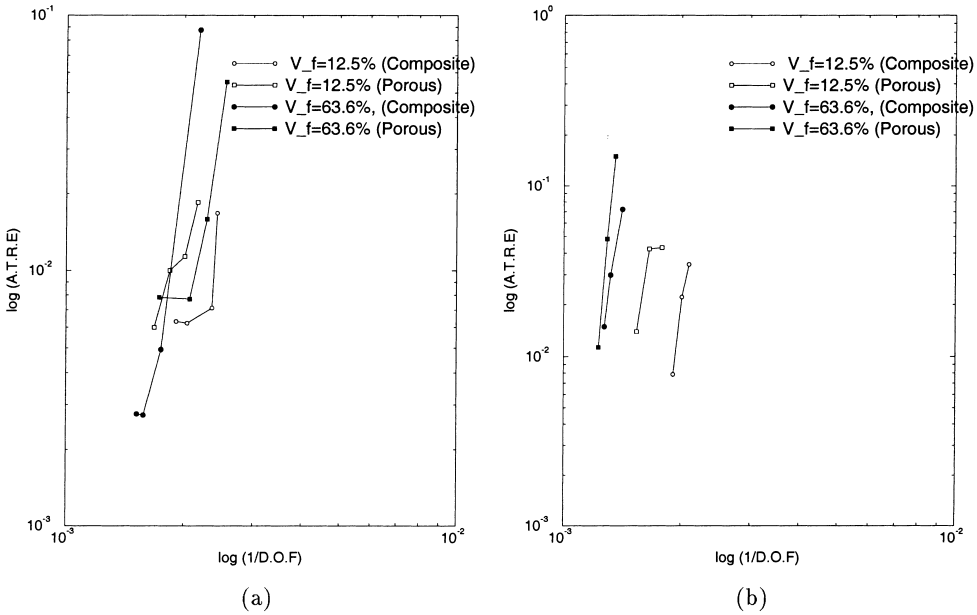

Fig. 11. Effect of heterogeneity size ($r/a = 0.2, 0.45$) on solution the convergence rate for composite and porous microstructural pattern 1: (a) average traction reciprocity error (ATRE) and (b) average strain energy error (ASEE), as functions of inverse of the total degrees of freedom.

4.1.3. Effect of heterogeneity shape on adapted solutions

To examine the effect of shape of heterogeneities on adaptivity and solutions, the circles in Fig. 3 are replaced with ellipses for all the six patterns. The ellipses have aspect ratio $A/B = 3.5$ and have their major axes aligned with the horizontal direction. Other dimensions are given as $\delta/A = 0.25$ and $A/a = 0.2$. The convergence of the VCFEM solutions with adaptation are depicted in Figs. 12 and 13 for the composite and porous materials respectively. The results infer that shape effects do not play any significant role in the quality of solutions and their convergence characteristics for the microstructures considered.

4.1.4. Adaptations with out-of-plane loading for composite microstructures

Micromechanical simulations of fibrous composites that are loaded in the axial directions have been carried out by Pagano and Rybicki [37] for examining the results of effective modulus theory. The boundary value problem considered in [37] is schematically illustrated in Fig. 14. It consists of two rows, each consisting of 8 circular boron fibers along the out of plane or z-direction. Only a quarter of the cross-section is analyzed due to symmetry about the xy and xz planes. The microstructure is subjected to a constant axial strain $\epsilon_{zz} = 1$. The adaptive VCFEM model is used to analyze this problem with generalized plane strain assumptions. The analysis considers two distinct cases viz.:

(i) The bottom edge i.e. $y = 0$ is traction free and top edge $y = 2h$ is a symmetry surface.

(ii) The bottom edge i.e. $y = 0$ is a symmetry surface and top edge $y = 2h$ is traction free.

The fiber radius to edge dimension ratio is $r/h = 0.3$. The material properties for the boron fiber are Young's Modulus $E_{\text{bo}} = 60 \times 10^6$ psi, Poisson's ratio $\nu_{\text{bo}} = 0.2$, and those for the epoxy matrix are Young's modulus $E_{\text{ep}} = 0.5 \times 10^6$ psi, Poisson's ratio $\nu_{\text{ep}} = 0.34$.

The mesh parameters, corresponding to the stress and displacement interpolations, for the initial VCFEM model are the same as those mentioned in Section 4.1.1. The VCFEM solutions are compared with the numerical results of micromechanical analysis provided in [37] and also with those from a finite element analysis with the ANSYS code. The converged ANSYS mesh with 3652 QUAD4 elements and 3773 nodes is shown in Fig. 15.

Fig. 16(a) and (b) show a comparison of the microscopic tensile stress (σ_{xx}) distribution by the three models along the sections $y = 2h$ and $y = h$ for the boundary conditions (i). The VCFEM results here are with h–p-adaptation of displacement degrees of freedom on the element boundaries and interfaces only.

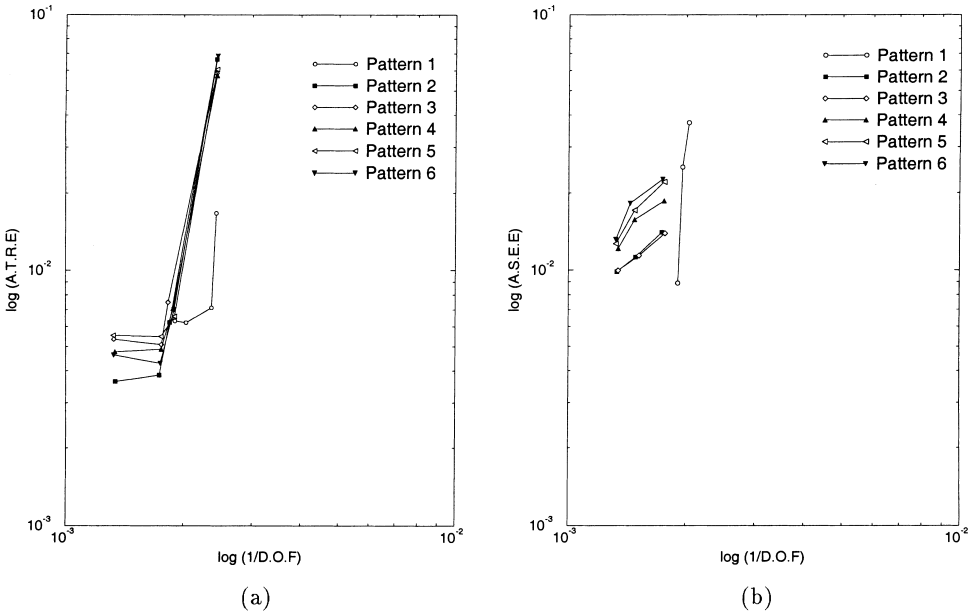

Fig. 12. Effect of heterogeneity shape ($A/B = 3.5$) on solution the convergence rate for composite microstructural patterns: (a) average traction reciprocity error (ATRE) and (b) average strain energy error (ASEE), as functions of inverse of the total degrees of freedom.

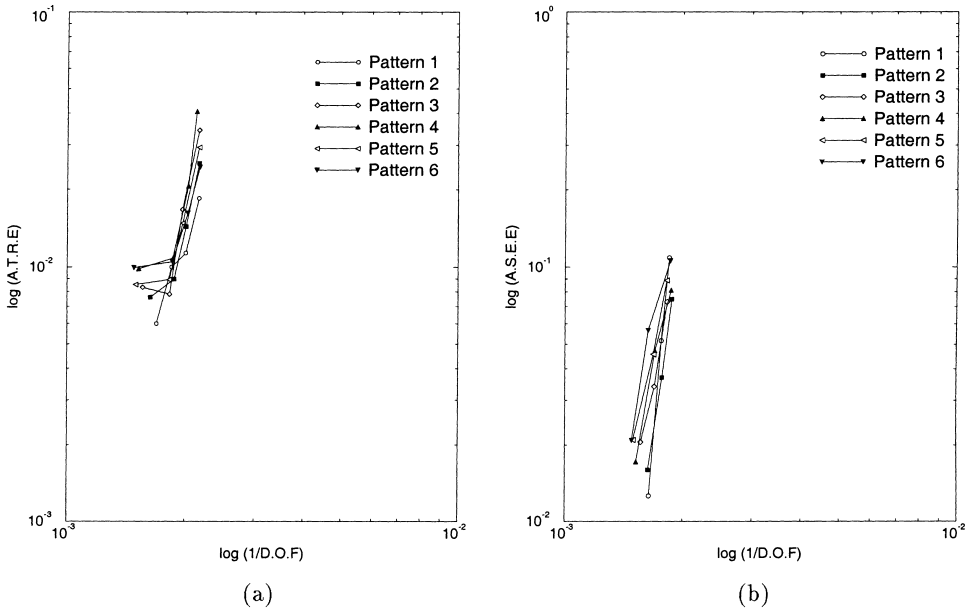

Fig. 13. Effect of heterogeneity shape ($A/B = 3.5$) on solution the convergence rate for porous microstructural patterns: (a) average traction reciprocity error (ATRE) and (b) average strain energy error (ASEE), as functions of inverse of the total degrees of freedom.

Adaptation includes 23 h-adapted nodes and 12 p-adapted nodes. The average traction reciprocity error is reduced from 0.29% to 0.07% as a result. Very good agreement exists among results of the three models. Further adaptation by stress function ${}^{\mathrm{enr}}p$ enrichment results in a drop of the total strain energy error to 0.12% from 0.9833%, with a rise in the number of β parameters from 228 to 280. The convergence of VCFEM solutions with ${}^{\mathrm{enr}}p$-adaptation is shown in Fig. 17.

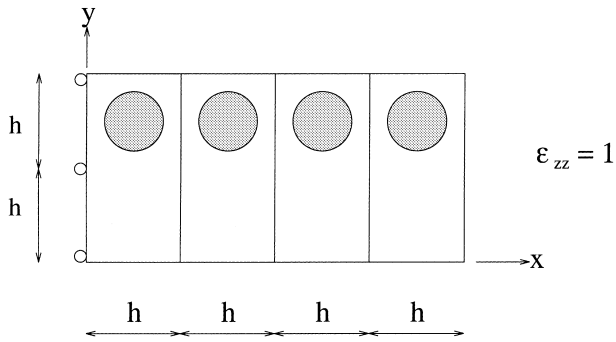

Fig. 14. Schematic view of a quarter of a fibrous composite microstructure with the VCFEM mesh.

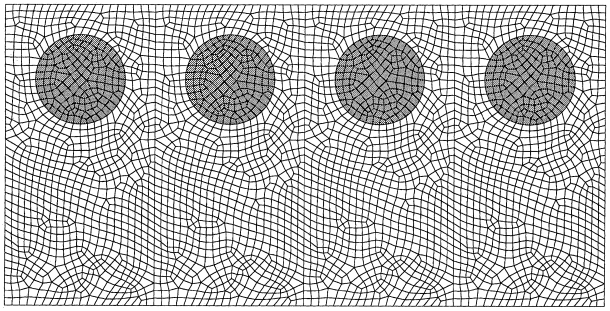

Fig. 15. A converged ANSYS mesh for a quarter of the fibrous composite microstructure.

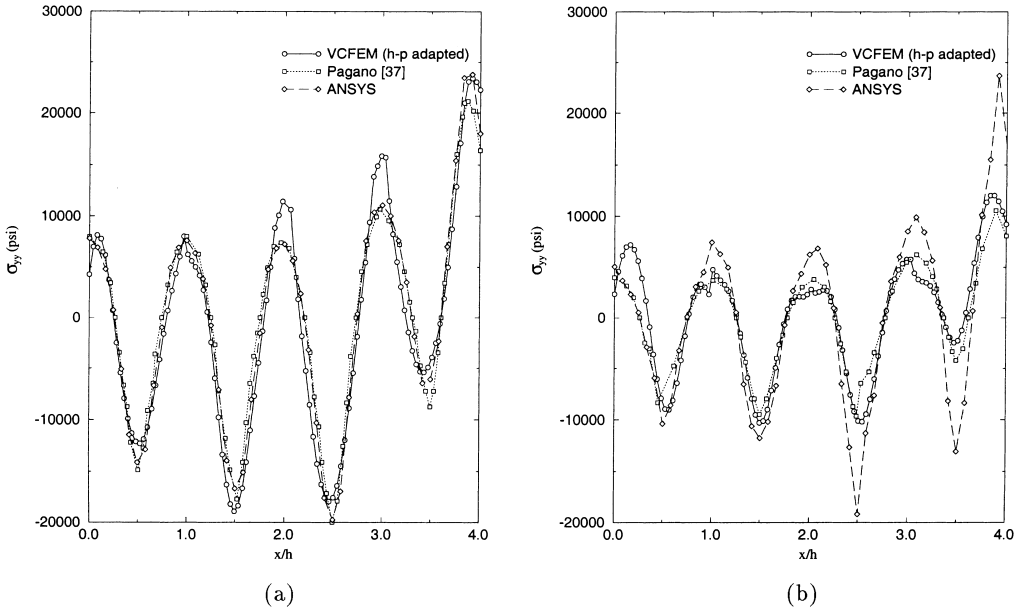

Fig. 16. Comparison plot of the microscopic stress σ_{xx} generated by adapted VCFEM, ANSYS and [37] for boundary conditions (i) along (a) $y = 2h$ and (b) $y = h$.

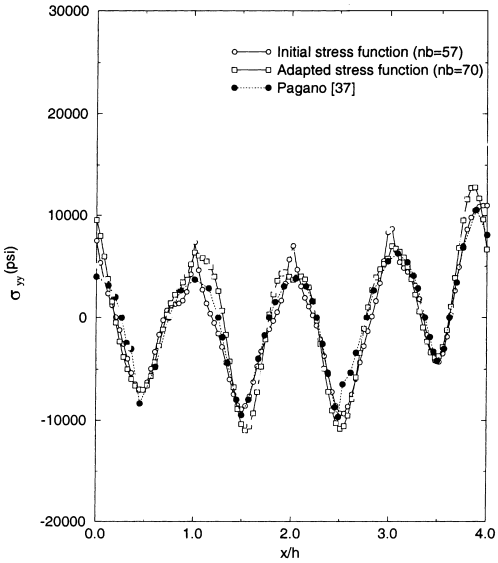

Fig. 17. Convergence of the VCFEM microscopic stress σ_{xx} distribution, with $^{\text{enr}}p$-adaptation for boundary conditions (i) along the line $y = h$.

For the boundary conditions (b), the convergence of the microscopic VCFEM solutions with successive h–p-adaptations are shown in Fig. 18. For this case, the adaptation includes 27 h-adapted nodes and 15 p-adapted nodes. The results are for σ_{xx} at $y = 0$ and $y = h$. A very significant enhancement of the solution is achieved as a consequence of adaptations. The adaptive scheme is able to satisfactorily improve even the transverse solutions for these problems, for which the major stresses are obviously in the axial direction.

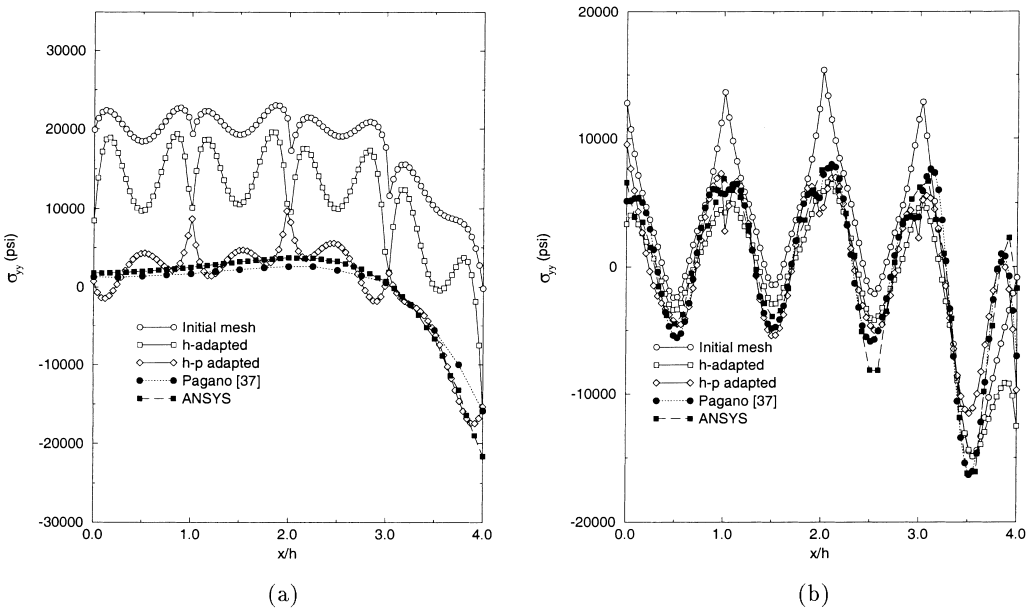

Fig. 18. Convergence of VCFEM results by comparison plot of the microscopic stress σ_{xx} for boundary conditions (ii) along (a) $y = 0$ and (b) $y = h$.

4.2. Elastic–plastic problems

The effectiveness of the adaptive VCFEM model in analyzing problems of work-hardening elasto-plastic matrix materials with embedded elastic inclusions or voids is studied in these examples. The first set of displacement and stress adaptations correspond to those for the elastic solutions. This is the same as discussed in the previous section. The traction reciprocity and strain energy errors are monitored at the end of each increment. If the value of traction reciprocity error (ATRE) exceeds an assumed threshold of 3% during an increment, the displacement field on the element boundaries and interfaces are re-adapted by p-adaptation only. Similarly, if the error in strain energy (ASEE) increases beyond a threshold value of 2.5%, the ${}^{\mathrm{enr}}p$-adaptation increases the stresses polynomials in each element by an order.

4.2.1. Microstructures with different distributions

The patterns 2, 4 and 6 in Fig. 4, with circular inclusions and voids, are re-analyzed for elasto-plasticity. The matrix plasticity is described by the J_2 flow theory with the following properties. *Initial yield stress*: $\sigma_Y = 94$ MPa and *Hardening law*: $\sigma_{\mathrm{eff}} = \sigma_Y + 1.0\bar{\epsilon}^{\mathrm{pl}}$. Each microstructure is loaded to an overall tensile strain $\bar{\epsilon}_{xx} = 1\%$ in 10 equal strain increments.

The evolution in the average traction reciprocity and average strain energy errors for the composite and porous materials are plotted as functions of the evolving overall strain in Figs. 19 and 20 respectively. The abrupt drops in the plots correspond to adaptations at these increments, viz. p-adaptation in Fig. 19(a) and ${}^{\mathrm{enr}}p$-adaptation in Fig. 19(b). Two cycles of each adaptation are required for all the microstructures. Both of these adaptations are effective in reducing and controlling the average ATRE and ASEE errors in the analysis for the duration of the simulation. Adaptation statistics and the average errors at the end of the 10 increments are tabulated in Tables 3 and 4. For both classes of materials, the initial errors ATRE and ASEE after the elastic adaptations are higher for the pattern 2 and remains the highest at the end of the simulation. However the additional degrees of freedom due to adaptation is the largest in pattern 2 for composites, but in pattern 6 for the porous material. The maximum polynomial order in matrix and inclusion stress fields at the end of loading is 10, corresponding to $p + q = 2, \ldots, 10$ in Eqs. (16) and (17). The

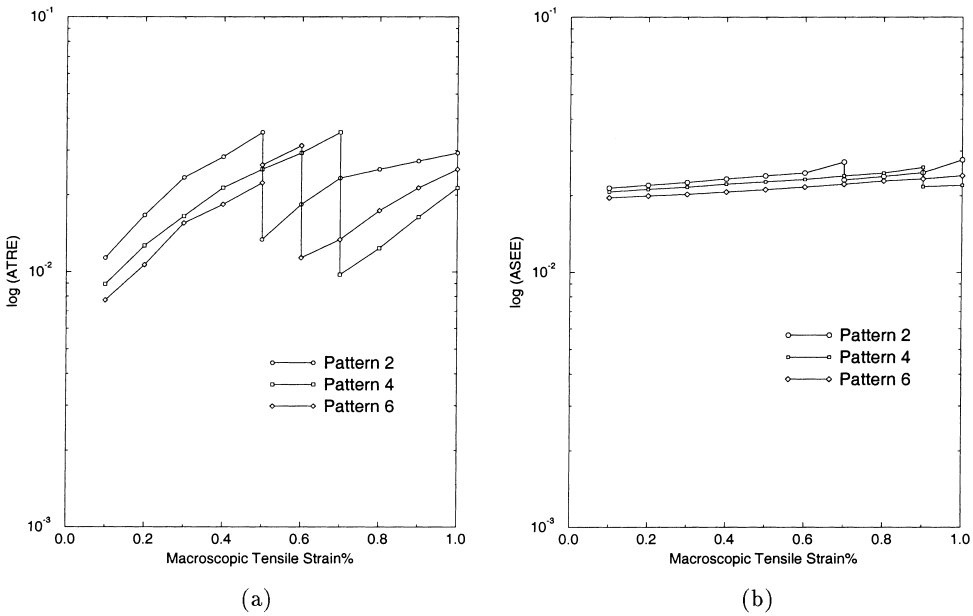

Fig. 19. Evolution of errors in the three elastic–plastic composite microstructures with progressive straining and adaptations: (a) average traction reciprocity error (ATRE) and (b) average strain energy error (ASEE), as functions of overall strain.

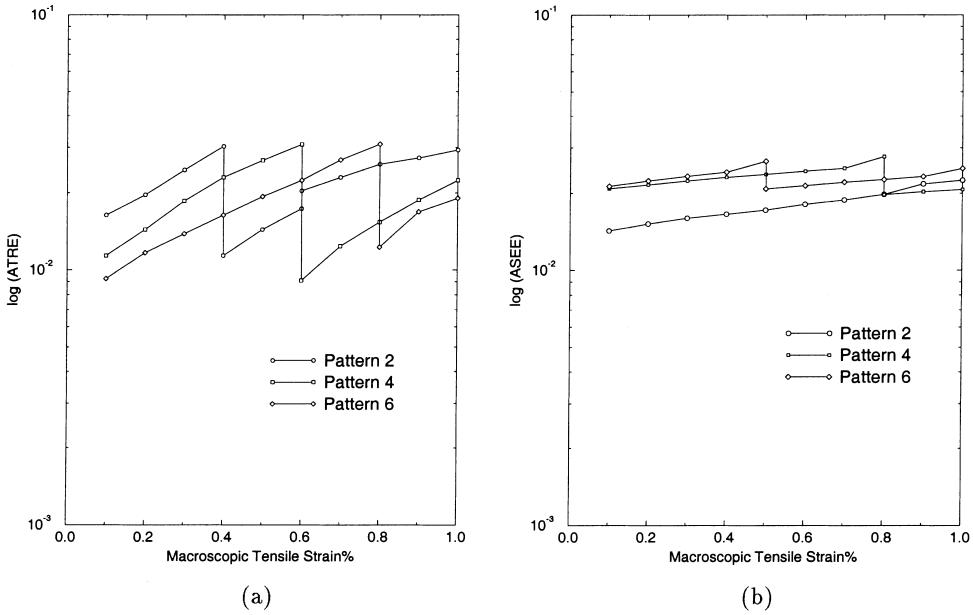

Fig. 20. Evolution of errors in the three elastic–plastic porous microstructures with progressive straining and adaptations: (a) average traction reciprocity error (ATRE) and (b) average strain energy error (ASEE), as functions of overall strain.

Table 3
Statistics of h–p–$^{\text{enr}}p$-adaptation for the three microstructural patterns of elastic–plastic composite materials with circular inclusions

Pattern	Total DOF	Additional DOF by			ATRE (%)	ASE (%)
		h	p	$^{\text{enr}}p$		
2	575	30	42	156	2.56	2.59
4	569	29	44	133	2.37	2.78
6	572	18	51	133	2.16	2.23

Table 4
Statistics of h–p–$^{\text{enr}}p$-adaptation for the three microstructural patterns of elastic–plastic porous materials with circular voids

Pattern	Total DOF	Additional DOF by			ATRE (%)	ASE (%)
		h	p	$^{\text{enr}}p$		
2	675	33	55	202	1.97	1.98
4	656	23	53	170	2.15	2.18
6	613	36	42	124	2.57	2.51

entire sequence of elastic and elastic–plastic adaptations are found to require approximately 50–66% additional degrees of freedom during the complete analysis. In general, the additional degrees of freedom necessary to meet the error criteria are found to be larger for the porous materials than for composites. These results show the capability of the adaptive method for providing accurate solutions for elastic–plastic analyses.

4.2.2. Randomly distributed microstructures with different distributions

In this final example, results of the adaptive VCFEM are compared with those generated in earlier papers [1,2] for randomly packed hard-core composite and porous microstructures. Comparison of a few section plots of microscopic stresses by the unadapted VCFEM with a very dense and converged ANSYS mesh, showed some differences in the peak values in [1,2]. The strength of the adaptive scheme is tested for these problems. The microstructures consist of 29 randomly distributed heterogeneities (inclusions and voids) packed in a hard-core pattern, corresponding to volume fraction $V_f = 20\%$, in a $L \times L$ square region. Details of the microstructure generation process as discussed in [2]. The VCFEM mesh consists of 29 elements as shown in Fig. 21(a). The converged ANSYS mesh for the composite material consists of 8000 QUAD4 elements as shown in Fig. 21(b) and for the porous material consists of 5282 QUAD4 elements. The matrix material is aluminum with the following properties:

Young's modulus: $E_{al} = 69$ GPa,
Poisson's ratio: $\nu_{al} = 0.33$;
Initial yield stress: $\sigma_Y = 43$ MPa
Hardening law:$\sigma_{eff} = \sigma_Y + \epsilon_{eff}^{0.125}$.

The composite material consists of elastic boron inclusions with Young's Modulus: $E_{bo} = 420$ GPa, Poisson's ratio $\nu_{bo} = 0.2$.

Uniform tension is applied on the edge $x = L$ upto a maximum macroscopic tensile strain of (a) $\bar{\epsilon}_{xx} = 0.5\%$ for the composite microstructure and (b) $\bar{\epsilon}_{xx} = 0.8\%$ for the porous microstructure, in 10 equal increments. The transverse face $y = L$ is traction free and $x = 0$ and $y = 0$ are symmetry faces. The evolution of the traction reciprocity error and strain energy error in the VCFEM simulations with strain increments and h–p–$^{\text{enr}}p$-adaptations are shown in Fig. 22. As mentioned in the previous example, p-adaptation of the displacement field is activated when the average traction reciprocity error exceeds a predetermined cut-off value $e^{\text{T}}_{\text{cut-off}} = 2.5\%$ at any increment. Stress field enrichment or $^{\text{enr}}p$-adaptation is performed when the total strain energy error in the entire domain, or $N * (\text{ASEE}) \leqslant 10\%$. After the elastic adaptations, the composite microstructure undergoes one p-adaptation and one $^{\text{enr}}p$-adaptation, while the porous microstructure is subjected to two p-adaptation and one $^{\text{enr}}p$-adaptation.

For the composite, the microstructural tensile stress distribution σ_{xx} along two sections $x/L = 0.4$ and $x/L = 0.7$ at the end of loading i.e. $\bar{\epsilon}_{xx} = 0.5\%$ are plotted in Fig. 23(a) and (b). The same plots for the unadapted model are also shown in [2]. Significant improvements with adaptation are observed through the concurrence in the ANSYS and adapted VCFEM results for both sections. Likewise, the adapted VCFEM solution for the porous microstructure is compared with those from ANSYS and the unadapted VCFEM (see [1]) in Fig. 24. The section plot of microstructural tensile stress is along $x/L = 0.5$ at the end of loading for a macroscopic tensile strain of $\bar{\epsilon}_{xx} = 0.8\%$. A very close match is observed for the adapted VCFEM and

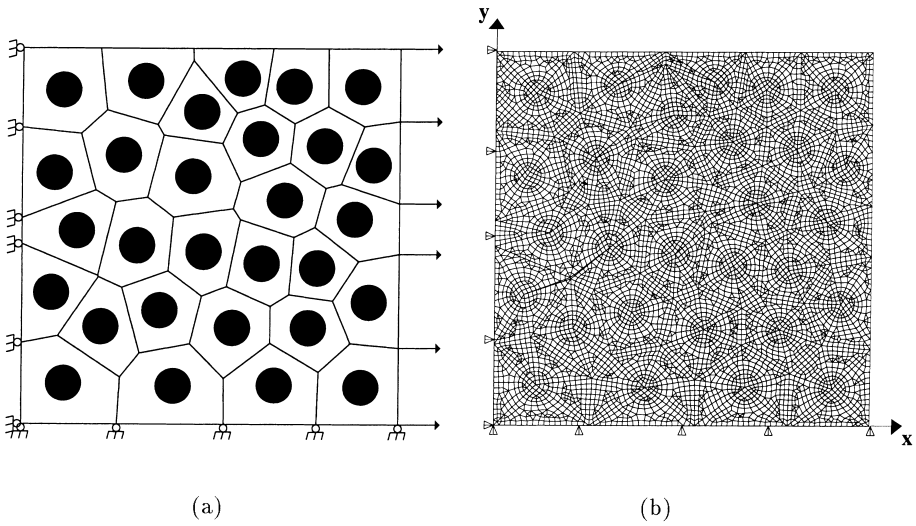

Fig. 21. (a) VCFEM mesh and (b) a converged ANSYS mesh for a randomly distributed with circular inclusions ($V_f = 20\%$).

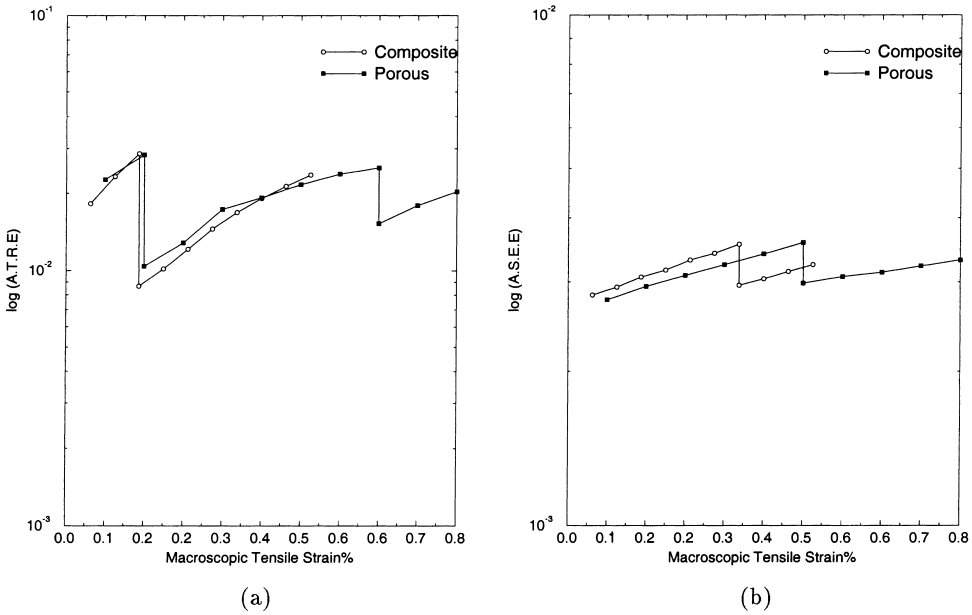

Fig. 22. Evolution of errors in the randomly packed elastic–plastic composite and porous microstructures with progressive straining and adaptations: (a) average traction reciprocity error (ATRE) and (b) average strain energy error (ASEE), as functions of overall strain.

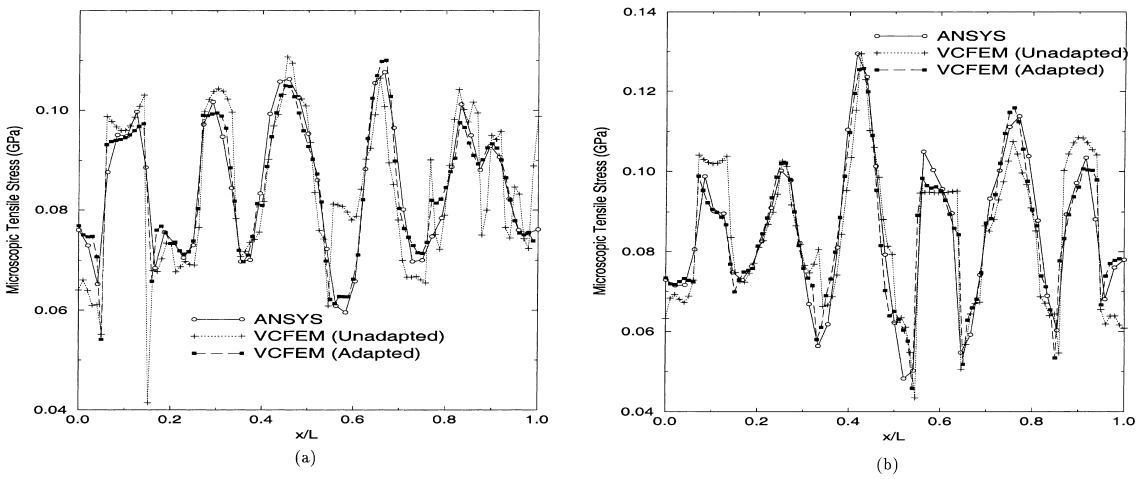

Fig. 23. Convergence of VCFEM results with adaptation, shown for the microscopic stress σ_{xx} in a randomly packed composite microstructure along (a) $x/L = 0.4$ and (b) $x/L = 0.7$, at macroscopic strain $\bar{\epsilon}_{xx}$ =0.5%.

ANSYS results. The effectiveness of the adaptive VCFEM in convergence with respect to accurate results for various morphologies in composite and porous microstructures are evident from this example.

5. Conclusions

An adaptive methodology has been developed in this paper to enhance convergence characteristics and accuracy of the Voronoi cell finite element model for analyzing heterogeneous materials. The effectiveness of the adaptive scheme is established for various morphologies, material properties (elastic and elasto-plastic) and heterogeneities (inclusions and voids). Two error measures are introduced and developed to

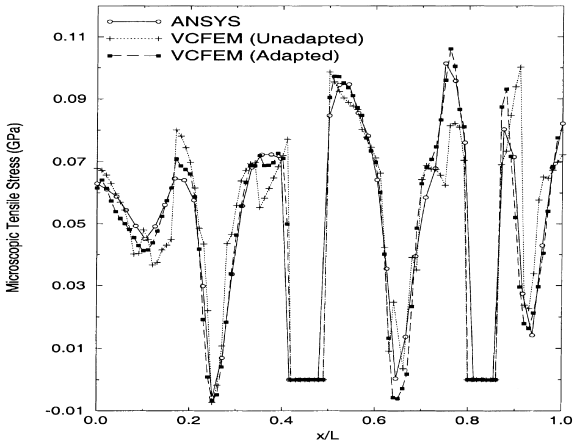

Fig. 24. Convergence of VCFEM results with adaptation, shown for the microscopic stress σ_{xx} in a randomly packed porous microstructure along $x/L = 0.5$ at macroscopic strain $\bar{\epsilon}_{xx}$ =0.8%.

measure the quality of the current VCFEM solution. They are (i) the traction reciprocity error, derived a posteriori from the element and interface traction discontinuity in the finite element solution, and (ii) the error in kinematic relationships that is equated to an error in the strain energy. Displacement adaptations to minimize traction discontinuity are implemented through a boundary refinement or h-adaptation and polynomial enrichment or p-adaptation to approach the 'optimal' directions. These directions optimize the virtual work done by the traction discontinuity in the finite element solution and are obtained as the restrictions of the traction discontinuity along a basis, orthogonal to the displacement field. The strain energy or kinematic relation error is proved to be minimized by enhancing the stress functions through polynomial enrichment or ${}^{\mathrm{enr}}p$-adaptation. Enhancement in the matrix and inclusion phases improves the solution quality in each phase.

A number of numerical examples are solved to demonstrate the effectiveness of the adaptive strategy for various phase distributions, shapes and sizes; different materials viz. elastic and elastic plastic; and different heterogeneities, viz. stiffer inclusions and voids. Both the traction reciprocity and strain energy errors are found to be very to be effective indicators of solution quality. They uniformly provide very good convergence rates and characteristics irrespective of distribution, size or shape. The location and extent of displacement adaptations are found to depend on phase distributions, such as proximity of heterogeneities to one another and to the domain boundary, and size. The h-adaptations, on the element boundaries and interfaces have a more pronounced effect in reducing the overall traction reciprocity error for composites than for porous materials. For voids however, subsequent p-adaptation provides considerable reduction in the traction discontinuity error. Stress function enrichment with ${}^{\mathrm{enr}}p$-adaptation is found to be more necessary in porous materials for reducing strain energy error. This results in a fairly higher order polynomials ($\approx \mathrm{O}(9-10)$) in stress fields for porous matrices than for composites ($\approx \mathrm{O}(6-7)$). However the total degrees of freedom required for accuracy are still approximately the same.

In the plastic range, the evolving non-linear microstructural response requires constant monitoring to ensure convergence of the solution with respect to the error indicators. In these problems, the initial h–p-adaptation is conducted with the elastic solutions. Subsequent p- and ${}^{\mathrm{enr}}p$-adaptations of the displacement and stress fields are done on a necessity basis depending on error indicators in each increment. The traction discontinuity and strain energy errors evolve and are therefore generally larger for elastic–plastic than for elastic problems. In conclusion, the adaptive VCFEM is demonstrated to be a very effective tool for accurate and efficient modeling of heterogeneous materials. Consequently, it can be an ideal materials modeling tool for multiple scale analysis of composite and porous materials. While the effectiveness of VCFEM in analyzing polyhedral shaped heterogeneities has not been addressed in this paper, various simple polyhedral shapes have been analyzed by this method, using a fourier expansion of the interface, in [1,4–6]. Due to the limitations of the fourier series expansion in modelling irregular shapes, complex non-convex polyhedral shapes may not be easily solved using the current approach.

Acknowledgements

The authors would like to thank Professor J.T. Oden for raising this issue and hence suggesting the problem. This work has been sponsored by the Unites States Air Force Office Of Scientific Research through grant no. f49620-98-1-01-93 (Program Director: Dr. Ozden O. Ochoa), and by the Mechanics and Materials program of National Science Foundation (Program Director Dr. S. Saigal) through an NSF Young Investigator grant (grant no. CMS-9457603). Computer support by the Ohio Supercomputer Center through grant # PAS813-2 is also gratefully acknowledged.

Appendix A. Expansion of an analytical solution in terms of the reciprocal basis in VCFEM

The exact stress function in the matrix of an infinite place with an arbitrary oriented elliptical void, that is loaded in tension, has been given in [36] as

$$\Phi^{\mathrm{M}}_{\mathrm{exact}} = Re(\bar{z}(Ac\cosh\zeta + Bc\sinh\zeta) + C\zeta + Dc^2\cosh 2\zeta + Ec^2\sinh 2\zeta) \tag{A.1}$$

with

$$z = x + \mathrm{i}y = (c\cosh\xi\cos\eta) + \mathrm{i}(c\sinh\xi\sin\eta), \quad \zeta = \xi + \mathrm{i}\eta. \tag{A.2}$$

The coordinates (ξ, η) are defined as elliptic coordinates in [36]. For an ellipse, the conformal mapping function f in Eq. (14) is related to ξ as

$$\tanh(\xi) = \frac{f - m/f}{f + m/f} = \frac{1 - m/f^2}{1 + m/f^2}, \tag{A.3}$$

where $m = (a-b)/(a+b)$ is the geometric eccentricity of the ellipse. Rewriting functions of ζ in Eq. (A.1) in terms of x and y and using Eq. (A.2) the following identities are obtained:

$$\begin{aligned} Re(\bar{z}c\cosh\zeta) &= Re(\bar{z}(c\cosh(\xi+\mathrm{i}\eta))) = Re(\bar{z}(c\cosh\xi\cos\eta + \mathrm{i}c\sinh\xi\sin\eta)) \\ &= Re(\bar{z}(x+\mathrm{i}y)) = x^2 + y^2, \end{aligned} \tag{A.4}$$

$$\begin{aligned} Re(\bar{z}c\sinh\zeta) &= Re(\bar{z}(c\sinh(\xi+\mathrm{i}\eta))) = Re(\bar{z}(c\sinh\xi\cos\eta + \mathrm{i}c\cosh\xi\sin\eta)) \\ &= Re(\bar{z}(x\tanh\xi + \mathrm{i}y\coth\xi)) = x^2\tanh\xi + y^2\coth\xi, \end{aligned} \tag{A.5}$$

$$\begin{aligned} Re(c^2\cosh 2\zeta) &= c^2(\cosh 2\xi\cos 2\eta) = c^2(\cosh^2\xi + \sinh^2\xi)(\cos^2\eta - \sin^2\eta) \\ &= x^2 - y^2 + x^2\tanh^2\xi - y^2\coth^2\xi, \end{aligned} \tag{A.6}$$

$$\begin{aligned} Re(c^2\sinh 2\zeta) &= c^2(\sinh 2\xi\cos 2\eta) = 2c^2\sinh\xi\cosh\xi(\cos^2\eta - \sin^2\eta) \\ &= 2(x^2\tanh\xi - y^2\coth\xi). \end{aligned} \tag{A.7}$$

Substituting Eqs. (A.3)–(A.7) in Eq. (A.1) the stress function takes the form:

$$\begin{aligned} \Phi^{m}_{\mathrm{exact}} &= A^*x^2 + B^*y^2 + C^*x^2\frac{1-m/f^2}{1+m/f^2} + D^*y^2\frac{1+m/f^2}{1-m/f^2} + E^*x^2\frac{(1+m/f^2)^2}{(1-m/f^2)^2} \\ &\quad + F^*y^2\frac{(1-m/f^2)^2}{(1+m/f^2)^2} + G^*\tanh^{-1}\frac{1-m/f^2}{1+m/f^2} \\ &\approx A^*x^2 + B^*y^2 + C^*x^2(1 - 2m/f^2 + 2m^2/f^4 + \mathrm{O}(1/f^6)) \\ &\quad + D^*y^2(1 + 2m/f^2 - 2m^2/f^4 + \mathrm{O}(1/f^6)) + E^*x^2(1 + 4m/f^2 + 8m^2/f^4 + \mathrm{O}(1/f^6)) \\ &\quad + F^*y^2(1 - 4m/f^2 + 8m^2/f^4 + \mathrm{O}(1/f^6)) + G^*(H^* + \log f + \mathrm{O}(1/f^4)), \end{aligned}$$

where the series expansion is performed with the symbolic manipulator MAPLE [38] and (A^*, B^*, C^*, D^*, E^*, F^*, G^*, H^*) are linear combinations of the constants (A, B, C, D, E, and c).

Appendix B. Error estimate from variation in element strain energy

The variations in strain energy of the constituent matrix and inclusion phases of the Voronoi cell element can be written as functions of stress variations as

$$ {}_e\mathsf{a}^{\mathrm{M}}(\triangle\boldsymbol{\sigma}^{\mathrm{M}}_{eH} + \mathrm{d}\boldsymbol{\sigma}^{\mathrm{M}}_{e}, \delta\boldsymbol{\sigma}^{\mathrm{M}}_{e}) = {}_e\mathsf{b}^{\mathrm{M}}_{\mathrm{E}}(\delta\boldsymbol{\sigma}^{\mathrm{M}}_{eH} + {}^*\delta\boldsymbol{\sigma}^{\mathrm{M}}_{e}, \triangle\mathbf{u}^{\mathrm{E}}_{eH} + \mathrm{d}\mathbf{u}^{\mathrm{E}}_{e}) - {}_e\mathsf{b}^{\mathrm{M}}_{\mathrm{I}}(\delta\boldsymbol{\sigma}^{\mathrm{M}}_{eH} + {}^*\delta\boldsymbol{\sigma}^{\mathrm{M}}_{e}, \triangle\mathbf{u}^{\mathrm{I}}_{eH} + \mathrm{d}\mathbf{u}^{\mathrm{I}}_{e}) \tag{B.1}$$

and therefore

$$\begin{aligned} &{}_e\mathsf{a}^{\mathrm{M}}(\triangle\boldsymbol{\sigma}^{\mathrm{M}}_{eH}, \delta\boldsymbol{\sigma}^{\mathrm{M}}_{eH} + {}^*\delta\boldsymbol{\sigma}^{\mathrm{M}}_{e}) + {}_e\mathsf{a}^{\mathrm{M}}(\mathrm{d}\boldsymbol{\sigma}^{\mathrm{M}}_{e}, \delta\boldsymbol{\sigma}^{\mathrm{M}}_{eH} + {}^*\delta\boldsymbol{\sigma}^{\mathrm{M}}_{e}) \\ &\quad = {}_e\mathsf{b}^{\mathrm{M}}_{\mathrm{E}}(\delta\boldsymbol{\sigma}^{\mathrm{M}}_{eH}, \triangle\mathbf{u}^{\mathrm{E}}_{eH}) + {}_e\mathsf{b}^{\mathrm{M}}_{\mathrm{E}}({}^*\delta\boldsymbol{\sigma}^{\mathrm{M}}_{e}, \triangle\mathbf{u}^{\mathrm{E}}_{eH}) + {}_e\mathsf{b}^{\mathrm{M}}_{\mathrm{E}}(\delta\boldsymbol{\sigma}^{\mathrm{M}}_{e}, \mathrm{d}\mathbf{u}^{\mathrm{E}}_{e}) - {}_e\mathsf{b}^{\mathrm{M}}_{\mathrm{I}}(\delta\boldsymbol{\sigma}^{\mathrm{M}}_{eH}, \triangle\mathbf{u}^{\mathrm{I}}_{eH}) \\ &\qquad - {}_e\mathsf{b}^{\mathrm{M}}_{\mathrm{I}}({}^*\delta\boldsymbol{\sigma}^{\mathrm{M}}_{e}, \triangle\mathbf{u}^{\mathrm{I}}_{eH}) - {}_e\mathsf{b}^{\mathrm{M}}_{\mathrm{I}}(\delta\boldsymbol{\sigma}^{\mathrm{M}}_{e}, \mathrm{d}\mathbf{u}^{\mathrm{I}}_{e}), \end{aligned} \tag{B.2}$$

where the substitution $\delta\boldsymbol{\sigma}^{\mathrm{M}}_{e} = \delta\boldsymbol{\sigma}^{\mathrm{M}}_{eH} + {}^*\delta\boldsymbol{\sigma}^{\mathrm{M}}_{e}$ is made. From the orthogonality conditions in Eq. (44) and also the fact that the weak form in Eq. (7) is satisfied in the approximation space, it can be concluded that

$$ {}_e\mathsf{a}^{\mathrm{M}}(\mathrm{d}\boldsymbol{\sigma}^{\mathrm{M}}_{e}, \delta\boldsymbol{\sigma}^{\mathrm{M}}_{e}) = {}_e\mathsf{b}^{\mathrm{M}}_{\mathrm{E}}(\triangle{}^*\delta\boldsymbol{\sigma}^{\mathrm{M}}_{e}, \mathbf{u}^{\mathrm{E}}_{eH}) - {}_e\mathsf{b}^{\mathrm{M}}_{\mathrm{I}}({}^*\delta\boldsymbol{\sigma}^{\mathrm{M}}_{e}, \triangle\mathbf{u}^{\mathrm{I}}_{eH}) + {}_e\mathsf{b}^{\mathrm{M}}_{\mathrm{E}}(\delta\boldsymbol{\sigma}^{\mathrm{M}}_{e}, \mathrm{d}\mathbf{u}^{\mathrm{E}}_{e}) - {}_e\mathsf{b}^{\mathrm{M}}_{\mathrm{I}}(\delta\boldsymbol{\sigma}^{\mathrm{M}}_{e}, \mathrm{d}\mathbf{u}^{\mathrm{I}}_{e}) $$

and similarly

$$ {}_e\mathsf{a}^{\mathrm{I}}(\mathrm{d}\boldsymbol{\sigma}^{\mathrm{I}}_{eH}, \delta\boldsymbol{\sigma}^{\mathrm{I}}_{e}) = {}_e\mathsf{b}^{\mathrm{I}}_{\mathrm{I}}({}^*\delta\boldsymbol{\sigma}^{\mathrm{I}}_{e}, \triangle\mathbf{u}^{\mathrm{I}}_{eH}) + {}_e\mathsf{b}^{\mathrm{I}}_{\mathrm{I}}(\delta\boldsymbol{\sigma}^{\mathrm{I}}_{e}, \mathrm{d}\mathbf{u}^{\mathrm{I}}_{e}). \tag{B.3}$$

An upper bound for the total error in the strain energy is then obtained by adding the left hand sides in Eq. (B.3) and applying Cauchy–Schwarz inequality as

$$\begin{aligned} &\left| \sum_{e=1}^{N} e\mathsf{a}^{\mathrm{E}}(\mathrm{d}\boldsymbol{\sigma}^{\mathrm{E}}_{e}, \mathrm{d}\boldsymbol{\sigma}^{\mathrm{E}}_{e}) + {}_e\mathsf{a}^{\mathrm{I}}(\mathrm{d}\boldsymbol{\sigma}^{\mathrm{E}}_{e}, \mathrm{d}\boldsymbol{\sigma}^{\mathrm{I}}_{e}) \right| \\ &\quad \leqslant \left| \sum_{e=1}^{N} \{ {}_e\mathsf{b}^{\mathrm{M}}_{\mathrm{E}}(\mathrm{d}\boldsymbol{\sigma}^{\mathrm{M}}_{e}, \mathrm{d}\mathbf{u}^{\mathrm{E}}_{e}) - {}_e\mathsf{b}^{\mathrm{M}}_{\mathrm{I}}(\mathrm{d}\boldsymbol{\sigma}^{\mathrm{M}}_{e}, \mathrm{d}\mathbf{u}^{\mathrm{I}}_{e}) + {}_e\mathsf{b}^{\mathrm{I}}_{\mathrm{I}}(\mathrm{d}\boldsymbol{\sigma}^{\mathrm{I}}_{e}, \mathrm{d}\mathbf{u}^{\mathrm{I}}_{e}) \} \right| \\ &\qquad + \left| \sum_{e=1}^{N} \{ {}_e\mathsf{b}^{\mathrm{M}}_{\mathrm{E}}({}^*\mathrm{d}\boldsymbol{\sigma}^{\mathrm{M}}_{e}, \triangle\mathbf{u}^{\mathrm{E}}_{eH}) - {}_e\mathsf{b}^{\mathrm{M}}_{\mathrm{I}}({}^*\mathrm{d}\boldsymbol{\sigma}^{\mathrm{M}}_{e}, \triangle\mathbf{u}^{\mathrm{I}}_{eH}) \} \right| + \left| \sum_{e=1}^{N} \{ {}_e\mathsf{b}^{\mathrm{I}}_{\mathrm{I}}({}^*\mathrm{d}\boldsymbol{\sigma}^{\mathrm{I}}_{e}, \triangle\mathbf{u}^{\mathrm{I}}_{eH}) \} \right| \\ &\quad \leqslant \left| \left[\sup_{\forall \mathrm{d}\mathbf{u}^{\mathrm{E/I}}_{e} \in \mathscr{V}^{\mathrm{E/I}}_{e}} \sum_{e=1}^{N} \{ {}_e\mathsf{b}^{\mathrm{M}}_{\mathrm{E}}(\mathrm{d}\boldsymbol{\sigma}^{\mathrm{M}}_{e}, \mathrm{d}\mathbf{u}^{\mathrm{E}}_{e}) - {}_e\mathsf{b}^{\mathrm{M}}_{\mathrm{I}}(\mathrm{d}\boldsymbol{\sigma}^{\mathrm{M}}_{e}, \mathrm{d}\mathbf{u}^{\mathrm{I}}_{e}) + {}_e\mathsf{b}^{\mathrm{I}}_{\mathrm{I}}(\mathrm{d}\boldsymbol{\sigma}^{\mathrm{I}}_{e}, \mathrm{d}\mathbf{u}^{\mathrm{I}}_{e}) \} \right] \right| \\ &\qquad + \left[\sum_{e=1}^{N} \left| \{ {}_e\mathsf{b}^{\mathrm{M}}_{\mathrm{E}}({}^*\mathrm{d}\boldsymbol{\sigma}^{\mathrm{M}}_{e}, \triangle\mathbf{u}^{\mathrm{E}}_{eH}) - {}_e\mathsf{b}^{\mathrm{M}}_{\mathrm{I}}({}^*\mathrm{d}\boldsymbol{\sigma}^{\mathrm{M}}_{e}, \triangle\mathbf{u}^{\mathrm{I}}_{eH}) \} \right| + \sum_{e=1}^{N} \left| \{ {}_e\mathsf{b}^{\mathrm{I}}_{\mathrm{I}}({}^*\mathrm{d}\boldsymbol{\sigma}^{\mathrm{I}}_{e}, \triangle\mathbf{u}^{\mathrm{I}}_{eH}) \} \right| \right]. \end{aligned}$$

Appendix C. Optimal directions for enrichment of displacement fields

Optimal displacement enrichments can be obtained as stationary points for the augmented functional in Eq. (60), corresponding to the traction reciprocity error

$$\begin{aligned} {}_{\tilde{e}}\tilde{\mathsf{g}}^{\mathrm{E/I}}({}^*\delta\mathbf{u}^{\mathrm{E/I}}_{\tilde{e}H}, \lambda_1, \lambda_2) &= {}_{\tilde{e}}\tilde{\mathsf{b}}^{\mathrm{E/I}}([[\mathbf{t}]]^{\tilde{e}/,\tilde{e}_{\mathrm{I}}}_{H}, {}^*\delta\mathbf{u}^{\mathrm{E/I}}_{\tilde{e}H}) + \lambda_1 \int_{\partial\Omega^{\mathrm{E/I}}_{e}} \delta\mathbf{u}^{\mathrm{E/I}}_{\tilde{e}H} \cdot {}^*\delta\mathbf{u}^{\mathrm{E/I}}_{\tilde{e}H} \ \mathrm{d}\Omega \\ &\quad - \frac{\lambda_2}{2} \int_{\partial\Omega^{\mathrm{E/I}}_{e}} \left[{}^*\delta\mathbf{u}^{\mathrm{E/I}}_{\tilde{e}H} \cdot {}^*\delta\mathbf{u}^{\mathrm{E/I}}_{\tilde{e}H} \ \mathrm{d}\Omega - \varepsilon^2 \right]. \end{aligned}$$

Equating the derivatives of ${}_{\tilde{e}}\tilde{\mathsf{g}}^{\mathrm{E/I}}({}^*\delta\mathbf{u}^{\mathrm{E/I}}_{\tilde{e}H}, \lambda_1, \lambda_2)$ with respect to ${}^*\delta\mathbf{u}_{\tilde{e}H}$ to zero, yields the optimal adaptivity direction as the solutions to the equations

$$\frac{\partial}{\partial {}^*\mathbf{u}_{eH}^{\mathrm{E/I}}}\left[{}_{\tilde{e}}\tilde{\mathsf{b}}^{\mathrm{E/I}}([[\mathbf{t}]]_H^{\tilde{e}/,\tilde{e}_1}, {}^*\delta\mathbf{u}_{\tilde{e}H}^{\mathrm{E/I}}) + \lambda_1 \int_{\partial\Omega_e^{\mathrm{E/I}}} \delta\mathbf{u}_{\tilde{e}H}^{\mathrm{E/I}} \cdot {}^*\delta\mathbf{u}_{\tilde{e}H}^{\mathrm{E/I}}\ \mathrm{d}\Omega \right.$$
$$\left. - \lambda_2 \int_{\partial\Omega_e^{\mathrm{E/I}}} ({}^*\delta\mathbf{u}_{\tilde{e}H}^{\mathrm{E/I}} \cdot {}^*\delta\mathbf{u}_{\tilde{e}H}^{\mathrm{E/I}}\ \mathrm{d}\Omega - \varepsilon^2)\right] = 0 \quad \forall\delta\mathbf{u}_{\tilde{e}H} \in \mathscr{V}_{eH}$$

or

$$_{\tilde{e}}\tilde{\mathsf{b}}^{\mathrm{E/I}}([[\mathbf{t}]]_H^{\tilde{e}/,\tilde{e}_1}, {}^*\mathbf{1}) + \lambda_1 \int_{\partial\Omega_e^{\mathrm{E/I}}} \delta\mathbf{u}_{\tilde{e}H}^{\mathrm{E/I}} \cdot {}^*\mathbf{1}\ \mathrm{d}\Omega - \lambda_2 \int_{\partial\Omega_e^{\mathrm{E/I}}} ({}^*\delta\mathbf{u}_{\tilde{e}H}^{\mathrm{E/I}} \cdot {}^*\mathbf{1})\ \mathrm{d}\Omega = 0, \tag{C.1}$$

where ${}^*\mathbf{1} \in^{\perp} \mathscr{V}_{eH}$ is a unity function. An explicit assumption made in Eq. (C.1) is that the boundary $\partial\Omega_e^{\mathrm{E}}$ and interface $\partial\Omega_e^{\mathrm{I}}$ are fixed. Setting the derivatives of ${}_{\tilde{e}}\tilde{\mathsf{g}}^{\mathrm{E/I}}({}^*\delta\mathbf{u}_{\tilde{e}H}^{\mathrm{E/I}}, \lambda_1, \lambda_2)$ with respect to λ_1 and λ_2 to zero yields the constraint conditions Eq. (45) and (59) respectively in terms of the optimal displacement enrichment ${}^*_{\mathrm{opt}}\delta\mathbf{u}_{eH}^{\mathrm{E/I}}$, i.e.

$$\begin{aligned} &\int_{\partial\Omega_e^{\mathrm{E/I}}} \delta\mathbf{u}_{eH}^{\mathrm{E/I}} \cdot {}^*_{\mathrm{opt}}\delta\mathbf{u}_{eH}^{\mathrm{E/I}}\ \mathrm{d}\Omega = 0 \quad \forall(\delta\mathbf{u}_{eH}, {}^*\delta\mathbf{u}_{eH}) \in (\mathscr{V}_{eH}, {}^{\perp}\mathscr{V}_{eH}) \\ &\int_{\partial\Omega_e^{\mathrm{E/I}}} {}^*_{\mathrm{opt}}\delta\mathbf{u}_{eH}^{\mathrm{E/I}} \cdot {}^*_{\mathrm{opt}}\delta\mathbf{u}_{eH}^{\mathrm{E/I}}\ \mathrm{d}\Omega = \varepsilon^2 \quad \forall {}^*\delta\mathbf{u}_{eH} \in^{\perp} \mathscr{V}_{eH}. \end{aligned} \tag{C.2}$$

Solutions to Eqs. (C.1) and (C.2) are obtained as

$${}^*_{\mathrm{opt}}\delta\mathbf{u}_{eH}^{\mathrm{E/I}} = \frac{([[\mathbf{t}]]^{\tilde{e}/,\tilde{e}_1} - {}^*[[\mathbf{t}]]^{\tilde{e}/,\tilde{e}_1})\varepsilon}{(\|[[\mathbf{t}]]_e^{\mathrm{E/I}} - {}^*[[\mathbf{t}]]_e^{\mathrm{E/I}}\|)}, \quad \lambda_1 = 1 \quad \text{and} \quad \lambda_2 = \frac{\|([[\mathbf{t}]]^{\tilde{e}/,\tilde{e}_1} - {}^*[[\mathbf{t}]]^{\tilde{e}/,\tilde{e}_1})\|}{\varepsilon}.$$

Appendix D. Kinematic component of the total error

On account of bilinearity of ${}_e\mathsf{a}^{\mathrm{M/I}}$, Eqs. (66) and (67) can be resolved as:

$$\begin{aligned} &{}_e\mathsf{a}^{\mathrm{M}}(\triangle\boldsymbol{\sigma}_{eH}^{\mathrm{M}}, \delta\boldsymbol{\sigma}_{eH}^{\mathrm{M}}) + {}_e\mathsf{a}^{\mathrm{M}}(\triangle\boldsymbol{\sigma}_{eH}^{\mathrm{M}}, {}^*\delta\boldsymbol{\sigma}_{eH}^{\mathrm{M}}) + {}_e\mathsf{a}^{\mathrm{M}}(\mathrm{d}\boldsymbol{\sigma}_e^{\mathrm{M}}, \delta\boldsymbol{\sigma}_e^{\mathrm{M}}) \\ &\quad = {}_e\mathsf{b}_{\mathrm{E}}^{\mathrm{M}}(\delta\boldsymbol{\sigma}_{eH}^{\mathrm{M}}, \triangle\mathbf{u}_{eH}^{\mathrm{E}}) + {}_e\mathsf{b}_{\mathrm{E}}^{\mathrm{M}}({}^*\delta\boldsymbol{\sigma}_{eH}^{\mathrm{M}}, \triangle\mathbf{u}_{eH}^{\mathrm{E}}) + {}_e\mathsf{b}_{\mathrm{E}}^{\mathrm{M}}(\delta\boldsymbol{\sigma}_e^{\mathrm{M}}, \mathrm{d}\mathbf{u}_{eH}^{\mathrm{E}}) - {}_e\mathsf{b}_{\mathrm{I}}^{\mathrm{M}}(\delta\boldsymbol{\sigma}_{eH}^{\mathrm{M}}, \triangle\mathbf{u}_{eH}^{\mathrm{I}}) - {}_e\mathsf{b}_{\mathrm{I}}^{\mathrm{M}}({}^*\delta\boldsymbol{\sigma}_{eH}^{\mathrm{M}}, \triangle\mathbf{u}_{eH}^{\mathrm{I}}) \\ &\qquad - {}_e\mathsf{b}_{\mathrm{I}}^{\mathrm{M}}(\delta\boldsymbol{\sigma}_e^{\mathrm{M}}, \mathrm{d}\mathbf{u}_{eH}^{\mathrm{I}}) \end{aligned}$$

and

$${}_e\mathsf{a}^{\mathrm{I}}(\triangle\boldsymbol{\sigma}_{eH}^{\mathrm{I}}, \delta\boldsymbol{\sigma}_e^{\mathrm{I}}) + {}_e\mathsf{a}^{\mathrm{I}}(\mathrm{d}\boldsymbol{\sigma}_e^{\mathrm{I}}, \delta\boldsymbol{\sigma}_e^{\mathrm{I}}) = {}_e\mathsf{b}_{\mathrm{I}}^{\mathrm{I}}(\delta\boldsymbol{\sigma}_{eH}^{\mathrm{I}}, \triangle\mathbf{u}_{eH}^{\mathrm{I}}) + {}_e\mathsf{b}_{\mathrm{I}}^{\mathrm{I}}({}^*\delta\boldsymbol{\sigma}_{eH}^{\mathrm{I}}, \triangle\mathbf{u}_{eH}^{\mathrm{I}}) + {}_e\mathsf{b}_{\mathrm{I}}^{\mathrm{I}}(\delta\boldsymbol{\sigma}_e^{\mathrm{I}}, \mathrm{d}\mathbf{u}_{eH}^{\mathrm{I}}). \tag{D.1}$$

Since the stress and displacement solutions in the approximation space satisfy the weak form of the kinematic relation in Eq. (7) exactly, the above equations may be simplified using Eq. (7) and the orthogonality condition (44), as

$$\begin{aligned} &{}_e\mathsf{a}^{\mathrm{M}}(\mathrm{d}\boldsymbol{\sigma}_e^{\mathrm{M}}, \delta\boldsymbol{\sigma}_e^{\mathrm{M}}) = {}_e\mathsf{b}_{\mathrm{E}}^{\mathrm{M}}({}^*\delta\boldsymbol{\sigma}_{eH}^{\mathrm{M}}, \triangle\mathbf{u}_{eH}^{\mathrm{E}}) + {}_e\mathsf{b}_{\mathrm{E}}^{\mathrm{M}}(\delta\boldsymbol{\sigma}_e^{\mathrm{M}}, \mathrm{d}\mathbf{u}_{eH}^{\mathrm{E}}) - {}_e\mathsf{b}_{\mathrm{I}}^{\mathrm{M}}({}^*\delta\boldsymbol{\sigma}_{eH}^{\mathrm{M}}, \triangle\mathbf{u}_{eH}^{\mathrm{I}}) - {}_e\mathsf{b}_{\mathrm{I}}^{\mathrm{M}}(\delta\boldsymbol{\sigma}_e^{\mathrm{M}}, \mathrm{d}\mathbf{u}_{eH}^{\mathrm{I}}) \\ &{}_e\mathsf{a}^{\mathrm{I}}(\mathrm{d}\boldsymbol{\sigma}_e^{\mathrm{I}}, \delta\boldsymbol{\sigma}_e^{\mathrm{I}}) = {}_e\mathsf{b}_{\mathrm{I}}^{\mathrm{I}}({}^*\delta\boldsymbol{\sigma}_{eH}^{\mathrm{I}}, \triangle\mathbf{u}_{eH}^{\mathrm{I}}) + {}_e\mathsf{b}_{\mathrm{I}}^{\mathrm{I}}(\delta\boldsymbol{\sigma}_e^{\mathrm{I}}, \mathrm{d}\mathbf{u}_{eH}^{\mathrm{I}}). \end{aligned} \tag{D.2}$$

Eqs. (D.2) imply that an enrichment in stress field will generate corrections to the displacement field $\mathbf{u}_{eH}^{\mathrm{E/I}} + \triangle\mathbf{u}_{eH}^{\mathrm{E/I}}$. These corrections $\mathrm{d}\mathbf{u}_{eH}^{\mathrm{E/I}}$ are a consequence of the modified traction discontinuities on the element boundaries and interfaces due to locally augmented stress fields. These stresses are obtained by solving the global traction reciprocity conditions Eq. (10) for the entire model

$$\begin{aligned} &\sum_{e=1}^{N} {}_e\mathsf{b}_{\mathrm{E}}^{\mathrm{M}}((\boldsymbol{\sigma}_{eH}^{\mathrm{M}} + \triangle\boldsymbol{\sigma}_{eH}^{\mathrm{M}} + \mathrm{d}\boldsymbol{\sigma}_e^{\mathrm{M}}), \delta\mathbf{u}_{eH}^{\mathrm{E}}) = \sum_{e=1}^{N} {}_e\mathsf{f}^{\mathrm{E}}(\delta\mathbf{u}_{eH}^{\mathrm{E}}) \quad \forall\delta\mathbf{u}_{eH}^{\mathrm{E}} \in \mathscr{V}_{eH}^{\mathrm{E}} \\ &{}_e\mathsf{b}_{\mathrm{I}}^{\mathrm{I}}((\boldsymbol{\sigma}_{eH}^{\mathrm{I}} + \triangle\boldsymbol{\sigma}_{eH}^{\mathrm{I}} + \mathrm{d}\boldsymbol{\sigma}_e^{\mathrm{I}}), \delta\mathbf{u}_{eH}^{\mathrm{I}}) - {}_e\mathsf{b}_{\mathrm{I}}^{\mathrm{M}}((\boldsymbol{\sigma}_{eH}^{\mathrm{M}} + \triangle\boldsymbol{\sigma}_{eH}^{\mathrm{M}} + \mathrm{d}\boldsymbol{\sigma}_e^{\mathrm{M}}), \delta\mathbf{u}_{eH}^{\mathrm{I}}) = 0 \quad \forall\delta\mathbf{u}_{eH}^{\mathrm{I}} \in \mathscr{V}_{eH}^{\mathrm{I}}, \ \forall e. \end{aligned}$$

The correction to the displacement field obtained from the global solution will also result in the subsequent correction to the stress field $\mathrm{d}\boldsymbol{\sigma}_e^{\mathrm{M/I}}$ for the element level Eq. (D.2).

References

[1] S. Moorthy, S. Ghosh, A model for analysis of arbitrary composite and porous microstructures with Voronoi cell finite elements, Int. J. Numer. Meth. Engrg. 39 (1996) 2363–2398.

[2] S. Ghosh, S. Moorthy, Elastic–plastic analysis of arbitrary heterogeneous materials with the Voronoi cell finite element method, Comp. Meth. Appl. Mech. Engrg. 121 (1995) 373–409.

[3] S. Ghosh, Y. Liu, Voronoi cell finite element method for micropolar thermo-elastic heterogeneous materials, Int. J. Numer. Meth. Engrg. 38 (8) (1995) 1361–1398.

[4] S. Moorthy, The Voronoi cell finite element method for response and damage analysis of arbitrary heterogeneous media, Ph.D. Dissertation, The Ohio-State University, Columbus, 1997.

[5] S. Ghosh, S. Moorthy, Particle fracture simulation in nonuniform microstructures of metal–matrix composites, Acta Mater. 46 (3) (1998) 965–982.

[6] S. Moorthy, S. Ghosh, A Voronoi cell finite element model for particle cracking in composite materials, Comp. Meth. Appl. Mech. Engrg. 151 (1998) 377–400.

[7] S. Ghosh, S.N. Mukhopadhyay, A two-dimensional automatic mesh generator for finite element analysis of random composites, Comput. Struct. 41 (1991) 245–256.

[8] M. Finot, Y.-L. Shen, A. Needleman, S. Suresh, Micromechanical modeling of reinforcement fracture in particle reinforced–matrix composites, Metall. Trans. A 25 (1994) 2403–2420.

[9] J.R. Brockenbrough, S. Suresh, W.A. Weinecke, Deformation of metal–matrix composites with continuous fibers geometrical effects of fiber distribution and shape, Acta Metall. Mater. 39 (1991) 735–752.

[10] T. Christman, A. Needleman, S. Suresh, An experimental and numerical study of deformation in metal–ceramic composites, Acta Metall. Mater. 37 (1989) 3029–3050.

[11] S. Ghosh, Z. Nowak, K. Lee, Quantitative characterization and modeling of composite microstructures by Voronoi cells, Acta Mater. 45 (6) (1997) 2215–2234.

[12] S. Ghosh, Z. Nowak, K. Lee, Tessellation based computational methods in characterization and analysis of heterogeneous microstructures, Comp. Sci. Tech. 57 (1997) 1187–1210.

[13] S. Ghosh, K. Lee, S. Moorthy, Multiple scale analysis of heterogeneous elastic structures using homogenization theory and Voronoi cell finite element method, Int. J. Solids Struct. 32 (1) (1995) 27–62.

[14] S. Ghosh, K. Lee, S. Moorthy, Two scale analysis of heterogeneous elastic–plastic materials with asymptotic homogenization and Voronoi cell finite element model, Comp. Meth. Appl. Mech. Engrg. 132 (1996) 63–116.

[15] K. Lee, S. Moorthy, S. Ghosh, Multiple scale computational model for damage in composite materials, Comp. Meth. Appl. Mech. Engrg., 172 (1999) 175–201.

[16] J.T. Oden, L. Demkowicz, T. Strouboulis, P. Devloo, in: I. Babuska, O.C. Zienkiewicz, J. Gago, E.R. Oliveria (Eds.), Adaptive Methods for Problems in Solid and Fluid Mechanics, Accuracy Estimates and Adaptive Refinements in Finite Element Computations, Wiley, New York, 1986, pp. 249–280.

[17] M. Ainsworth, A. Craig, A posteriori error estimators in the finite element method, Numer. Math. 60 (1992) 429–463.

[18] M. Ainsworth, J.T. Oden, A procedure for a posteriori error estimation for *h–p* finite element methods, Comp. Meth. Appl. Mech. Engrg. 101 (1992) 73–96.

[19] J.T. Oden, W. Wu, M. Ainsworth, An a posteriori error estimate for finite element approximations of the Navier Stokes equations, Comp. Meth. Appl. Mech. Engrg. 111 (1994) 185–202.

[20] I. Babuska, W.C. Rheinbolt, Error estimates for adaptive finite element computations, SIAM J. Numer. Anal. 15 (4) (1978) 736–754.

[21] I. Babuska, L. Plank, R. Rodriguez, Quality assessment of the a posteriori error estimation in finite elements, Finite Elements in Anal. Design 11 (1991) 285–305.

[22] O.C. Zienkiewicz, J.Z. Zhu, The superconvergent patch recovery and aposteriori error estimates, Part I. The recovery techniques. Part 2. Error estimates and adaptivity, Int. J. Numer. Meth. Engrg. 33 (1992) 1365–1382.

[23] I. Babuska, T. Strouboulis, A. Mathur, C.S. Upadhyay, Pollution error in the h-version of the finite element method and the local quality of a posteriori error estimators, Finite Elements in Anal. Design 17 (1994) 273–321.

[24] I. Babuska, T. Strouboulis, C.S. Upadhyay, S.K. Gangaraj, A posteriori estimation and adaptive control of the pollution error in the *h*-version of the finite method, CMC Report No. 94-06, August 1994.

[25] J.T. Oden, Y. Feng, Local and pollution error estimation for finite element approximations of elliptic boundary value problems, TICAM Report 95-03, The University of Texas, 1995.

[26] W-M. Xue, S.N. Atluri, Existence and stability and discrete BB and rank conditions for general mixed-hybrid finite elements in elasticity, in: R.L. Spilker, K.W. Reed (Eds.), Hybrid and Mixed Finite Element Methods ASME-AMD (13), 1985, pp. 91–112.

[27] W-M. Xue, L.A. Karlovitz, S.N. Atluri, On the existence and stability conditions for mixed-hybrid finite element solutions based on Reissner's variational principle, Int. J. Solids Struct. 21 (1) (1985) 97–116.

[28] L-A. Ying, S.N. Atluri, A hybrid finite element method for Stokes flow: Part II: stability and convergence studies, Comp. Meth. Appl. Mech. Engrg. 36 (1983) 39–60.

[29] I. Babuska, The finite element method with Lagrange multipliers, Numer. Math. 20 (1973) 179–192.

[30] I. Babuska, J.T. Oden, J.K. Lee, Mixed-hybrid finite element approximations of second order elliptic boundary value problems, Part I, Comp. Meth. Appl. Mech. Engrg. 11 (1977) 175–206.

[31] F. Brezzi, On the existence uniqueness and approximation of saddle-point problems arising from Lagrange Multipliers, R.A.I.R.O 8-R2, 1974, pp. 129–151.

[32] J.N. Reddy, J.T. Oden, Mathematical theory of mixed finite element approximations, Quart. Appl. Math. 33 (1975) 255–280.
[33] J.K. Lee, Convergence of mixed-hybrid finite element models, Ph.D. Dissertation, University of Texas, Austin, 1976.
[34] N.I. Muskhelishvili, Some Basic Problems in the Mathematical Theory of Elasticity, P. Nordhoff, Netherlands, 1965.
[35] G. Savin, Stress Concentrations Around Holes, Pergamon Press, Oxford, 1951.
[36] S.P. Timoshenko, J.N. Goodier, Theory of Elasticity, McGraw-Hill, New York, 1970.
[37] N.J. Pagano, E.F. Rybicki, On the significance of effective modulus solutions for fibrous composites, J. Comp. Mater. 8 (1974) 214–228.
[38] M. Kofler, Maple Version 5 Release 3: An Introduction and Reference, Addison-Wesley, Reading, MA, 1997.
[39] ANSYS User's Manual, Version 5.3, Swanson Analysis Systems Inc.